1-1-2017

Thermomechanical Stability of Automotive Clutches and Brakes

Zhuo Chen
University of Denver

Thermomechanical Stability of Automotive Clutches and Brakes

Abstract

Finite element analyses were performed to evaluate the stability thermal buckling existing in clutch disks. The commercial software ABAQUS had been used. It was discovered that monotonically increasing thermal loads constantly result in axisymmetric buckling modes. When the maximum values of thermal loads were located at the medium radii of the models, the non-axisymmetric modes became dominant. The buckling mode and buckling temperature of the model in which the profile of thermal load varies periodically in the circumferential direction were also tentatively studied. The [achievements] described in this part of this dissertation had been published in Ref. [33].

The numerical analysis was applied to inspect the thermal buckling of an annular plate using a reduced Fourier method. The stress stiffness matrix was derived from the geometric nonlinearity in the Green strains with a predefined circumferential wave number. It was implemented to solve non-axisymmetric problems with multiple reversals in the circumferential direction. It was shown that there exists a particular wave number with which the buckling temperature reaches a minimum. The [achievements] described in this part of this dissertation had been published in Ref. [58].

Through performing finite element analyses, the coupling between thermal buckling and thermoelastic instability (TEI) was studied. The eigenmodes (i.e. nodal temperature distributions) obtained from TEI analyses were applied as the reference thermal loads. The effects of the sliding speed, the coefficient of friction, and the boundary condition had been investigated. It was concluded that TEI and thermal buckling could interact with each other in some situations. The [achievements] described in this part of this dissertation will be published in Ref. [63].

Linear and nonlinear buckling finite element analyses were performed to evaluate the thermal postbuckling of clutch metal disks. The dominant buckling modes were firstly obtained through linear buckling FEA analyses. The scaled displacement fields obtained from the linear buckling analyses were applied to the original geometries to produce the perturbed meshes. The postbuckling behaviors were then investigated through nonlinear buckling FEA analyses. The software ABAQUS was used as the fundamental numerical tool. It was discovered the temperature dependence of material properties significantly decreases the cirtical buckling. The [achievements] described in this part of this dissertation will be published in Ref. [72].

Document Type

Dissertation

Degree Name

Ph.D.

Department

Engineering

First Advisor

Yun-Bo Yi, Ph.D.

Second Advisor

Maria Calbi, Ph.D.

THERMOMECHANICAL STABILITY OF AUTOMOTIVE CLUTCHES AND BRAKES

_____

A Dissertation

Presented to

the Faculty of the Daniel Felix Ritchie School of Engineering and Computer Science

University of Denver

_____

In Partial Fulfillment

of the Requirements for the Degree

Doctor of Philosophy

_____

by

Zhuo Chen

August 2017

Advisor: Dr. Yun-Bo Yi

Author: Zhuo Chen
Title: THERMOMECHANICAL STABILITY OF AUTOMOTIVE CLUTCHES AND BRAKES
Advisor: Dr. Yun-Bo Yi
Degree Date: August 2017

Abstract

Finite element analyses were performed to evaluate the stability thermal buckling existing in clutch disks. The commercial software ABAQUS had been used. It was discovered that monotonically increasing thermal loads constantly result in axisymmetric buckling modes. When the maximum values of thermal loads were located at the medium radii of the models, the non-axisymmetric modes became dominant. The buckling mode and buckling temperature of the model in which the profile of thermal load varies periodically in the circumferential direction were also tentatively studied. The achievments described in this part of this dissertation had been published in Ref. [33].

The numerical analysis was applied to inspect the thermal buckling of an annular plate using a reduced Fourier method. The stress stiffness matrix was derived from the geometric nonlinearity in the Green strains with a predefined circumferential wave number. It was implemented to solve non-axisymmetric problems with multiple reversals in the circumferential direction. It was shown that there exists a particular wave number with which the buckling temperature reaches a minimum. The achievments described in this part of this dissertation had been published in Ref. [58].

Through performing finite element analyses, the coupling between thermal buckling and thermoelastic instability (TEI) was studied. The eigenmodes (i.e. nodal temperature distributions) obtained from TEI analyses were applied as the reference thermal loads. The effects of the sliding speed, the coefficient of friction, and the

boundary condition had been investigated. It was concluded that TEI and thermal buckling could interact with each other in some situations. The achievments described in this part of this dissertation will be published in Ref. [63].

Linear and nonlinear buckling finite element analyses were performed to evaluate the thermal postbuckling of clutch metal disks. The dominant buckling modes were firstly obtained through linear buckling FEA analyses. The scaled displacement fields obtained from the linear buckling analyses were applied to the original geometries to produce the perturbed meshes. The postbuckling behaviors were then investigated through nonlinear buckling FEA analyses. The software ABAQUS was used as the fundamental numerical tool. It was discovered the temperature dependence of material properties significantly decreases the cirtical buckling. The achievments described in this part of this dissertation will be published in Ref. [72].

Acknowledgements

It has been more than seven years since I arrived in Denver on March 15th, 2010. During these seven years, there is memorable struggle and happiness. The experience living and studying in Denver will be a special treasure to me.

I am willing to say thanks to my academic advisor, Dr. Yun-Bo Yi, first. His teaching and advice are always valuable for me, especially, when I encounter difficulties. Without his help and guidance, it would be impossible for me to complete my master and Ph.D. programs.

Most importantly, I am willing to give thanks to my parents. Their love and support are my ultimate energy source to chase my goals. It is their encouragements stimulating me to overcome hardness and step forward.

I am also happy to thank my committee members, Dr. Calbi, Dr. Azadani and Dr. Matin who gave me treasured suggestions. Thanks also to the DU faculty and staff in the Department of Mechanical and Materials Engineering.

I would like to thank my friends and classmetes whom I met at Denver: Jian Qiu, Qi Pan, Dongfang Zhao, Wanqing Yang, Shu Zhong, Yuchen Du, Jiaxin Zhao, Ke Bao, Demao Xia, Heyan Li, Xueyuan Li, Tim Sheu, Ali Bendawi, John Leicham, Justin Huff, Brett Barlow, Danny Sorenson, Tyler Traasdahl, Travis Hamilton and so on. I appreciate friendships and companions from you.

Finally, I want to thank all my relatives who are alive and who have passed away and all the people who love and support me.

Zhuo Chen

June 27th, 2017

Table of Contents

List of Figures

List of Tables

1. INTRODUCTION

1.1 A Brief Review of Automotive Clutch Systems

Clutches are widely used to transfer power and rotations from driving parts to driven parts of machines. For instance, there is a clutch installed between the engine and the transmission of an automotive vehicle. In a vehicle, the function of a clutch is to transmit rotation, power and torque from the energy source (i.e. engine) to the driveline. Also, the transfers of rotation, power and torque can be interrupted as needed.

Figure 1.1: A multi-disc clutch system

By the working principle, clutches are classified into electromagnetic clutch, belt clutch, hydraulic clutch, magnetic particle clutch, frictional clutch and so on [1,2]. Frictional clutch in which the driven parts are connected to the driving parts through friction is the most frequently used type of clutch. By the cooling method, frictional clutches can be categorized into dry clutches and wet clutches in which cooling liquids

are applied to decrease the working temperatures of systems. By the working mechanism, frictional clutches are grouped as single-disc clutches and multi-disc clutches in which multiple sets of friction disks and metal disks are coupled with each other. A typical multi-disc clutch assembly is shown in Figure 1.1 [3].

As the areas of contacting surfaces between driving disks and driven disks increase, more power and torques can be transferred through multi-disc clutches, and the sizes of clutch assemblies are reduced. However, failures introduced by high temperature restrict the applications of multi-disc clutch [4,5].

1.2 A Brief Review of Automotive Brakes

The working principle of automotive brakes is essentially the same as that of automotive clutches. Clutches and brakes connect mechanical parts through friction, magnetism, hydraulic power and so on. Some mechanical devices can be used as either brakes or clutches. When a rotating part is coupled with another rotating part, the device is considered as a clutch. If one stationary part is connected to a rotating part, a device is considered as a brake [1]. The figure below represents classic disk brake assembly [6].

Figure 1.2: An automotive disk brake

In an automotive vehicle, a brake is applied to stop or slow the vehicle. By working principle, brakes can be classified into electromagnetic brake, frictional brake, pumping brake and so on. In the braking process of a frictional brake, kinetic energy is transferred to heat [7]. Therefore, the working temperature of an automotive brake rises rapidly, especially, during an emergent stop.

Based on the configurations of the rotating parts, frictional brakes can be categorized as *drum brakes* and *disk brakes*. In a drum brake, the rotating part that is installed at the wheel hub is with a drum shape, a set of brake shoes are pressed against the contacting surface of the rotating parts (i.e. the drum). The configuration of the brake rotor of a disk brake is an annular plate. The rotating disk is fixed to the wheel hub or the axle of a vehicle. The most common material for brake disks is cast iron. The rotors of high-performance disk brakes are made of ceramics. Compared with disk brakes, the costs of drum brakes are relatively lower, but drum brakes are more likely to be worn out. Normally, drum brakes are installed on vehicles made decades ago and less expensive vehicles. Theoretically, the kinetic energy of a vehicle is transferred to heat during a braking process. However, a significant amount of kinetic energy is actually converted into acoustic energy which leads to the noise problem.

1.3 A Brief Review of Thermoelastic Instability

Figure 1.3: Hot spots around circumference

The first type of failure mechanism induced by severe heat generation is called as thermoelastic instability or "TEI" for short. It is believed that the contact pressures between friction disks and metal disks are uniform. However, disturbances may exist in environments or devices. Usually, the disturbances are introduced by the disturbed temperature fields, the manufacturing imperfections and the installation misalliances. The disturbances produce uneven contact pressures and hence the non-uniform heat generations when driving parts are sliding against driven parts. The non-uniform heat generations, in turn, make contact pressures more non-uniform. If the sliding speed is above a critical value, which is defined as critical speed, the coupled thermal-mechanical behavior of a sliding system will become unstable. When this phenomenon exists in a multi-disc clutch system, the contacting area between friction disks and metal disks switches to multiple separated regions that are called as "hot spots". The temperatures of hot spots increase rapidly [8].

The TEI phenomenon was first discovered in a train braking test [9]. It was found that the heat generation during a braking process can be localized. Barber then performed

the pioneering research on this phenomenon experimentally and theoretically [10,11]. It was found that the thermal deformation transforms the contacting area from a uniform surface to separated, localized regions (hot spots).

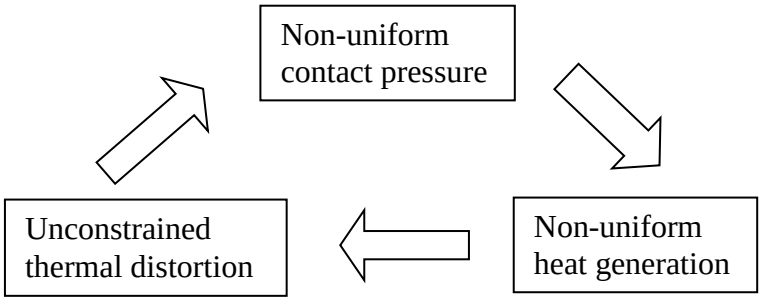

Figure 1.4: Mechanism of TEI

Burton applied the perturbation method to a half-plane model to investigate this problem [12]. It was assumed that there is a disturbed contact pressure existing in the contacting interface. In this study, the concept of *critical speed* had been proposed. The scholar claimed that the TEI phenomenon only exists after the sliding speed of the system reaches the critical value. Nonetheless, the critical speeds calculated via Burton's theory are higher than the experimentally obtained values. Another disadvantage of this half plane theory is that characteristic dimension has not been introduced to the model. To research a realistic clutch or an automotive brake, we have to focus on perturbations whose wavelengths are not longer than the perimeters of disks.

It was found that TEI can result in the thermal-mechanical fatigue in train brake plates by Fec and Sehitoglu [13]. Anderson and Knapp revealed that the localized zones on the surfaces of brake disks with elevated temperature lead to problems such as cracks, material degradation, and braking failure [14]. The researchers classified hot spots into four types: *asperity*, *focal*, *distortional* and *regional*. All kinds of hot spots are root causes of braking failure and noise.

Based on Burton's previous work, Lee et al. developed a model in which there are two half planes pressing against a moving layer with a limited thickness [15]. They concluded that the antisymmetric modes are dominant, in other words, the hot spots on a surface of a disk are in the middle of the intervals of hot spots on the other surface of the disk. It was also found that the wavelength of the dominant mode is proportional to the thickness of the layer. They concluded that the finite thickness of the sliding layer is the cause of the difference between the predicted critical speeds via Burton's method and the critical speeds obtained through performing experiments. Lee's model is broadly applied to evaluate the susceptibility of clutches and brakes toward TEI.

Vernersson investigated TEI through performing experiments in which both cast iron brake pads and composite brake pads were selected [16,17]. It was discovered that disturbances in brakes could cause hot spots in braking processes, and the temperature of hot spots are higher than the temperature of the vicinity. Due to thermal expansion, the material around hot spots expands more than the material of vicinity; therefore the wear around hot spots is more apparent. This coupled thermal-mechanical mechanism is the primary reason of the non-uniform roughness in brake disks and clutch plates.

To investigate the effects of geometric differences between the realistic three-dimensional clutch disks and Lee's simplified two-dimensional model, Du incorporated Burton's perturbation method into a finite element analysis algorithm [18,19]. It was assumed that the brake pad is ideally rigid and thermally insulated. Based on this assumption, the growth rates of perturbations are real. In other words, perturbations do not move over the contacting interface.

Yi applied Du's method to investigate the impacts of geometric differences between a real clutch plate and the two-dimensional model on TEI phenomenon [20]. It was found that based on plain strain assumption the calculated critical speeds are quite accurate when the number of hot spots is large.

The basis of Du's method is that the brake pad is made of a type of material that is completely not deformable and thermally non-conducting. Based on this assumption, the perturbation does not migrate over the brake pad. However, there is no a type of material which is perfectly rigid and thermally insulated. Due to the conductivity of the pad material is considerably lower than that of the brake disk material; the migration speed of a perturbation over the brake disk is very slow. However, the migrations of perturbations affect the stability behaviors significantly, as the migrations of perturbations reduce the thermal expansions and hence raise the critical speeds of the dominant TEI modes.

Yi incorporated Burton's theory into an FEA algorithm to evaluate the TEI of clutches and brakes in which both friction components and metal components are made of thermal conductors [21,22]. In this analysis, eigenvalue method was applied to determining the exponential growth rates of the eigenmodes. Yi's algorithm had been integrated into the CAE software *hotspotter* [23]. When the number of hot spots (i.e. TEI wave number) is defined, the critical speed of the corresponding eigenmode can be determined. When the sliding speed is provided, the growth rates of multiple eigenmodes can be calculated.

Jang and Ahn developed a transient two-dimensional finite element model to evaluate TEI caused by frictional heat generation. In their model, there is a fixed functionally graded material (FGM) plate between two sliding layers. Jang and Ahn

discovered that the functionally graded material coating on the surface of the metal plate increases the critical speed of a system [24]. The effects of the constituent parameter of the FGM upon TEI phenomenon was also evaluated. It was found that an optimum value of the constituent parameter which yields the highest critical speed exists when the thickness of FGM coating is given. They concluded that the application of FGM coating could prevent the TEI of clutches.

Zhao et al. studied the influences of friction material properties on TEI of multi-disc clutches and automotive brakes. The dominant TEI modes and the associated critical speeds of models with different types of friction materials were investigated through analytical methods and finite element analyses. Zhao et al. concluded that the frictional material properties affect the dominant modes considerably [25]. It was also revealed that the symmetric TEI modes could be dominant modes if Young's moduli of friction materials are adequately large or the conductivities of friction materials are sufficiently small.

1.4 A Brief Review of Thermal Buckling and Postbuckling of Clutch Disks and Brake Disks

Another cause of failures of multi-disc clutch systems and disk brakes is thermal buckling of metal disks. During engagements of an automotive multi-disc clutch system and braking processes of a disk brake, a large quantity of thermal energy can be generated in the interfaces between metal disks and friction disks (or pads). The elevated temperature can cause circumferential stress and out-of-plane bending moment. When the bending moment exceeds a critical value, the annular plate buckles laterally [26]. The behavior of a structure after it buckles is considered as postbuckling [27,28 and 29].

In the presence of thermal buckling, the configurations of clutch disks can be distorted. Therefore, the contact pressure and frictional heat generation become nonuniform. Consequently, failures such as surface degradations, plastic deformations of disks and difficulties to be disengaged will be induced [30]. Due to its importance in industrial applications, extensive thermal buckling analyses of clutch disks have been reported in the literature, some of them are reviewed here.

Timoshenko developed a beam theory assuming that a curved beam buckles laterally when the in-plane bending moment exceeds the critical value [31]. However, the stress variation in the radial direction is simplified in this theory.

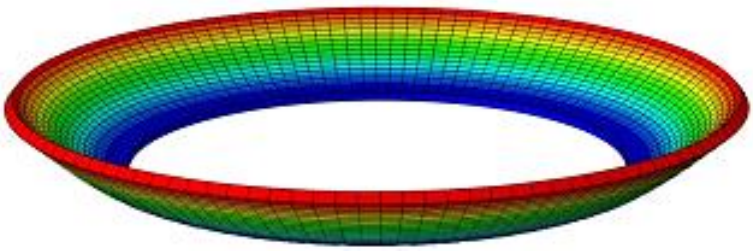

Axisymmetric mode

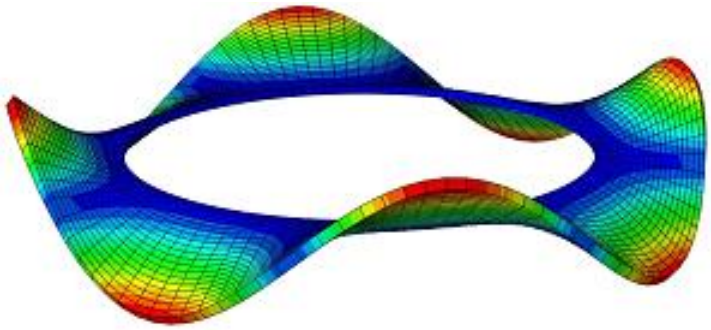

Non-axisymmetric mode

Figure 1.5: Thermal buckling modes of clutch metal disks

Audebert et al. investigated thermal buckling of multi-disc clutch plate analytically and numerically [32]. They calculated the critical bending moments of

axisymmetric and non-axisymmetric buckling modes. It was also found that for normal designs of multi-disc clutches the critical temperature inducing thermal buckling is around 600 ℃. They also revealed that the dominant buckling mode of a clutch plate could be either axisymmetric or non-axisymmetric.

To study the thermal buckling of brake disks, Ma [26] derived the governing equations of thermal buckling of annular disks based on Timoshenko's beam theory and Rayleigh-Ritz plate theory. The analytically computed results were applied to validate the finite element models evaluating the thermal buckling of annular disks. It was concluded that FEA models could solve thermal buckling problems of annular disks efficiently and accurately. It was also found that the thermal buckling behaviors are influenced by the boundary conditions considerably. The effects of geometric dimensions and structural features on thermal buckling behaviors had also been studied.

Xiong et al. [30] designed a new type of sliding experiment of a multi-disc wet clutch assembly to record the temperature distribution and the bending moment in the friction disk. To record the signs of thermal buckling, friction disks with single lining were selected and arranged in back-to-back formation. They validated that the recorded temperature through performing one-dimensional finite element analysis. It was also revealed that the calculated critical bending moment obtained by using the beam theory matches the experimentally recorded critical bending moment leading to thermal buckling. Finally, they concluded that both the coning and the wavy buckled configurations may exist.

Zhao et al. evaluated the effects of diverse kinds of thermal loading profiles on the thermal buckling behavior of clutch disks [33]. It was found that temperature

distributions are increasing from inner radii to outer radii of disks monotonically always lead to axisymmetric thermal buckling. Meanwhile, when the highest temperatures of thermal loads occur at the medium radii of annular disks, the non-axisymmetric buckling modes are with lowest buckling temperatures. The buckling modes and critical buckling temperatures of the models in which the temperature distributions vary periodically in circumferential direction were also tentatively tested.

The conventional buckling FEA analysis or *linear* buckling FEA analysis is only able to determine whether a structure is stable or not under a particular load. The postbuckling or *nonlinear* FEA buckling analysis is also able to evaluate the displacement field at a particular loading condition. Limited works have been devoted to the thermal postbuckling of clutch plates and brake disks. However, there are multiple relevant achievements.

By using the von Karman plate theory, Ma studied axisymmetric postbuckling of FGM circular plate under thermal, mechanical and combined thermal-mechanical loads [34]. The properties of functionally graded material vary through the thickness of the disk based on the power law of volume fraction of the components of FGM. The impacts of material parameters and different boundary conditions on the critical buckling temperatures and postbuckling of the disk had also been investigated.

By applying the von Karman plate theory, Li studied axisymmetric thermal postbuckling of FGM circular plate in which there is a geometric imperfection [35]. In their research, the imperfection of geometry was considered as an initial bending moment. The effects of the imperfection were discussed.

Sepahi inspected axisymmetric postbuckling of annular plates that are fixed in the inner and outer radii based on the first order shear deformation theory [36]. They presented the critical buckling temperatures and displacement profiles along the radial direction.

1.5 A Brief Review of Numerical Tools Used in the Current Research

1.5.1 A Brief Review of Hotspotter

Hotspotter is an FEA software package evaluating the TEI of frictional systems. Hotspotter was developed by Barber and Yi. There are two modules in this software: *classic* and *full three-D*. The Fourier finite element algorithm has been incorporated into the classic module [23,37].

The "*Classic*" module yields TEI critical speeds when the hot spot numbers are specified. As the Fourier finite element algorithm is applied, only the cross section of an annular disk is needed to be discretized; this module applies to systems with axisymmetric configurations. The "*full three-D*" module can generate eigenvectors as temperature distributions when the sliding speeds are specified. In the current research, the full three-D module is being applied as the primary numerical tool. In Hotspotter, we can define the geometric parameters, material parameters as well as boundary conditions of a in the graphic user interface of the Classic module. However, a computational model in the Full 3-D module must be developed through an input script file. The GUI of Hotspotter is shown in Figure 1.6.

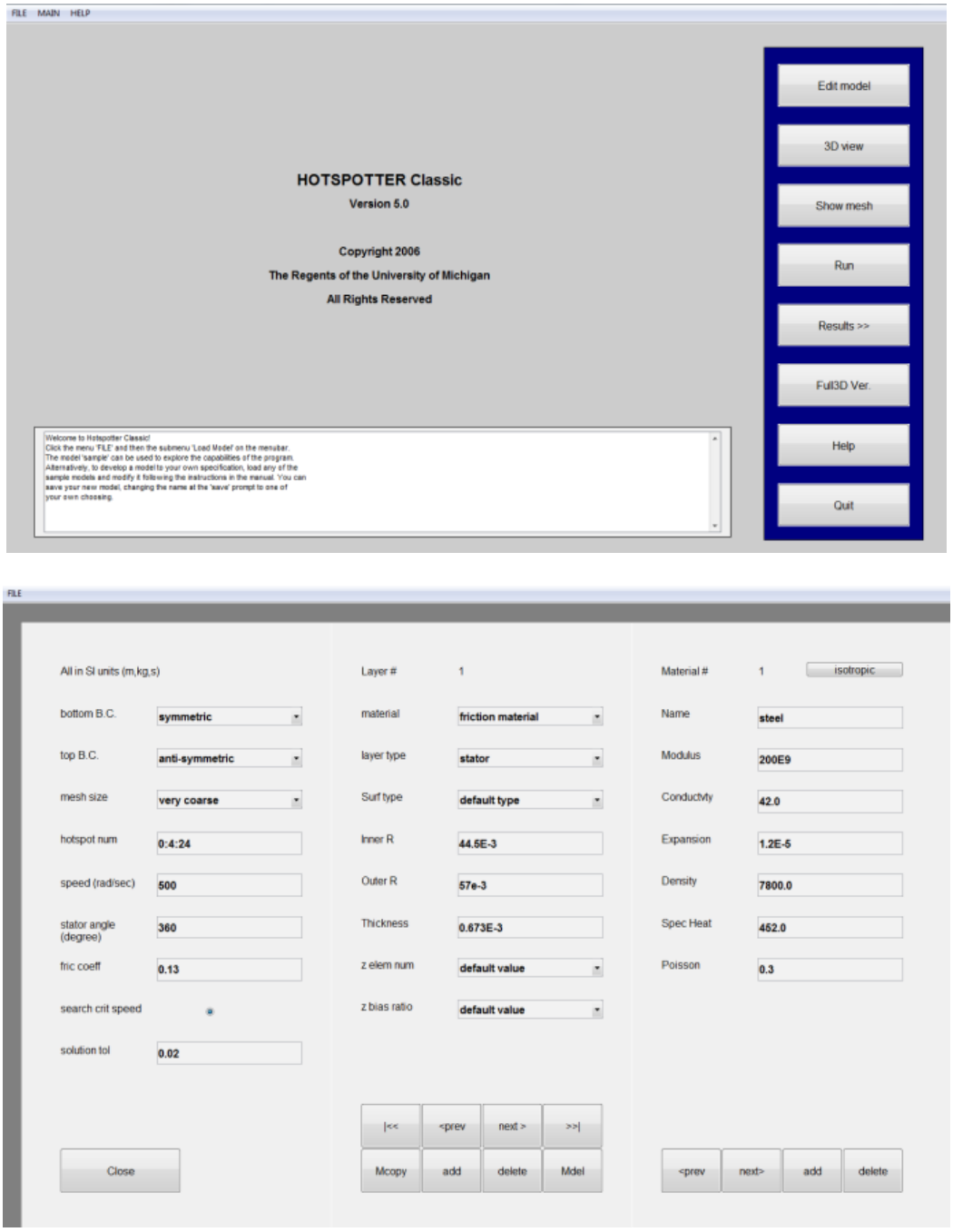

Figure 1.6: The GUI of HOTSPOTTER

1.5.2 A Brief Review of ABAQUS

ABAQUS is commercial FEA software developed by Dassault Group [38,39]. In ABAQUS, there are two modules*: Standard* and *Explicit*. The Abaqus/Standard employs

Newton's method or the Newton-Raphson method to solve equations iteratively. In Abaqus/Explicit, the explicit dynamic finite element formulation is used to simulate problems.

In the current research, the linear buckling analyses are performed by using "*buckle*" analysis step. Linear buckling analysis is a type of eigenvalue method determining the theoretically critical buckling load. As imperfections of structural geometries, nonlinearities of material properties and geometric nonlinearities have not been considered in this type of analysis; the obtained results are probably less conservative. This method is also applied as the first step of nonlinear buckling analysis [40,41].

After a structure buckles, it is still able to be loaded. The behavior of a structure after it buckles is called as postbuckling. The postbuckling needs to be evaluated by using *nonlinear* buckling finite element analysis which can be conducted through "*Riks*" analysis step. In the nonlinear buckling analysis, imperfections of structural geometries, nonlinearities of material properties and geometric nonlinearities have been taken into consideration. Thus, the results are more reliable and conservative.

1.6 A Brief Review of Finite Element Analyses of Thermal-mechanical Phenomena in Clutches and Brakes

Zagrodzki [4] developed a two-dimensional finite element model to evaluate the temperature field and stress distribution of a multi-disc clutch system. It was assumed that the temperature field does not change the contact pressure field. As a result, the frictional heat generation was not affected by the temperature field in Zagrodzki's research. It was found that the calculated thermal stress field is not severe based on the

aforementioned assumption. It was also concluded that due to different sliding speeds the friction heat generation at different radial positions is different, which results in a sharp increase in the circumferential stress. However, there is no solid evidence proving that Zagrodzki's assumption in ref. [4] is valid. During real applications, the contact pressure fields on the contacting interfaces are not even, which leads to the non-uniform frictional heat generations and thermal deformations. The uneven frictional heat generations and thermal deformations can also affect the distributions of contact pressure. This coupling process is called as the thermal-mechanical transition.

Choi and Lee investigated the coupled thermal-mechanical process existing on the contacting surface of the brake pad and brake disk of an automotive disk brake in the condition that the brake has been used repeatedly. The temperature field and stress distribution of the automotive brake disk, contact pressure distribution on the interface and the thermoelastic instability of the disk brake were evaluated. To optimize the designs of automotive disk brake systems, the influences of material properties and dimensional parameters on the coupled thermal-mechanical process were also studied. It was found that due to the high value of the circumferential thermal stress, the circumferential stress in a brake disk is the key factor restricting the safety of a disk brake system. It was also discovered that the contact ratio of the contact pair (i.e. the brake pad and brake disk) is strongly impacted by the material properties such as elastic modulus and the expansion coefficient [42,43].

All the aforementioned results were achieved through the two-dimensional finite element analyses. Analyzing the transient coupled thermal-mechanical processes of multi-disc clutches and disk brakes by applying conventional three-dimensional FEA

models is numerically inefficient. It is because severe nonlinearities such as rotational movements and friction are involved and extremely fine meshes are required to eliminate the numerical difficulty caused by the convective heat transfer. Cho and Ahn applied the Fourier finite element method through which researchers only need to discretize the cross sections of annular plates to investigate the coupled thermal-mechanical behaviors of multi-disc clutches and disk brakes [44].

1.7 Overview of This Dissertation

Based on the literature review and preliminary researches, the main body of this dissertation is divided into five chapters.

In Chapter 2, the effects of different temperature profiles on thermal buckling behaviors will be discussed. For this purpose, multiple three-dimensional finite element models in which clutch disks are represented as annular plates will be developed. The thermal loads discussed in this chapter can be classified as two groups that have uniform temperature distributions in the circumferential direction. In the first set of thermal loads, the temperature profiles increase from the inner radii to the outer radii of clutch disks. Whereas, the peak values of the second set of temperature profiles are located around the medium radii of clutch disks.

Clutch disks are normally represented by annular plates in finite element analysis models. Therefore, developing FEA models by using axisymmetric elements is beneficial as the efficiency and accuracy of FEA simulations can be considerably enhanced. However, the traditional axisymmetric elements in the commercial FEA software ABAQUS are only capable of simulating problems in which both the applied loads and calculated displacement fields are axisymmetric. Therefore, the Fourier elements are

necessary to be implemented in FEA models to evaluate thermal buckling of clutch disks and brake disks. The related works will be discussed in Chapter 3. With this methodology, only the cross section of an annular plate is needed to be discretized, and the displacement field can be expressed in the Fourier terms. This strategy has been applied to study the TEI problems of multi-disc clutches and thermoelastic damping in MEMS as well [45,46].

Among all the previous works on thermal buckling of clutch disks and brake disks, the temperature distributions were based on the experimental observations or plausible assumptions. However, the temperature fields can be strongly affected by the excited TEI modes, which might be significantly different from those presumed temperature distributions. Therefore it is important to study the coupling between TEI and thermal buckling of annular disks. Chapter 4 aims at assessing the possibility of thermal buckling in the presence of TEI, particularly how the different TEI modes change the critical buckling temperatures and the corresponding modes.

In Chapter 5, the nonlinear buckling analysis will be elaborated. The conventional linear buckling analysis is only able to caluate the critical buckling loads and the associated buckled configurations. To obtain the buckling displacement fields, nonlinear buckling analyses must be performed. In this chapter, the temperature distributions are assumed as linearly increasing from the inner radii to the outer radii of clutch disks. The effects of different boundary conditions and the temperature dependences of material properties will be discussed. Also, the effects of the plasticity of material will be tentatively evaluated.

The conclusions of the current study and future works will be presented in the last chapter.

2 EFFECTS OF DIFFERENT TEMPERATURE PROFILES ON THERMAL BUCKLING OF CLUTCH DISKS

2.1 Introduction

There is severe frictional heat generation in the contacting interfaces of automotive disk brakes and clutch systems during applications of automotive disk brakes and clutch systems. As a result, the working temperatures of automotive disk brakes and clutches can increase significantly, and the thermal stresses induced by the elevated temperature fields are the root causes of system failures. Thermoelastic instability (TEI) [47] and thermal buckling [48] are two main categories of failure mechanisms. The principle of thermal buckling of clutch plates is the raised temperature fields result in thermal stresses along circumferential direction after which reach critical values the stabilities of systems will be lost [49]. As the dimensions of multi-disc clutch plates in the thickness direction are not large, thermal buckling is the main reason for failures of such systems. The primary purpose of thermal buckling analyses is obtaining the buckling deformation modes and determining the associated critical buckling temperatures above which the stabilities of systems will be lost.

Ma [26] and Audebert [32] evaluated the influences of material properties and geometric dimensions upon the thermal buckling behaviors of brake plates and clutch disks. However, the effects of different types of thermal loading profiles have not been

thoroughly studied. In this chapter, we elaborate our effort devoted to this field. The method and its verification are also presented.

2.2 Methods

2.2.1 Finite Element Formation

A structure buckles when the stability of an equilibrium pattern is lost, while there is no material separation or breakage. The most common type of buckling is the *bifurcation buckling*. In the presence of the *bifurcation buckling*, the membrane strain energy transfers to bending strain energy while the applied load remains. In a Euler bar, this relation can be expressed by using following equations.

$$U_m = \frac{\pi^2 P}{4L} v_c^2 \tag{2-1}$$

$$U_b = \frac{\pi^4 EI}{4L^3} v_c^2 \tag{2-2}$$

$$U_m + U_b = 0 \tag{2-3}$$

Therefore, the critical buckling load is $P_{cr} = -\frac{\pi^2 EI}{L^2}$. In the above equations, L represnts the length of the bar, U_m represents the membrane strain energy, U_b represents the bending strain energy, P is the external load, P_{cr} is the critical buckling load, v_c is the buckling displacement at the midpoint of the bar, E is elastic modulus and I is second moment of area.

In the finite element analysis investigating buckling problem, the aforementioned principle is accounted by adding a stress stiffness matrix $[K_\sigma]$ to the stiffness matrix $[K]$ [50,51].

$$[k_\sigma] = \int [G]^T \begin{bmatrix} s & 0 & 0 \\ 0 & s & 0 \\ 0 & 0 & s \end{bmatrix} [G] dV \tag{2-4}$$

In the above equation, s is defined as

$$s = \begin{bmatrix} \sigma_x & \tau_{xy} & \tau_{zx} \\ \tau_{xy} & \sigma_y & \tau_{yz} \\ \tau_{zx} & \tau_{yz} & \sigma_z \end{bmatrix} \quad (2\text{-}5)$$

The matrix $[G]$ consists of the differentiations of shape functions, which is defined as

$$\lfloor G \rfloor = \frac{d}{dx} \lfloor N \rfloor \quad (2\text{-}6)$$

where $\lfloor N \rfloor$ consists of the shape functions.

The reference stress stiffness matrix $[K_\sigma]_{ref}$ can be determined, when the structure is loaded by a reference load $\{R\}_{ref}$. As the load applied to the structure changes to $\{R\} = \lambda\{R\}_{ref}$, the stress stiffness matrix will become $[K_\sigma] = \lambda[K_\sigma]_{ref}$. Either the reference configuration of the structure or a buckled configuration of the structure can exist under the critical load. As a result, the following two equations are obtained.

$$\left([K] + \lambda_{cr}[K_\sigma]_{ref}\right)\{D\}_{ref} = \lambda_{cr}\{R\}_{ref} \quad (2\text{-}7)$$

$$\left([K] + \lambda_{cr}[K_\sigma]_{ref}\right)\left\{\{D\}_{ref} + \delta D\right\} = \lambda_{cr}\{R\}_{ref} \quad (2\text{-}8)$$

In the above equations, δD contains the vector of buckling displacement, λ_{cr} represnts the critical buckling eigenvalue and $\{R\}_{cr} = \lambda_{cr}\{R\}_{ref}$ represents the critical buckling load. Through subtracting the above two equations, the equation defining the eigenvalue problem of buckling is obtained.

$$\left([K] + \lambda_{cr}[K_\sigma]_{ref}\right)\{\delta D\} = \{0\} \quad (2\text{-}9)$$

2.2.2 Selection of Finite Element

Generally used commercial software ABAQUS is capable of performing FEA analyses to evaluate various buckling problems. A clutch disk is a thin annular plate. The

geometric representation of the model can be built by using three-dimensional elements, which is the most general and natural choice. However, the dimension in the thickness direction is negligible; we can therefore develop the model by using shell elements. This choice not only accounts the variations of temperature and displacement in radial and circumferential directions but also increases the efficiency of the simulation. Furthermore, a model built by using axisymmetric elements is appropriate for axisymmetric buckling modes when the applied loads are also uniform in the circumferential direction.

ABAQUS offers a broad range of types of elements, and the selection of element affects the accuracy and efficiency of a simulation. Multiple types of elements have been tested to compare the efficiency and the accuracy. To prevent the shear locking induced by linear elements, quadratic interpolated element C3D20R which represents solid element with 20 nodes and reduced integration is used to develop the three-dimensional model. The 4-node reduced-integration planar elements (i.e. S4R) are applied to creat the shell model. The CAX8R (i.e. 8 nodes, reduced integration) element is used to develop the axisymmetric model. The schematic diagrams of three types of models are shown in Figure 2.1.

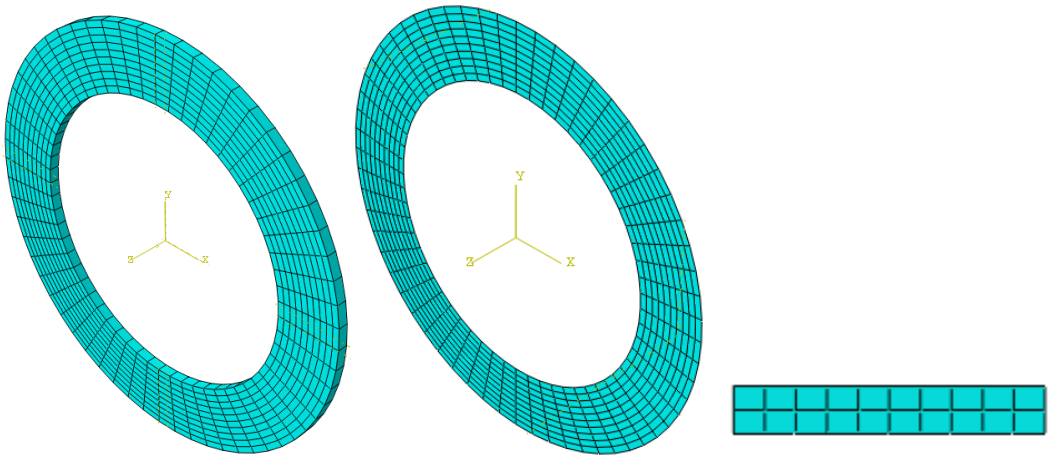

3-D 2-D Axisymmetric

Figure 2.1: Schematic diagrams of three types of models

2.2.3 Analytical Solution

With the intention of verifying the finite element analysis models, we compare the results obtained through FEA simulations with the results gained from analytical calculations. It is assumed that a circular ring can be considered as a curved beam with an annular axis, an analytical algorithm based on Timoshenko's beam theory is proposed by Audebert. Accordingly, the critical bending moment that causes buckling of an annular ring can be calculated. The governing equations are listed below [26,32].

$$K = \frac{1+\nu}{2} \tag{2-10}$$

$$M = \frac{1+K}{2} \pm \sqrt{\left(\frac{1-K}{2}\right)^2 + Kn^2} \tag{2-11}$$

$$M_{cr} = \frac{MGat^3}{3R} \tag{2-12}$$

$$a = R_b - R_a \tag{2-13}$$

$$G = \frac{E}{2(1+\nu)} \tag{2-14}$$

$$R = \frac{R_a + R_b}{2} \quad (2\text{-}15)$$

In the above equations, $K, \nu, M, n, M_{cr}, E, t, R_a$ and R_b represent the stiffness ratio, Poisson's ratio, the dimensionless critical bending moment, the buckling wave number, the critical bending moment, Young's modulus, the thickness, the inner diameter and the outer diameter respectively.

For validation and comparison purpose, the critical buckling temperatures are calculated by using geometric dimensions and material properties mentioned in Ma's work [26]. The geometric and material properties are listted in the following table.

	Inner radius	Outer radius	Thickness	Young's modulus	Poisson's ratio	Thermal expansion
Symbol	R_a	R_b	T	E	ν	α
Unit	mm	mm	mm	Gpa		10-6/k
Value	80	130	6	110	0.3	12.5

Table 2.1: Geometric dimensions and material properties applied in the testing model

The diagrammatic sketch is provided in Figure 2.2.

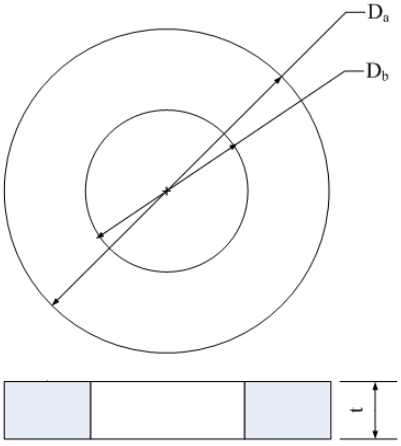

Figure 2.2: The diagrammatic sketch of the testing model

The calculations of first four modes are provided here to illustrate this method.

When n=0,

$$M = \frac{1+K}{2} \pm \frac{1-K}{2} \quad (2\text{-}16)$$

Hence, there are two solutions.

$M_1 = 1, M_2 = K = 0.65$

The smaller value of M should be used to calculate the critical bending moment.

$$M_{cr} = \frac{MGat^3}{3R} = \frac{0.65 \times 4.2308 \times 10^{10} \times 0.05 \times 0.06^3}{3 \times 0.105} = 943N \cdot m \quad (2\text{-}17)$$

When n=1,

$$M = \frac{1+K}{2} \pm \frac{1+K}{2} \quad (2\text{-}18)$$

$M_1 = 1 + K, M_2 = 0$

The smaller one is zero, which means this mode is a rigid body tilting mode rather than a buckling mode.

When n=2,

$$M = \frac{1+K}{2} \pm \sqrt{\left(\frac{1-K}{2}\right)^2 + 4n^2} \quad (2\text{-}19)$$

$M_1 = 2.45, M_2 = -0.8$

$$M_{cr} = \frac{MGat^3}{3R} = 1156N \cdot m \quad (2\text{-}20)$$

When n=3,

$$M = \frac{1+K}{2} \pm \sqrt{\left(\frac{1-K}{2}\right)^2 + 9n^2} \quad (2\text{-}21)$$

$M_1 = 3.25, M_2 = -1.6$

$$M_{cr} = \frac{MGat^3}{3R} = 2321N \cdot m \quad (2\text{-}22)$$

When n=4,

$$M = \frac{1+K}{2} \pm \sqrt{\left(\frac{1-K}{2}\right)^2 + 16n^2} \tag{2-23}$$

$M_1 = 4.05, M_2 = -2.4$

$$M_{cr} = \frac{MGat^3}{3R} = 3488N \cdot m \tag{2-24}$$

Based on Timoshenko's beam theory, the critical bending moments that cause buckling of annular rings can be represented as.

$$M = \int_{R_a}^{R_b} t\sigma_{\theta\theta}(r)(r-R)dr \tag{2-25}$$

If the inner radius and outer radius are not constrained, $\sigma_{\theta\theta}$ can be presented by following equations.

$$\begin{aligned} \sigma_{\theta\theta}(r) &= \frac{\alpha E}{r^2}\int_{R_a}^{r} rT(r)dr - \alpha ET(r) + \frac{EC_1}{1-\nu} + \frac{EC_1}{(1+\nu)r^2} \\ C_1 &= \frac{\alpha}{2(1-\nu)}\frac{1}{R_b^2-R_a^2}\int_{R_a}^{R_b} rT(r)dr \\ C_2 &= \frac{\alpha(1+\nu)R_a^2}{R_b^2-R_a^2}\int_{R_a}^{R_b} rT(r)dr \\ T(r) &= \frac{\Delta T}{R_b-R_a}(r-R_a) \end{aligned} \tag{2-26}$$

where α, $T(r)$ and ΔT represents the thermal expansion, the temperature distribution along radial direction and difference between the temperature at outer radius and the temperature at inner radius respectively.

When the temperature difference ΔT is set as 50 ℃, integrating the above equations by using Matlab, the relation between the critical bending moment and the difference between the temperature at outer radius and the temperature at inner radius can be represented by the following equation.

$$M = -1.693\Delta T \tag{2-27}$$

Thus, the critical buckling temperature differences and eigenvalues calculated by using analytical method are listed in Table 2.2.

Mode	Eigenvalue	ΔT_{cr}	Mode	Eigenvalue	ΔT_{cr}
1	11.14	-557 ℃	3	27.62	1371℃
2	13.66	683 ℃	4	41.22	2061℃

Table 2.2: Eigenvalues and critical temperatures obtained by using analytical method

2.2.4 Numerical Solution and Model Verification

Multiple FEA models have been created to perform convergence test. In the GUI of ABAQUS, the reference thermal load is defined as

$$T = \frac{50}{130-80}(r - 80) \qquad (2\text{-}28)$$

in which the value of temperature is linearly increased from the inner radius to the outer radius. The value of temperature is equal to 0 ℃ at the inner radius and is equal to 50 ℃ at the outer radius. It should be pointed out that the reference temperature is set as a "predefined field" in the FEA model evaluating thermal buckling as shown in Figure 2.3 [52,53 and 54]. In the testing model, neither the inner nor the outer radius is constrained.

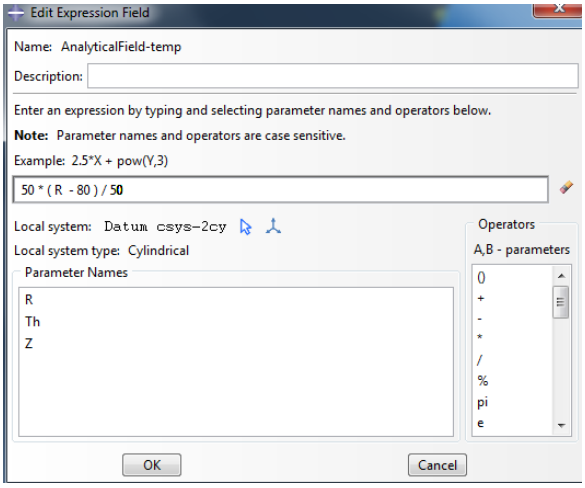

Figure 2.3: The definition of reference thermal load

As mentioned in the previous section, a number of models developed by different kinds of elements (S4R, CAX8R, C3D20R) have been created to test the performances of elements. Meanwhile, to execute the convergence test, the multiple mesh densities have been developed for test purpose. The mesh size is represented by the product of the element numbers along the three directions: radial, thickness and circumferential, respectively. The buckling eigenvalue is selected as the indicator of convergence. The models created by using different element types and different mesh densities are summarized in Table 2.3. The simulated eigenvalues are presented in Figure 2.4 and Figure 2.5.

Element type	1	2	3	4	5	6
S4R	4×16	6×24	8×32	10×48	12×64	14×96
C3D20R	1×4×16	1×6×24	1×8×32	1×10×48	1×12×64	1×14×96
C3D20R	4×4×16	4×6×24	4×8×32	4×10×48	4×12×64	4×14×96
CAX8R	4×4×16	2×6	2×8	2×10	2×12	2×14

Table 2.3: Models used in the convergence study

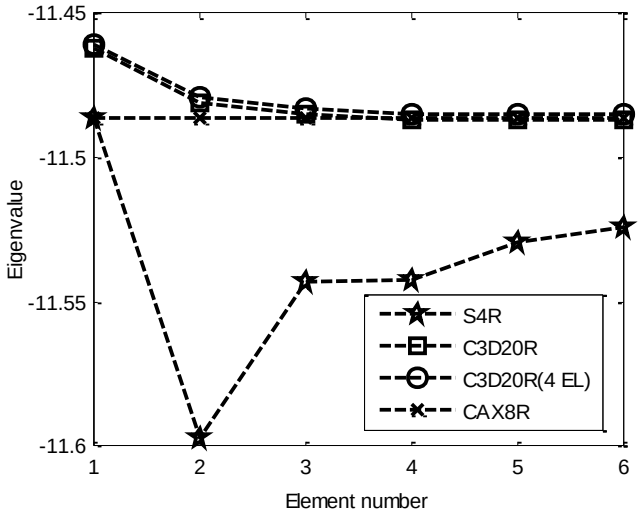

Figure 2.4: The calculated buckling eigenvalues of the 1st dominant mode

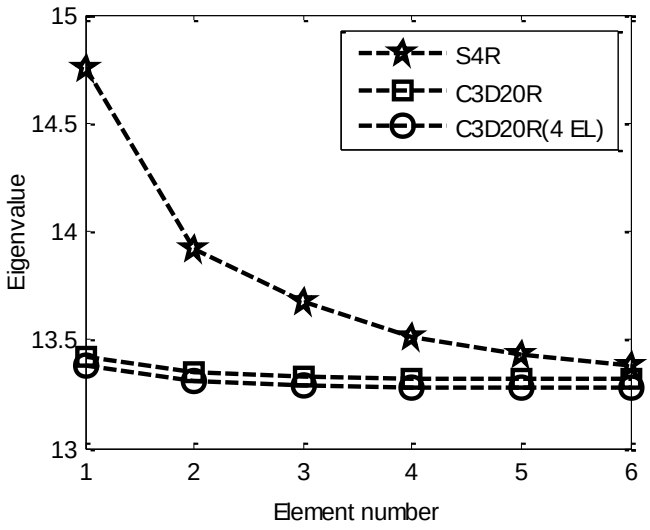

Figure 2.5: The calculated buckling eigenvalues of the 2nd dominant mode

According to results presented in Table 2.3, Figure 2.4 and Figure 2.5, we can obtain multiple preliminary conclusions:

1. With even a very coarse mesh (2×4), the axisymmetric model yields an accurate result for axisymmetric modes.

2. The result gained from the three-dimensional model is accurate when the mesh density is 1×10×48.

3. The shell model provides a small difference around 0.33% with a fine mesh (14×96).

4. The number of elements through the thickness does not impact the calculated result significantly.

It should be mentioned that although the axisymmetric model is the most computationally efficient, it is only appropriate for the cases when both the mode shapes and the applied loads are axisymmetric.

To validate the finite element model, the results obtained from the numerical simulations should be compared with the analytical solutions. The computed eigenvalues and critical buckling temperatures are listed in the following table.

Mode	Eigenvalue	ΔT_{cr}
1	11.487	-574.35
2	13.320	666
3	26.597	1329.85
4	40.135	2006.75

Table 2.4: Eigenvalues and critical temperatures obtained by using FEA analyses

Through the comparison, the largest difference between the numerical result collected from the shell model and the analytical solution is around 2.8%, which is satisfactory. This convergence study shows that the shell model is applicable to investigate the thermal buckling of annular disks. Based on the above comparison, the model built by using the shell elements (i.e. S4R) with a fine mesh (14×96) should be applied in the current study.

2.3 Results

2.3.1 Effects of Different Monotonically Increasing Temperature Variations

During the different operating phases, the working conditions of an automotive clutch system vary. In the initial engaging stage and separation stage, the friction disks of a multi-disc clutch system slide against the metal disks, therefore the frictional heat generation is intense. Depending on the working conditions, numerous types of temperature profiles exist in the clutch plates. The most frequently observed temperature

distributions include linear, exponential and sinusoidal temperature distributions. The sliding speed at a point on the surface of a clutch disk is proportional to its radial position. Meanwhile, the frictional heat generation is linearly increasing with the sliding speed. As a result, the linearly increasing temperature profile can be induced. In the presence of thermoelastic instability (TEI), the sinusoidal distribution can also be induced. The sinusoidal distribution corresponds to the banding mode of TEI in which the temperature varies along the radial direction alone. The exponential profile is introduced by the non-uniform convective heat transfer existing on the surface of the disk or a non-uniform contact pressure on the interfaces between disks.

To obtain more accurate results, the geometric dimensions and material properties of a clutch disk from a real application are selected. These geometric dimensions and material properties are listed in Table 2.5.

	Inner radius	Outer radius	Thickness	Young's modulus	Poisson's ratio	Thermal expansion
Symbol	R_a	R_b	t	E	ν	α
Unit	mm	mm	mm	Gpa		10-6/k
Value	86	125	3	160	0.29	12.7

Table 2.5: Geometric and material parameters of the clutch disk used in the parametric studies

On the basis of the aforementioned assumptions, three types of temperature distributions that are monotonically increasing from the inner radius to the outer radius of a clutch disk have been defined as follows.

$$T_1 = 39\frac{r-86}{125-86} \tag{2-29}$$

$$T_2 = 39\,sin\big(40.28(r-86)\big) \tag{2-30}$$

$$T_3 = 39\,\frac{39(exp(60(r-86))-1)}{241(125-86)} \qquad (2\text{-}31)$$

In the above equations, T_1, T_2 and T_3 correspond to the linear, sinusoidal and exponential temperature profiles respectively. Through these equations, we find that the temperature differences along the radial direction are fixed at 39 °C for all three kinds of temperature profiles. The temperature distributions are also shown in Figure 2.6.

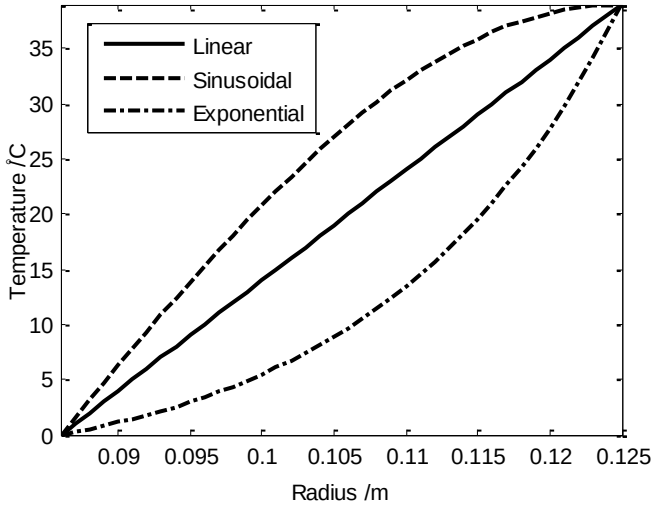

Figure 2.6: Monotonically increasing temperature distributions

The buckling eigenvalues obtained through finite element analyses are shown in Table 2.6.

	Eigenvalue		
Mode	Linear	Sinusoidal	Exponential
1	-4.556	-4.838	-4.916
2	5.444	5.332	5.741
3	10.92	10.82	11.32
4	-11.73	-11.09	-12.99
5	16.49	16.54	16.81

Table 2.6: Buckling eigenvalues of the monotonically increasing temperature distributions

From the above table, it can be found that the eigenvalues of mode 1 and mode 4 are negative, which denotes that the highest temperature is located at the inner radius and the lowest temperature is located at the outer radius. The calculated buckling temperatures obtained from finite element analyses are shown Figure 2.7.

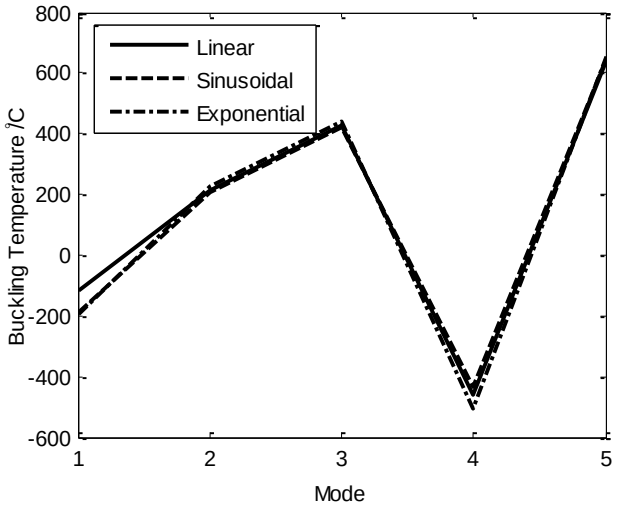

Figure 2.7: Buckling temperatures of the monotonically increasing temperature distributions

From the above figure, we can discover that the buckling temperatures of the dominant mode are around 178 °C for monotonic temperature profiles, which is obviously lower than real operating temperatures of clutch systems. However, as the clutch disk is not constrained at either inner radius or outer radius, these eigenvalues and buckling temperatures represent the lower bound of thermal buckling of the clutch disk. It is expected that if the inner or outer radius is fixed the eigenvalues and critical buckling temperatures will be elevated. Through Figure 2.7, we also conclude that the patterns of thermal loads do not affect the calculated eigenvalues and critical buckling temperatures evidently. The critical buckling temperatures of the first buckling modes (i.e. Mode 1 and

Mode 2) are around -200 °C and 200 °C. In comparison with higher modes, these values are significantly lower. Therefore, the first two modes are dominant. The deformed shapes of the first two modes are shown in Figure 2.8.

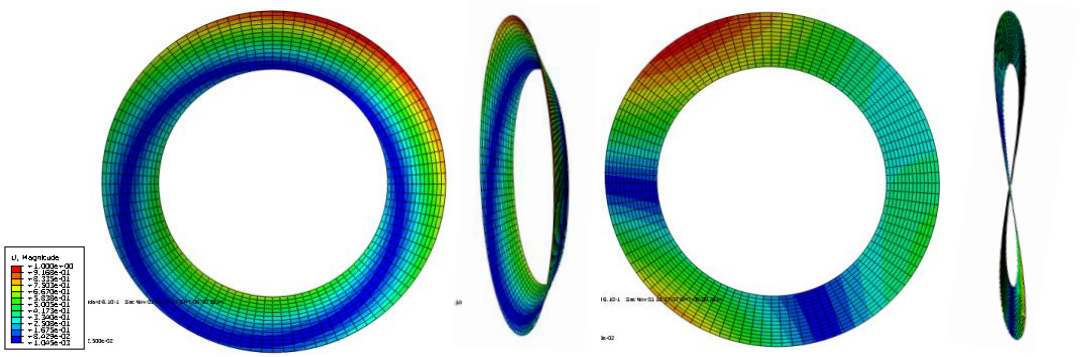

(a) Linear temperature distribution

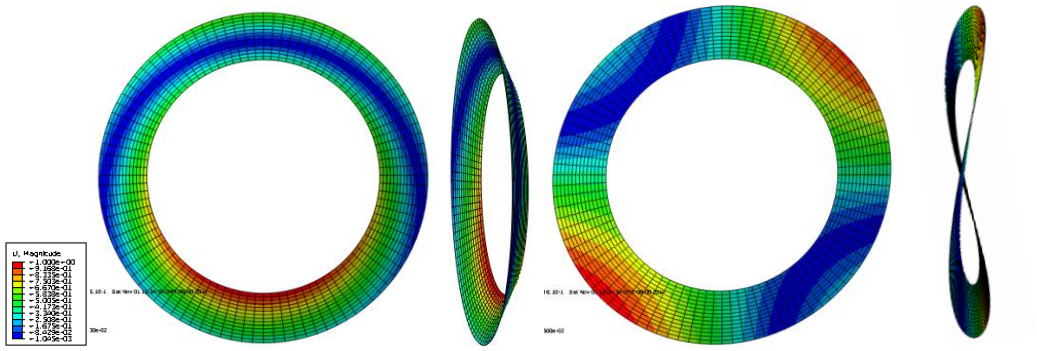

(b) Sinusoidal temperature distribution

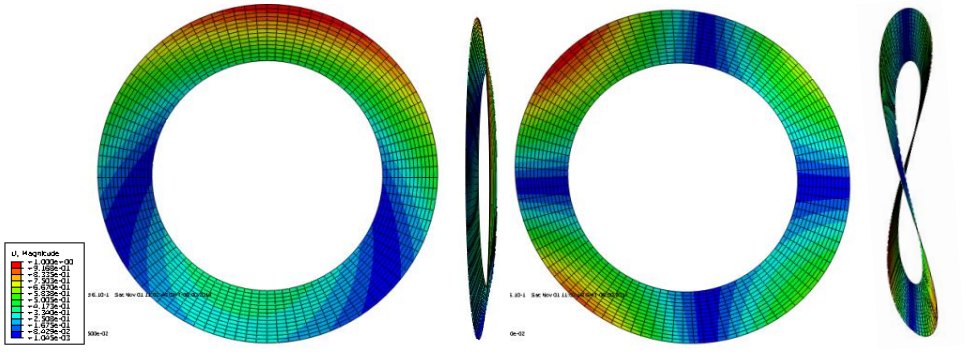

(c) Exponential temperature distribution

Mode 1 Mode 2

Figure 2.8: Buckling modes of the monotonically increasing temperature distributions

From Figure 2.8, it shows that the configurations of the first mode of all three conditions are always axisymmetric and the deformed shapes of the second mode are always non-axisymmetric when the temperature distributions are increasing or decreasing monotonically along the radial direction. Nevertheless, the axisymmetric mode exists only when the temperature is decreasing along the radius of the disk. Rather than buckling mode, the temperature distributions change the deformed shapes significantly. As a result, it can be discovered that the thermal loads that are increasing or decreasing monotonically in the radial direction influence the deformed shape rather than the thermal buckling mode and the buckling temperature.

2.3.2 Effects of Different Non-monotonic Radial Temperature Variations

To evaluate the thermal buckling behavior of clutch disks more systematically, another set of temperature distributions have been created. These temperature profiles are defined by the following expressions.

$$T_4 = \begin{cases} \frac{78(r-86)}{125-86}, (86 \le r \le 105.5) \\ 78 - \frac{78(r-86)}{125-86}, (105.5 \le r \le 125) \end{cases} \quad (2\text{-}32)$$

$$T_5 = 39\, sin\big(80.56(r-86)\big) \quad (2\text{-}33)$$

$$T_6 = \begin{cases} \frac{39\left(exp\left(120(r-86)\right)-1\right)}{240.5(125-86)}, (86 \le r \le 105.5) \\ \frac{39\left(exp\left(120(-r+125)\right)-1\right)}{240.5(125-86)}, (105.5 \le r \le 125) \end{cases} \quad (2\text{-}34)$$

In the above equations, T_4, T_5 and T_6 correspond to the linear, sinusoidal and exponential temperature profiles respectively. Through these equations, we find that the temperature differences along the radial direction are fixed at 39 °C for all three types of

temperature profiles. The temperature distributions are shown in Figure 2.9, through which we find that the maximum temperatures are located at the medium radii.

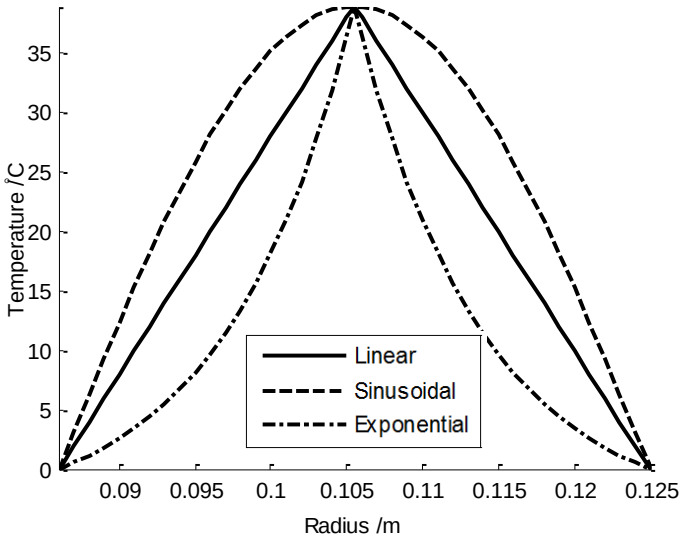

Figure 2.9: Non-monotonic temperature distributions

	Eigenvalue		
Mode	Linear	Sinusoidal	Exponential
1	-46.21	-42.51	-53.25
2	-56.14	-51.69	-64.59
3	-61.88	-56.94	-71.23
4	-67.05	-61.63	-77.29
5	69.62	64.56	79.17

Table 2.7: Buckling eigenvalues of the non-monotonic radial temperature profiles

The buckling eigenvalues are listed in the above table. Compared to Tables 2.6 and 2.7, it is obviously shown that the eigenvalues obtained from temperature distributions in which the peak values are located at the medium radii are higher than the eigenvalues obtained from models with monotonic temperature profiles by around ten times. Actually, under non-monotonic temperature profiles, the calculated buckling temperatures are above the working temperatures of clutch systems. Therefore, thermal

buckling is more likely to occur under monotonic radial temperature profiles. The buckled configurations of the first two buckling modes are shown in Figure 2.10.

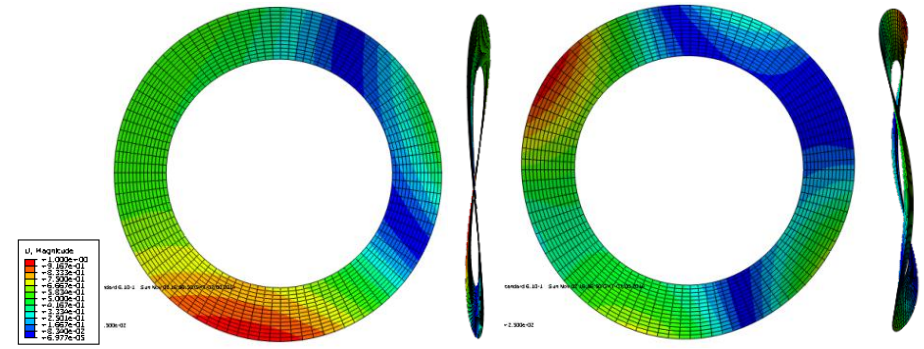

(a) Linear temperature distribution

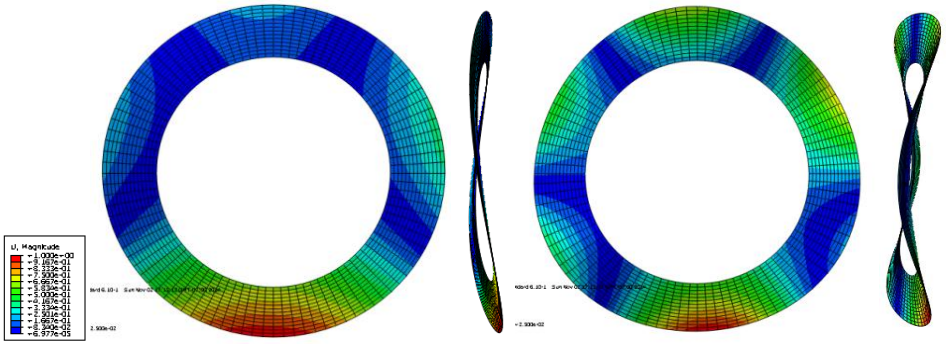

(b) Sinusoidal temperature distribution

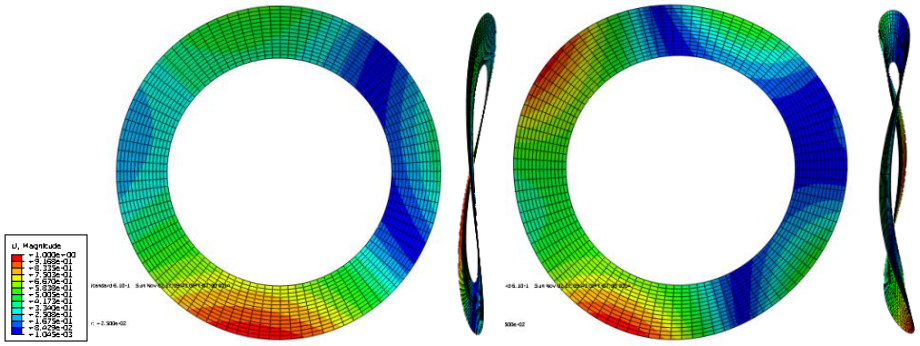

(c) Exponential temperature distribution

Mode 1 Mode 2

Figure 2.10: Buckling modes of the non-monotonic temperature distributions

From Figure 2.10, it shows that the configurations of first and second modes of all three types of thermal loads are always non-axisymmetric when the temperature distributions are non-monotonic. Meanwhile, the coning mode does not exist under this

condition. It also reveals that the temperature distributions change the deformed shapes significantly.

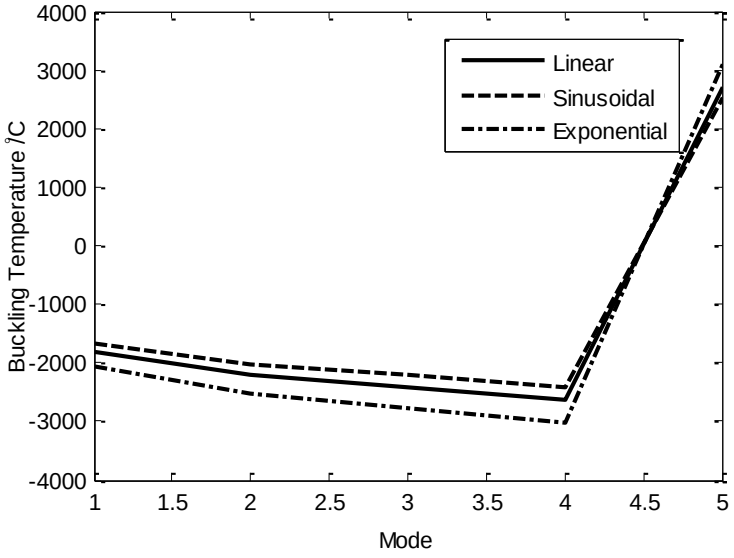

Figure 2.11: Buckling temperatures of the non-monotonic temperature distributions

The calculated critical buckling temperatures are presented in above figure. From Figure 2.10 and Figure 2.11, it is shown that the temperature profiles influence the deformed shape significantly rather than the thermal buckling mode or the buckling temperature.

2.3.3 Effects of Temperature Distributions Varying Circumferentially

If TEI exists, the temperature distribution may vary periodically along the circumferential direction, due to the existence of the hot spots. In this subsection, a thermal load changing periodically along the circumferential direction has been defined. The thermal load can be expressed as the following function.

$$T_7 = 39\,sin(n\theta)\; n = 0.5,1.5 \qquad (2\text{-}35)$$

where n and θ represent the number of hot spots and the angular coordinate. The calculated buckling eigenvalues are reported in Table 2.8, and the deformed configurations of first two modes are shown in Figure 2.12.

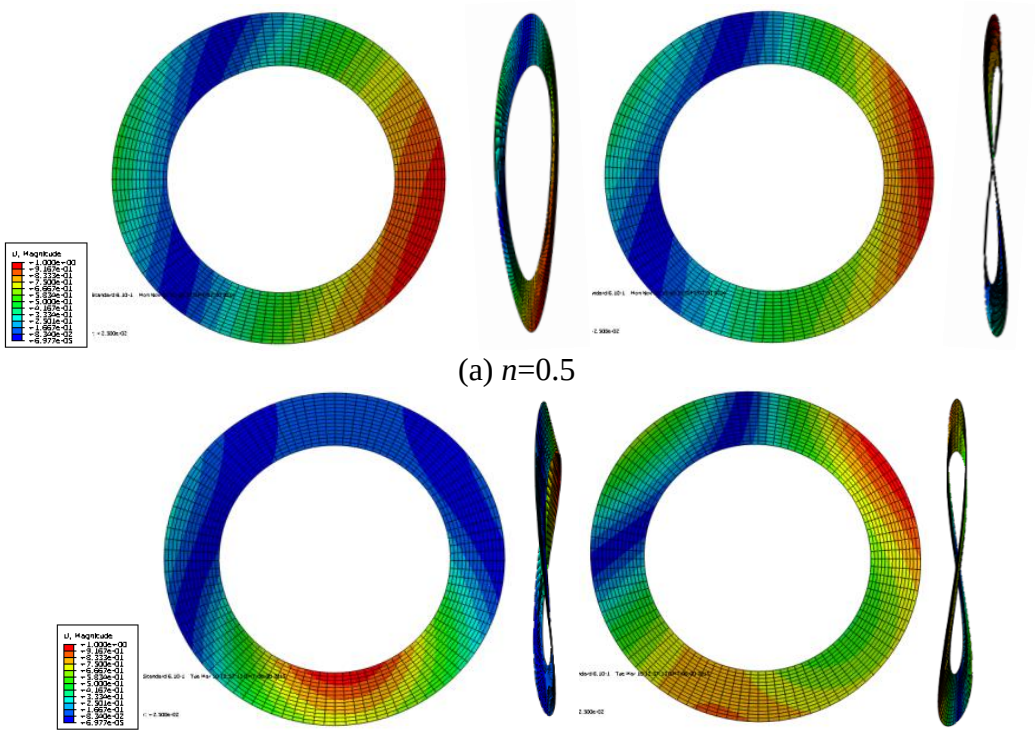

(a) n=0.5

(c) n=1.5

Mode 1 Mode 2

Figure 2.12: Dominant buckling modes of the sinusoidal temperature distributions along the circumference

From the calculated results, we find that the critical buckling temperature of mode 1 is 1785 ℃ when n is equal to 1.5, and is 1071 ℃ when n is equal to 0.5. Therefore, the tendency that the simulated buckling temperatures increase with the number of hot spots can be discovered. These calculated critical buckling temperatures are higher than that of monotonically increasing thermal loads, and are higher than the working temperatures of automotive clutch systems.

	Eigenvalue	
Mode	n=0.5	n=1.5
1	27.46	45.76
2	43.43	71.52
3	60.36	98.70
4	63.03	105.1

Table 2.8: Buckling eigenvalues of the sinusoidal temperature profiles in the circumference

2.4 Conclusions

The thermal buckling phenomenon occurring among clutch disks has been evaluated through a set of finite element analyses. It shows that the axisymmetric temperature distributions which vary in the radial direction can cause thermal buckling of clutch disks. It also has been found that the different types of temperature distributions along the radius of the disk impact both the critical buckling temperatures and the dominant buckling modes apparently. For a reference thermal load increasing monotonically along the radial direction, the simulated dominant buckling mode is always the axisymmetric mode. However, the actual temperature decreases from the inner radius to the outer radius. For a reference thermal load that increase monotonically in the radial direction, the non-axisymmetric modes can also occur, but the corresponding buckling temperatures are much higher.

When the maximum temperatures of reference thermal loads are located at the medium radii, the non-axisymmetric buckling modes are with lowest critical buckling temperatures among all existing modes. In other words, they are dominant modes. Meanwhile, their buckling temperatures are significantly higher than that of monotonically distributed temperature profiles.

It is revealed that when the temperature differences of different types (i.e. linear, sinusoidal and exponential) of reference thermal loads are the same, the buckling temperatures are not considerably affected. Whereas, the simulated thermal buckling mode shapes are greatly impacted.

A periodically varying temperature field has also been tested. However, due to the numerical difficulties, the numerical results are not convergent.

3 A FOURIER FINITE ELEMENT MODEL FOR PREDICTION OF THERMAL BUCKLING IN DISC CLUTCHES AND BRAKES

3.1 Introduction

Frictional heat generation during the engagements of automotive clutch systems and the braking processes result in thermal stresses. The thermal stresses can lead to thermoelastic instability (TEI) and thermal buckling. The buckling mode with the lowest critical buckling temperature is dominant and with the most practical importance. Finite element analyses can be performed to evaluate thermal buckling of annular rings through commercial software such as ABAQUS [52]. However, through my study described in Chapter two of this dissertation, it was found that the calculated eigenvalues of different buckling modes are actually very close. This phenomenon is serious when three-dimensional models are applied to evaluate the thermal buckling of clutch disks. As a result, it is essential for researchers to sort the simulated buckling modes manually according to the deformation shapes. Therefore, studying the eigenvalue as a function of the circumferential deformation wave number is not convenient. Conversely, taking advantage of the axisymmetric shapes seems beneficial when both the temperature distributions and the deformed configurations shape are axisymmetric. By applying the axisymmetric element library available in commercial software, the coning thermal buckling modes can be studied. However, it was discovered that at certain situations the critical buckling temperatures of coning modes are higher than the critical buckling

temperatures of the non-axisymmetric modes. Therefore, developing axisymmetric models is insufficient when both the deformation configurations and thermal stresses are non-axisymmetric.

For solving the thermal buckling problems of axisymmetric geometries, the implement of the Fourier method is the best choice. The algorithm used in this research is modified from the methodology applied to the analyses of thermoelastic instability in automotive brakes and clutches [22] and thermoelastic damping in MEMS systems [45,46]. Although the principles of these problems are significantly different, the Fourier scheme can be applied to reduce the dimensionality. As the configurations of brake disks and clutch disk can be presented as annular rings, the thermal loads and displacement fields can be expressed in the Fourier terms. Therefore, the circumferential dependence of the variables can be eliminated from the governing equations. This mechanism reduces the finite element formation of an annular solid body to the finite element formation of a cross-section of the annular solid body. Through this method, the computational cost is significantly reduced. However, the degrees of freedom of each node in the radial, axial and circumferential directions are retained.

3.2 Method

As described in the theory of elasticity, the geometric nonlinearity during the deformation of a structure leads to the buckling. To account the geometric nonlinearity, an additional stiffness term should be inserted to the governing equation. In the finite element formulation of the buckling problem of a certain structure, the *stress stiffness*

matrix $[K_\sigma]$ is needed to added to the stiffness matrix $[K]$. The equation defining the eigenvalue problem of the buckling load is provided below [50,51].

$$\left([K] + \lambda_{cr}[K_\sigma]_{ref}\right)\{\delta D\} = \{0\} \tag{3-1}$$

In equation (3-1), λ_{cr} is the buckling eigenvalue. Vector $\{\delta D\}$ contains the buckling displacement components which can be induced by either mechanical loads or temperature distributions.

The stress stiffness matrix can be connected to the geometric nonlinearity through the Green tensor [55]. In general, the Green strain tensor, *E*, contains both the linear terms and nonlinear terms. The Green tensor is defined by the following equation [56].

$$E = \frac{1}{2}(F^T \cdot F - I) \tag{3-2}$$

In above equation, the matrix *I* is the identity matrix, and the matrix *F* represents the deformation gradients. The matrix *F* can be obtained by Equation 3-3.

$$F = \begin{bmatrix} 1 + \frac{\partial u_r}{\partial r} & \frac{1}{r}\frac{\partial u_r}{\partial \theta} - \frac{u_\theta}{r} & \frac{\partial u_r}{\partial z} \\ \frac{\partial u_\theta}{\partial r} & 1 + \frac{1}{r}\frac{\partial u_\theta}{\partial \theta} + \frac{u_r}{r} & \frac{\partial u_\theta}{\partial z} \\ \frac{\partial u_z}{\partial r} & \frac{1}{r}\frac{\partial u_z}{\partial \theta} & 1 + \frac{\partial u_z}{\partial z} \end{bmatrix} \tag{3-3}$$

In cylindrical coordinates, the linear terms of strains are defined as following equation [57].

$$\varepsilon = \begin{Bmatrix} \varepsilon_r \\ \varepsilon_z \\ \varepsilon_\theta \\ \gamma_{rz} \\ \gamma_{z\theta} \\ \gamma_{\theta r} \end{Bmatrix} = \begin{Bmatrix} \frac{\partial u_r}{\partial r} \\ \frac{\partial u_z}{\partial z} \\ \frac{u}{r} + \frac{1}{r}\frac{\partial u_\theta}{\partial \theta} \\ \frac{\partial u_r}{\partial z} + \frac{\partial u_z}{\partial r} \\ \frac{\partial u_\theta}{\partial z} + \frac{1}{r}\frac{\partial u_z}{\partial \theta} \\ \frac{1}{r}\frac{\partial u_r}{\partial \theta} + \frac{\partial u_\theta}{\partial r} - \frac{u_\theta}{r} \end{Bmatrix} \tag{3-4}$$

In above equation, u_r, u_θ, u_z represnt the displacement in the radial direction, the displacement in the circumferential and the displacement in the axial direction, respectively. Through subtracting the linear terms from the Green strains, nonlinear terms can be obtained:

$$\Delta E = \begin{bmatrix} \Delta E_{11} & \Delta E_{12} & \Delta E_{13} \\ \Delta E_{21} & \Delta E_{22} & \Delta E_{23} \\ \Delta E_{31} & \Delta E_{32} & \Delta E_{33} \end{bmatrix} \quad (3\text{-}5)$$

where

$$\Delta E_{11} = \frac{1}{2}\left[\left(\frac{\partial u_r}{\partial r}\right)^2 + \left(\frac{\partial u_\theta}{\partial r}\right)^2 + \left(\frac{\partial u_z}{\partial r}\right)^2\right] \quad (3\text{-}6)$$

$$\Delta E_{12} = \frac{1}{2}\left[-\frac{u_\theta}{r}\frac{\partial u_r}{\partial r} + \frac{u_r}{r}\frac{\partial u_\theta}{\partial r} + \frac{1}{r}\frac{\partial u_r}{\partial \theta}\frac{\partial u_r}{\partial r} + \frac{1}{r}\frac{\partial u_\theta}{\partial r}\frac{\partial u_\theta}{\partial \theta} + \frac{1}{r}\frac{\partial u_z}{\partial r}\frac{\partial u_z}{\partial \theta}\right] \quad (3\text{-}7)$$

$$\Delta E_{13} = \frac{1}{2}\left[\frac{\partial u_r}{\partial r}\frac{\partial u_r}{\partial z} + \frac{\partial u_\theta}{\partial r}\frac{\partial u_\theta}{\partial z} + \frac{\partial u_z}{\partial r}\frac{\partial u_z}{\partial z}\right] \quad (3\text{-}8)$$

$$\Delta E_{22} = \frac{1}{2}\left[\left(\frac{u_\theta}{r}\right)^2 + \left(\frac{u_r}{r}\right)^2 - \frac{2u_\theta}{r^2}\frac{\partial u_r}{\partial \theta} + \frac{2u_r}{r^2}\frac{\partial u_\theta}{\partial \theta} + \frac{1}{r^2}\left(\frac{\partial u_r}{\partial \theta}\right)^2 + \frac{1}{r^2}\left(\frac{\partial u_\theta}{\partial \theta}\right)^2 + \frac{1}{r^2}\left(\frac{\partial u_z}{\partial \theta}\right)^2\right] \quad (3\text{-}9)$$

$$\Delta E_{23} = \frac{1}{2}\left[-\frac{u_\theta}{r}\frac{\partial u_r}{\partial z} + \frac{u_r}{r}\frac{\partial u_\theta}{\partial z} + \frac{1}{r}\frac{\partial u_r}{\partial \theta}\frac{\partial u_r}{\partial z} + \frac{1}{r}\frac{\partial u_\theta}{\partial \theta}\frac{\partial u_\theta}{\partial z} + \frac{1}{r}\frac{\partial u_z}{\partial \theta}\frac{\partial u_z}{\partial z}\right] \quad (3\text{-}10)$$

$$\Delta E_{33} = \frac{1}{2}\left[\left(\frac{\partial u_r}{\partial z}\right)^2 + \left(\frac{\partial u_\theta}{\partial z}\right)^2 + \left(\frac{\partial u_z}{\partial z}\right)^2\right] \quad (3\text{-}11)$$

$$\Delta E_{21} = \Delta E_{12} \quad (3\text{-}12)$$

$$\Delta E_{31} = \Delta E_{13} \quad (3\text{-}13)$$

$$\Delta E_{32} = \Delta E_{23} \quad (3\text{-}14)$$

According to the Fourier algorithm, the temperature distributions and displacements are expressed as follows

$$\begin{cases} T = \Theta\, cos(p\theta) \\ u_r = U_r\, cos(p\theta) \\ u_\theta = U_\theta\, cos(p\theta) \\ u_z = U_z\, cos(p\theta) \end{cases} \tag{3-15}$$

in which p represents the temperature wave number (i.e. "hot spot" number) in the circumferential direction; n represents the displacement wave number along the circumferential direction. In general, the values of p and n are not necessarily identical. For example, an axisymmetric temperature distribution (p=0) can cause both axisymmetric modes (n=0) and wavy modes (n≠0).

According to [50, 51], the stress stiffness matrix is determined by the following equation.

$$[K_\sigma] = \int [G]^T \begin{bmatrix} S & 0 & 0 \\ 0 & S & 0 \\ 0 & 0 & S \end{bmatrix} [G] dV \tag{3-16}$$

In above equation, V is the volume; G can be determined through the nonlinear terms ΔE contained in the Green tensor and the shape functions [N]. The matrix [s] is the thermal stress components introduced by the reference temperature distribution.

$$[s] = \begin{bmatrix} \sigma_{rr} & \sigma_{r\theta} & \sigma_{zr} \\ \sigma_{r\theta} & \sigma_{\theta\theta} & \sigma_{\theta z} \\ \sigma_{zr} & \sigma_{\theta z} & \sigma_{zz} \end{bmatrix} \tag{3-17}$$

The relation between the temperature and the induced thermal stresses is defined by the following equation.

$$\sigma = [C]\varepsilon - [D]T \tag{3-18}$$

In above equation, the coefficient matrix [C] is the stress-strain relationship which is defined by the following equation.

$$[C] = \frac{E}{(1+\nu)(1-2\nu)} \begin{bmatrix} 1-\nu & \nu & \nu & 0 & 0 & 0 \\ \nu & 1-\nu & \nu & 0 & 0 & 0 \\ \nu & \nu & 1-\nu & 0 & 0 & 0 \\ 0 & 0 & 0 & 1-2\nu & 0 & 0 \\ 0 & 0 & 0 & 0 & 1-2\nu & 0 \\ 0 & 0 & 0 & 0 & 0 & 1-2\nu \end{bmatrix} \quad (3\text{-}19)$$

In above equation, E represents elastic modulus and ν represents Poisson's ratio, D is associated with thermal expansions

$$[D] = \frac{E\alpha}{1-2\nu}[1 \quad 1 \quad 1 \quad 0 \quad 0 \quad 0]^T \quad (3\text{-}20)$$

The strain vector ε is obtained from the vector U containing nodal displacements through following equations:

$$\varepsilon = [B]U \quad (3\text{-}21)$$

$$[B] = [B_1 \quad B_2 \quad B_3 \quad B_4] \quad (3\text{-}22)$$

$$[B_i] = \begin{bmatrix} \frac{\partial N_i}{\partial r} & 0 & 0 \\ \frac{N_i}{r} & \frac{nN_i}{r} & 0 \\ 0 & 0 & \frac{\partial N_i}{\partial z} \\ -\frac{nN_i}{2r} & \frac{1}{2}\left(\frac{\partial N_i}{\partial r} - \frac{N_i}{r}\right) & 0 \\ 0 & \frac{1}{2}\frac{\partial N_i}{\partial z} & -\frac{nN_i}{2r} \\ \frac{1}{2}\frac{\partial N_i}{\partial z} & 0 & \frac{1}{2}\frac{\partial N_i}{\partial r} \end{bmatrix} \text{ (i=1,2,3,4)} \quad (3\text{-}23)$$

In above equations, σ and ε are stresses and strains induced by temperature distributions. As the temperature distribution varies with $\cos(p\theta)$, σ also varies with $\cos(p\theta)$. It implies that the nonlinear terms in the Green strains ΔE would be zero if both

n and *p* are non-zero integers, which leads to a zero stress stiffness matrix, due to the following orthogonality relationships of the sine and cosine functions:

$$\begin{cases} \int_0^{2\pi} cos^2(n\theta)\, cos(p\theta) d\theta = 0 \\ \int_0^{2\pi} sin^2\big((n\theta)\big)\, cos(p\theta) d\theta = 0 \\ \int_0^{2\pi} cos(n\theta)\, sin(n\theta)\, cos(p\theta) d\theta = 0 \end{cases} \quad (3\text{-}24)$$

If the temperature distribution is axisymmetric (p=0), the following equations can be derived.

$$[K_\sigma]^{\{r\}} = \iint \left[\sigma_{rr} \frac{\partial[N]}{\partial r}\frac{\partial[N]^T}{\partial r} + \sigma_{\theta\theta}\frac{(n^2+1)}{r^2}[N][N]^T + \sigma_{zz}\frac{\partial[N]}{\partial r}\frac{\partial[N]^T}{\partial r} + \sigma_{rz}\left(\frac{\partial[N]}{\partial r}\frac{\partial[N]^T}{\partial z} + \frac{\partial[N]}{\partial z}\frac{\partial[N]^T}{\partial r}\right)\right] r dr dz \quad (3\text{-}25)$$

$$[K_\sigma]^{\{\theta\}} = [K_\sigma]^{\{r\}} \quad (3\text{-}26)$$

$$[K_\sigma]^{\{z\}} = \iint \left[\sigma_{rr} \frac{\partial[N]}{\partial r}\frac{\partial[N]^T}{\partial r} + \sigma_{\theta\theta}\frac{n^2}{r^2}[N][N]^T + \sigma_{zz}\frac{\partial[N]}{\partial r}\frac{\partial[N]^T}{\partial r} + \sigma_{rz}\left(\frac{\partial[N]}{\partial r}\frac{\partial[N]^T}{\partial z} + \frac{\partial[N]}{\partial z}\frac{\partial[N]^T}{\partial r}\right)\right] r dr dz \quad (3\text{-}27)$$

When both the temperature distribution and the displacement field are axisymmetric (*n*=*p*=0 and U_θ=0), the following equations can be derived.

$$[K_\sigma]^{\{r\}} = \iint \left[\sigma_{rr} \frac{\partial[N]}{\partial r}\frac{\partial[N]^T}{\partial r} + \sigma_{\theta\theta}\frac{1}{r^2}[N][N]^T + \sigma_{zz}\frac{\partial[N]}{\partial r}\frac{\partial[N]^T}{\partial r} + \sigma_{rz}\left(\frac{\partial[N]}{\partial r}\frac{\partial[N]^T}{\partial z} + \frac{\partial[N]}{\partial z}\frac{\partial[N]^T}{\partial r}\right)\right] r dr dz \quad (3\text{-}28)$$

$$[K_\sigma]^{\{z\}} = \iint \left[\sigma_{rr} \frac{\partial[N]}{\partial r}\frac{\partial[N]^T}{\partial r} + \sigma_{zz}\frac{\partial[N]}{\partial r}\frac{\partial[N]^T}{\partial r} + \sigma_{rz}\left(\frac{\partial[N]}{\partial r}\frac{\partial[N]^T}{\partial z} + \frac{\partial[N]}{\partial z}\frac{\partial[N]^T}{\partial r}\right)\right] r dr dz \quad (3\text{-}29)$$

The stiffness matrix *[K]* can be expressed as following equation [22].

$$[K_e] = \iint_\pi [B]^T [C][B] r dr dz \quad (3\text{-}30)$$

The aforementioned Fourier finite element algorithm has been integrated into a Matlab code, in which the eigenvalue equation is solved to find the critical buckling eigenvalue through the built-in eigenvalue solver *eig*.

3.3 Results

3.3.1 Convergence Study

To validate the method mentioned in the previous section, we performed a convergence test. The critical buckling temperature is selected as the indicator of convergence. In the convergence test, both the inner radii and outer radii of annular disks are free; and the circumferential wave number is fixed at 0. The material properties and geometric dimensions are tabulated in Table 3.1.

	Inner radius	Outer radius	Thickness	Young's modulus	Poisson's ratio	Thermal expansion
Symbol	R_a	R_b	t	E	ν	α
Unit	mm	mm	mm	Gpa		10-6/k
Value	86	125	3	160	0.29	12.7

Table 3.1: Geometric parameters and material properties of the clutch plate used in the thermal buckling models

The axisymmetric mode shape has been assumed so that the circumferential wave number is set to zero in the analysis. The cross-section of the disk is discretized by applying the axisymmetric elements with the linearly interpolated shape functions. The temperature is assumed as linearly increased from the inner radius to the outer radius. The value of temperature is 0 at the inner radius; and the value of temperature at outer radius is equal to 1 °C. As a result, the calculated *buckling temperature* is equivalent to the simulated buckling eigenvalue. A positive eigenvalue implies that the temperature

profile is increasing along the radial direction, whereas a negative eigenvalue shows the temperature is decreasing along the radial direction.

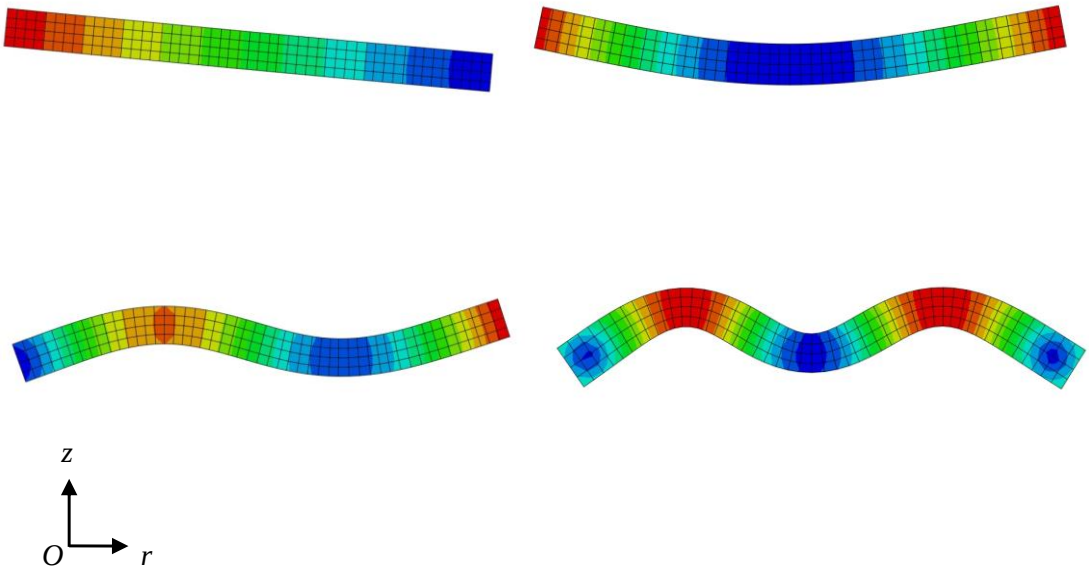

Figure 3.1: The dominant four axisymmetric buckling modes for an annular ring with free boundaries

The first four dominant buckling modes obtained through the FEA analyses are plotted in Figure 3.1. The simulated critical buckling temperatures of these modes are the lowest ones among all calculated results. The colors in Figure 3.1 denote the values of the values of nodal displacement in the axial (thickness) direction. In the convergence test, the number of elements in the thickness direction is fixed at 5. Meanwhile, the element number aling the radius (m) increases from 5 and 100. The relationship between the buckling temperatures and the element number along the radius is presented in Figure 3.2. The results of the convergence test for the first three modes are shown in Figure 3.2. The dominant mode is a coning mode in which the displacement in the axial direction is linearly distributed along the radius. The computed buckling temperature is -185.9 °C when m is equal to 5; and the computed buckling temperature is -178.3 °C if the element

along the radius direction reaches 100. The error between the simulated critical buckling is only 4% which implies an outstanding convergence rate for the first mode. The negative critical buckling temperature of the first mode implies that the temperature distribution is actually decreasing in the radial direction. The critical buckling temperature was also compared with the result obtained from the ABAQUS model in which the axisymmetric elements (CAX4I) were applied. As shown in Figure 3.2, the buckling temperature obtained from the ABAQUS model is -177.0 °C at *m*=100.

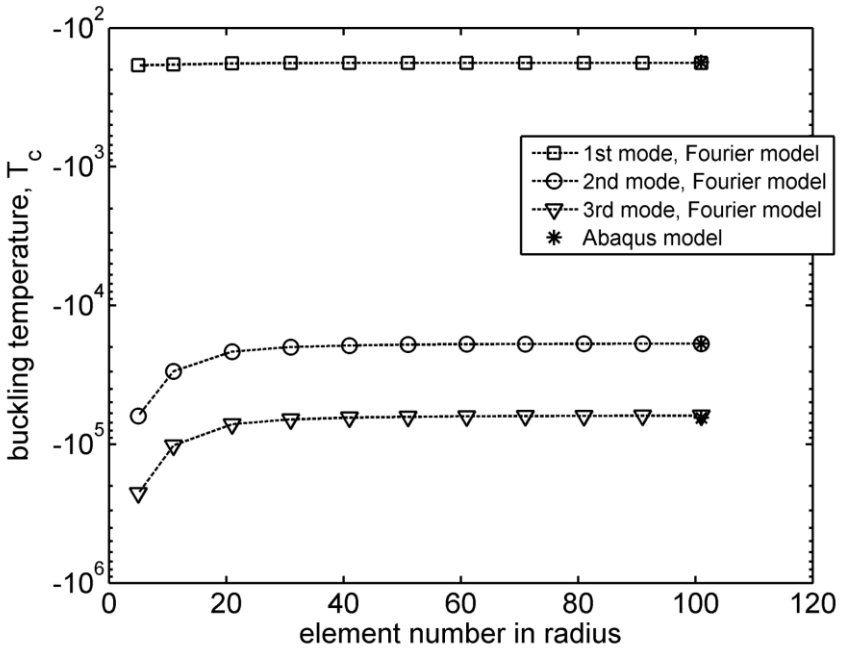

Figure 3.2: A convergence study on the relationship between the buckling temperature and the element number in the radial direction

Among higher-order buckling modes, the deformation patterns have nonlinear profiles in which there are multiple reversals along the radii of the disks. The computed buckling temperatures converge when the number of elements along the radial direction reach 50, but deviates significantly when the number of elements along the radial

direction are less than 20. It can be confirmed that 50 elements in the radial direction are sufficient to yield acceptable results. It is also discovered that the buckling temperatures of second and third modes are significantly higher than that of the first mode. Normally, the working temperatures of clutch systems are below 1000 °C. As a result, it can be concluded that the coning mode is the only axisymmetric mode with practical importance.

3.3.2 Effects of Boundary Conditions

For the Euler bar problem, the boundary conditions affect the critical buckling loads obviously. It is expected that the boundary conditions also influence the buckling behaviors of annular disks.

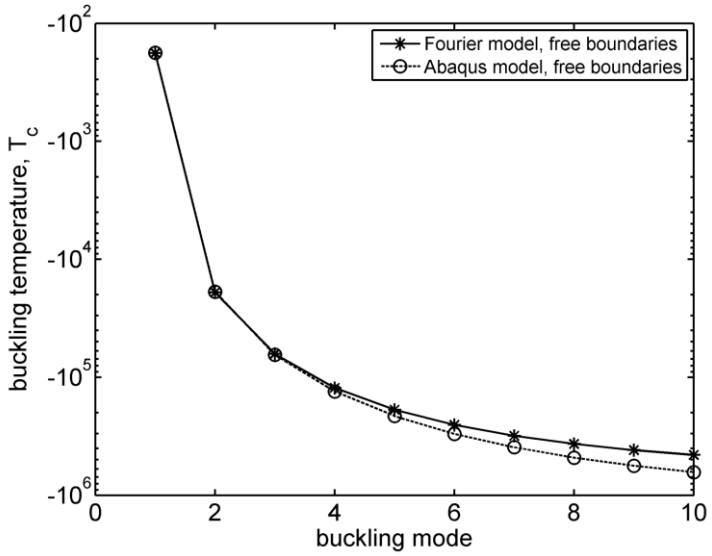

Figure 3.3: Comparison of the computed buckling temperature between the Fourier model and Abaqus for an annular ring with free boundaries

When the inner and outer radii are not constrained, the relation between the calculated buckling temperatures and the buckling modes obtained through the Fourier model and Abaqus model are shown in Figure 3.3. In the current research, there are 50

elements in the radial direction for all models. The critical buckling temperatures of the first three buckling modes obtained through the two methods are very close. Meanwhile, starting from the fourth mode, the two curves deviate from each other. It is possible because the different interpolating functions and the different integration methods have been applied in the two models.

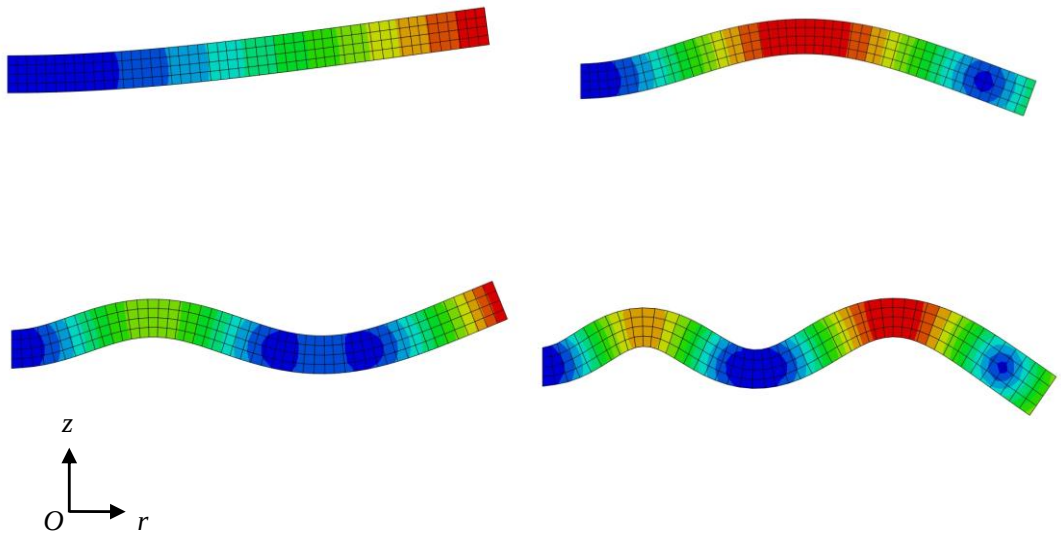

Figure 3.4: The dominant four axisymmetric buckling modes for an annular ring with fixed inner radius

The first four buckling modes of a clutch disk with a fixed inner radius are presented in Figure 3.4. The relation between the buckling temperatures and the buckling modes of the clutch disk with a fixed inner radius is plotted in Figure 3.5.

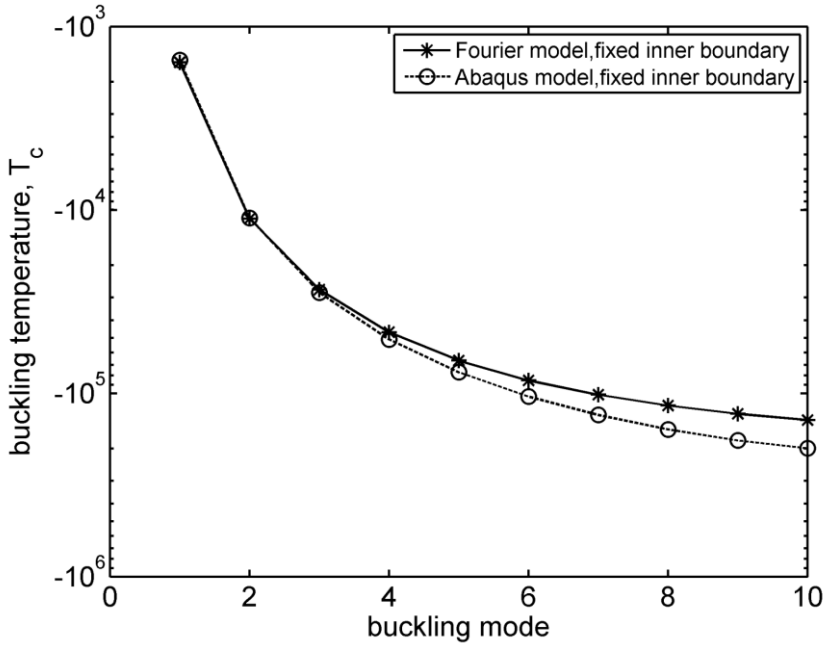

Figure 3.5: Comparison of the computed buckling temperature between the Fourier model and Abaqus for an annular ring with fixed inner radius

It is also discovered that the simulated critical buckling temperatures of the first three modes agree with each other well, but the difference becomes larger starting from the fourth mode. The discrepancy between the results obtained through different methods is around 10% for the fourth buckling mode. We also discovered that the buckling temperatures obtained through the model with a fixed inner radius are much higher than those of the model with a free inner radius.

3.3.3 Non-axisymmetric Buckling Modes

Through the aforementioned results of axisymmetric buckling modes, it is found that the critical buckling temperatures are significantly higher than the working temperatures in practical applications; and these values are only with theoretical importance except for the first mode (i.e. coning mode). The critical buckling

temperatures of nonaxisymmetric modes are much lower, and therefore the nonaxisymmetric modes are with more practical importance. The nonaxisymmetric modes have also been studied by setting the displacement wave number as non-zero integers. In this part of the research, the thermal loads are also assumed to be axisymmetric. To prevent the solid body motions, the inner radius is assumed to be fully fixed.

The simulated buckled configurations are presented in Figure 3.6. It shows that Mode A is the coning mode. Modes B thru F are nonaxisymmetric modes. The dominant mode is Mode D with n=6, as its critical buckling temperature is the lowest one.

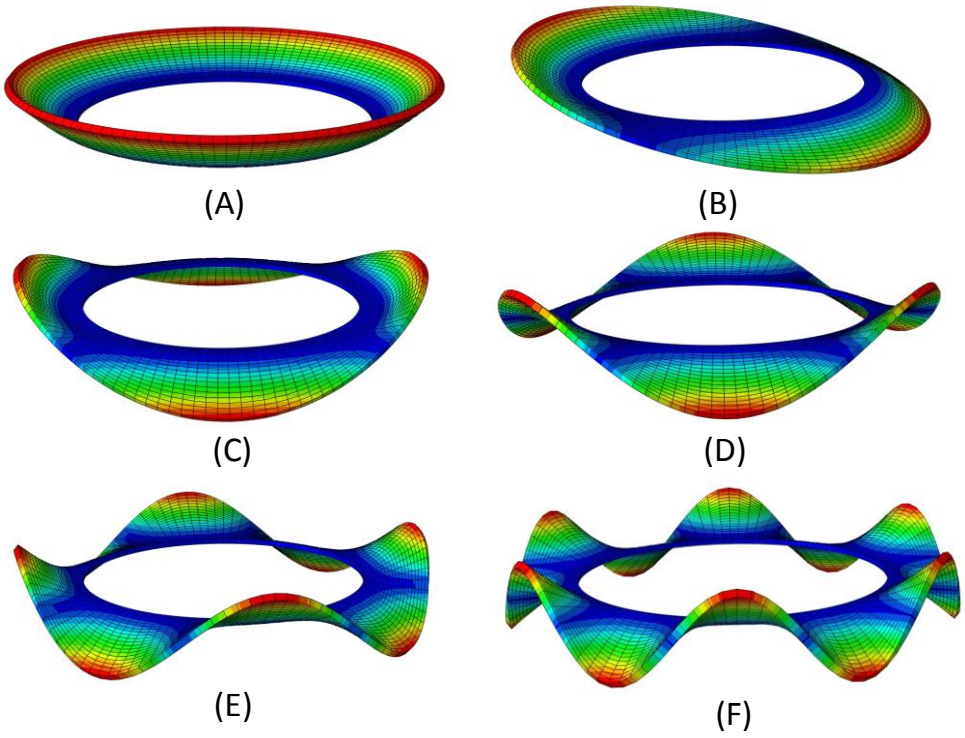

Figure 3.6: Dominant buckling modes for an annular ring with fixed inner radius, with both axisymmetric and non-axisymmetric modes included

The relationship between the critical buckling temperature and the circumferential displacement wave number is shown in Figure 3.7. From Figure 3.7, it is shows that the results of mode 1 to mode 14 obtained through the Fourier model and the results obtained through the ABAQUS model are very close. The critical buckling temperature of the coning mode is the lowest (absolute value) among the buckling modes with negative eigenvalues. In Figure 3.7, it also represents that the sign of the buckling eigenvalue transits from negative at n=2 to positive at n=3. Furthermore, in the region with positive buckling eigenvalues, the dominant buckling mode is Mode 6 (n=6 or Mode D).

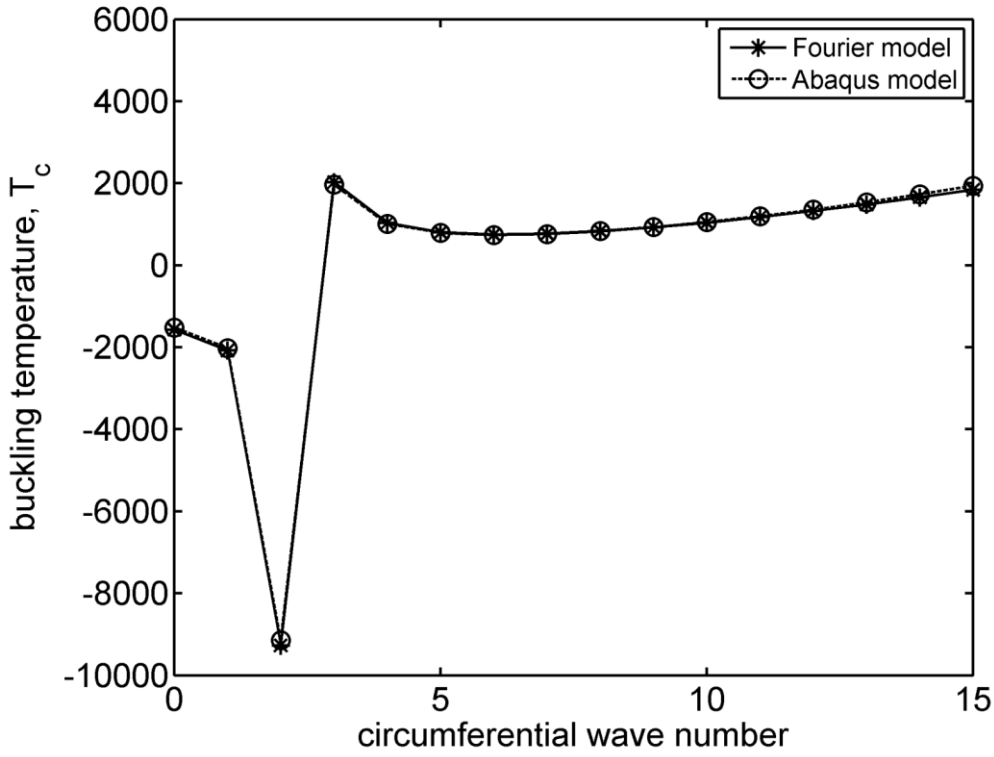

Figure 3.7: Buckling temperature as a function of circumferential wave number for an annular ring with fixed inner radius

The region with positive eigenvalues in Figure 3.7 is plotted in Figure 3.8. It shows that the critical buckling temperatures of Mode 5 thru Mode 9 are below 1000°C,

which is in the working temperature range of clutch systems. In practical applications, the teeth on the edge of the clutch disk and the splines in the shaft impose restrictions to the clutch plates, which affect the excited buckling modes and corresponding buckling temperatures. As the critical buckling temperatures of Mode 5 thru Mode 9 are close, the excited mode is determined by the boundary conditions.

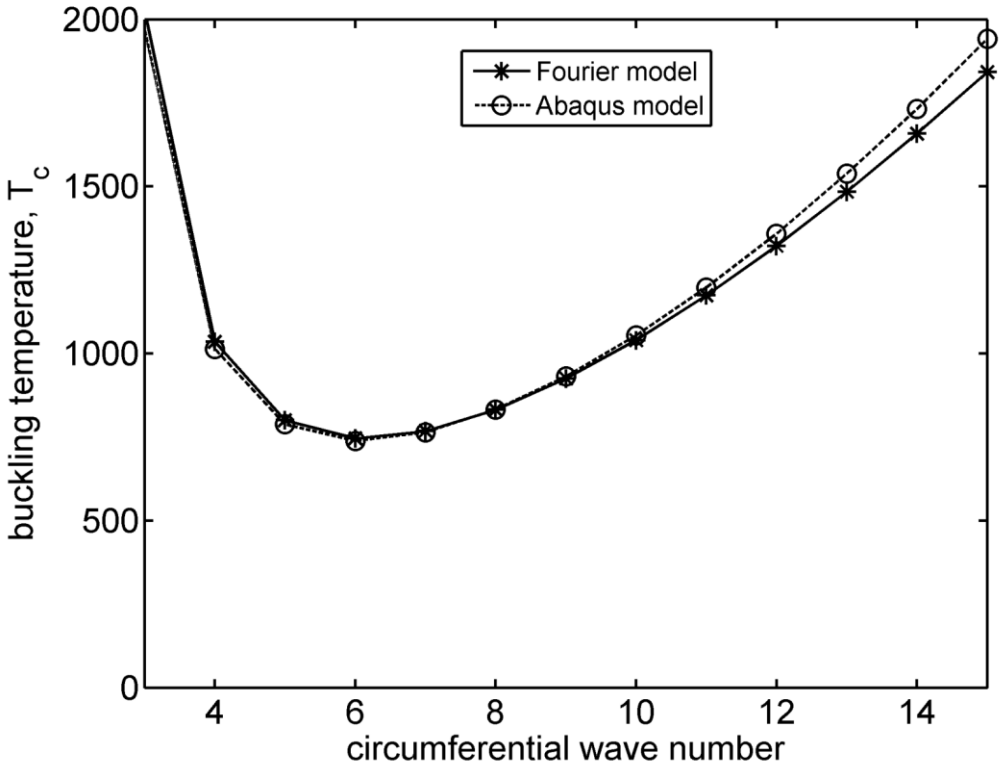

Figure 3.8: Enlarged figure showing the positive buckling temperature as a function of circumferential wave number

All aforementioned results in this subsection are obtained from the model with fixed inner radius. The critical buckling temperatures of certain modes are above the melting point of the material of the clutch disk, therefore, these modes do not exist in reality. When both the inner radius and outer radius are free, as the critical buckling

temperature of the axisymmetric mode is significantly lower than the value aforementioned [11], it is more likely the dominant mode. In practical applications, the real boundary condition of a disk is somewhere between fully fixed and completely free. Therefore, the buckling temperatures obtained from models with fixed and free boundaries should be considered as extreme values.

3.4 Conclusions

A Fourier finite element algorithm predicting the buckling deformation modes and the corresponding critical buckling temperatures in automotive brakes and clutches has been developed. In the current research, the thermal load is predefined as a function of radial coordinate, and the governing equation is derived based on the Green tensor. As the complexity of the configuration has been simplified, the computational efficiency has been increased significantly. The Fourier model was validated by comparing the calculated results with the counterparts obtained from a three-dimensional model developed in ABAQUS. Both axisymmetric and non-axisymmetric buckling modes have been evaluated. It is found that there is a dominant buckling mode with the lowest critical buckling temperature among all modes. The dominant buckling mode is determined by the material properties and geometric shapes. The critical buckling temperatures obtained from the models with free boundaries are lower than the buckling temperatures obtained from the models with constrained boundaries. In addition, the results of the current research imply that both thermal buckling and TEI exhibit similar mode patterns and that the two phenomena could be coupled together as the temperature gradient is sufficiently high. The achievements described in this section have been summarized in ref. [58].

4 A NUMERICAL ANALYSIS OF THE COUPLING BETWEEN FRICTIONALLY EXCITED THERMOELASTIC INSTABILITY AND THERMAL BUCKLING

4.1 Introduction

As mentioned previously, two failure mechanisms sheared by automotive clutch systems and brake systems are thermoelastic instability (TEI) and thermal buckling [21,32]. Normally, the contact pressure distributions in the interfaces between clutch disks can be considered as uniform. Meanwhile, there are pressure disturbances on the contacting surfaces. When the sliding speed of the system is higher than the *critical speed* of a frictional system, the thermal-mechanical feedback will become unstable [12,15]. Therefore, separated regions where the contact pressures and the temperatures are higher than surroundings exist. The localizations of the contact pressure and the temperature distribution were first discovered and explained by Barber [11].

Thermal buckling is another source of failures of automotive clutches and brakes. The principle of thermal buckling is when the thermal stress in the circumferential direction is high enough, the stability of a system will be lost [4]. To improve the performances of products suffered from high temperature, numerous studies have been performed on this problem. Thornton [59] and Taunchert [60] summarized achievements on this field. Najafizadeh and Hedayati evaluated the thermal buckling of an FGM ring through the first order shear deformation theory (FSDT) [61]. Based on higher order

deformation theory, Najafizadeh and Heydari obtained buckling temperatures for circular disks. They discovered that the buckling temperatures obtained by using first order shear deformation theory and classic plate theory are higher than that obtained by using higher order shear deformation theory [62].

The purpose of the current study is assessing the possibility of thermal buckling in the presence of temperature distributions induced by TEI. Formerly, the patterns of the thermal loads are based on reasonable hypotheses. Nevertheless, the temperature profiles induced by excited TEI modes are significantly different from the assumed temperature profiles previously. Meanwhile, the temperature profiles associated with TEI probably can cause thermal buckling. Thus, evaluating the coupling between these two phenomena is of practical and theoretical significance. The software *Hotspotter* will be applied to generate the temperature distributions induced by TEI. The CAE software ABAQUS will then be utilized to calculate the critical buckling temperatures and corresponding buckling modes. The effects of the frictional coefficient, the sliding speed and the TEI focal hot spots will be explored. As the pressure distributions and thus the temperature profiles can be altered by the thermal buckling, TEI is influenced by thermal buckling as well. But, in this chapter, only the effect of TEI towards thermal buckling is investigated.

4.2 Method

The current study is divided into two steps. The first step is to evaluate thermoelastic instability and to obtain temperature profiles by applying finite element analysis software *HOTSPOTTER*. The second step is investigating the thermal buckling to obtain the critical buckling temperatures and associated buckled configurations. In the

current study, the dimensions and material properties of a clutch disk that is from a practical application have been chosen.

HOTSPOTTER is FEA software investigating TEI phenomenon developed by Barber and Yi. There are two modules in this software, *classic* and *full three-D*. The classic module calculates critical speeds when the number of hotspots is defined. The full three-D module generates temperature distributions of certain TEI modes, if the sliding speed is defined [23].

As the temperature and the contact pressure grow exponentially with time, it is reasonable to express the temperature distribution, the nodal displacement field and the stress distribution as products of functions of spatial coordinates and terms increasing exponentially with time. For example, the temperature distribution can be written in the following form [21].

$$T(r,\theta,z,t) = \Re\left\{e^{bt+jn\theta}\Theta(r,z)\right\} \tag{4-1}$$

The governing equation of a body β is

$$K_\beta\left(\frac{\partial^2 T}{\partial r^2}+\frac{1}{r}\frac{\partial T}{\partial r}+\frac{1}{r^2}\frac{\partial^2 T}{\partial \theta^2}+\frac{\partial^2 T}{\partial z^2}\right)-\rho_\beta c_\beta\left(\frac{\partial T}{\partial t}+\omega_\beta\frac{\partial T}{\partial \theta}\right)=0 \tag{4-2}$$

where K, ρ, c and ω are the thermal conductivity, the density, the specific heat of a particular type of material and the angular velocity of an object respectively. Following equations define the eigenvalue problem of the growth rate *b* [21].

$$[(K+C+fV\Phi A)+bH]=0 \tag{4-3}$$

$$K=\iint_\Omega K_\beta\left(\frac{\partial W}{\partial r}\frac{\partial W^T}{\partial r}-\frac{W}{r}\frac{\partial W^T}{\partial r}+\frac{\partial W}{\partial z}\frac{\partial W^T}{\partial z}\right)d\Omega \tag{4-4}$$

$$H=\iint_\Omega \rho_\beta c_\beta W W^T\, d\Omega \tag{4-5}$$

$$C = \iint_{\Omega} \left(\frac{K_\beta n^2}{r^2} + jn\rho_\beta c_\beta \omega_\beta \right) WW^T d\Omega \quad (4\text{-}6)$$

In above equations, *K* represents the conductivity matrix, *H* represents the mass matrix and *W* is the matrix containing shape functions. The term of "$fV\Phi A$" is the nodal frictional heat generation. The matrix *A* is a general thermoelastic matrix. The Φ is the matrix relating the local heat flux produced in the contacted nodes to the heat flux at all nodes in the entire model. The relation can be written in the following form.

$$Q = \Phi Q_{con} \quad (4\text{-}7)$$

As a result, the growth rate at a sliding speed and the corresponding temperature distribution are determined by using the eigenvalue method.

The principle had been integrated into Hotspotter. In the current study, the Full 3-D module is applied to obtain the TEI temperature profiles. In the Full 3-D module, an FEA model is only able to be created through an input script file which is similar to that of an ABAQUS simulation model. Firstly, the elements and nodes on the cross section of a disk plate should be defined. The three-dimensional model is then created by rotating the cross section 360 degrees along the circumference. As long as the analysis is finished, a script file containing the eigenvectors or the temperature distributions of the TEI modes is produced. As the TEI mode with the highest growth rate bears the largest chance to be evoked, only the nodal temperatures of the TEI mode with the highest growth rate are needed in the buckling analysis.

In buckling problems, to take account the influence of the membrane stress, the stress stiffness matrix [k_σ] should be added to stiffness matrix [k] [50,51].

$$[k_\sigma] = \int [G]^T \begin{bmatrix} s & 0 & 0 \\ 0 & s & 0 \\ 0 & 0 & s \end{bmatrix} [G] dV \quad (4\text{-}8)$$

In above equation, *s* is defined as

$$s = \begin{bmatrix} \sigma_x & \tau_{xy} & \tau_{zx} \\ \tau_{xy} & \sigma_y & \tau_{yz} \\ \tau_{zx} & \tau_{yz} & \sigma_z \end{bmatrix} \quad (4\text{-}9)$$

Matix [G] consists of the differentiations of shape functions.

The reference stress stiffness matrix $[\mathrm{K}_\sigma]_{\mathrm{ref}}$ can be determined, when the structure is loaded by a reference load $\{\mathrm{R}\}_{\mathrm{ref}}$. As the load applied to the structure changes to $\{\mathrm{R}\} = \lambda\{\mathrm{R}\}_{\mathrm{ref}}$, the stress stiffness matrix will be $[\mathrm{K}_\sigma] = \lambda[\mathrm{K}_\sigma]_{\mathrm{ref}}$. Either the reference configuration of the structure or a buckled configuration of the structure can exist under the critical load. So, following two equations can be obtained.

$$\big([K] + \lambda_{cr}[K_\sigma]_{ref}\big)\{D\}_{ref} = \lambda_{cr}\{R\}_{ref} \quad (4\text{-}10)$$

$$\big([K] + \lambda_{cr}[K_\sigma]_{ref}\big)\big\{\{D\}_{ref} + \delta D\big\} = \lambda_{cr}\{R\}_{ref} \quad (4\text{-}11)$$

In equation 4-10 and equation 4-11, $\{\delta\mathrm{D}\}$ is the buckling displacement vector; λ_{cr} represents the critical buckling eigenvalue. Through subtracting the above equations, the governing equation of buckling eigenvalue can be derived.

$$\big([K] + \lambda_{cr}[K_\sigma]_{ref}\big)\{\delta D\} = \{0\} \quad (4\text{-}12)$$

In ABAQUS, both temperature distributions and mechanical loads are able to be defined as the reference loads [52]. The TEI modes and corresponding temperature distributions can be categorized into two types as shown in Figure 4.1. The first type of temperature distribution is called *banding mode* with an axisymmetric temperature profile. There are multiple annular regions on the surface of the disk in the banding mode

as shown in Figure 4.1 (a). The red circles represent areas with relatively high temperature, whereas, the temperature of the blue rings is lower. As shown in Figure 4.1 (b), the second type of temperature distribution is so-called *focal hotspots* of which there are several high-temperature regions and low-temperature regions around the circumference. In other words, the temperature distributions vary in both the radial and the circumferential directions. The *BUCKLE* step analyzing buckling can be set in the GUI of ABAQUS. It should be noticed that both mechanical and thermal loads can be applied as the reference loads, and critical buckling loads are represented as the products of the critical buckling eigenvalues and the reference loads. As the temperature profiles obtained in the TEI analyses are non-uniform, the reference loads are needed to be defined manually through the input files.

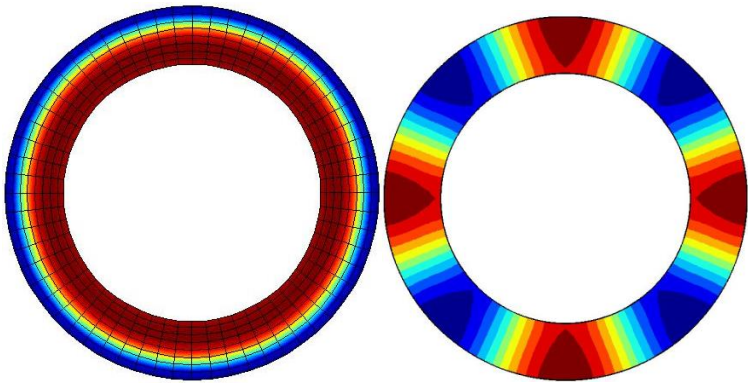

(a) (b)

Figure 4.1: Temperature distributions of TEI

It seems reasonable to develop FEA models by axisymmetric FEA elements to investigate the thermal buckling under banding modes, as the temperature distributions are axisymmetric. However, axisymmetric FEA models only work when both the reference loads and buckled configurations are axisymmetric [33]. In previous researches,

shell elements were applied to develop three-dimensional planar models, based on the fact that temperature does not change significantly in the thickness direction. Nonetheless, temperature variation in the thickness direction cannot be ignored in the presence of TEI phenomenon. Thus, FEA models evaluating thermal buckling in the current study must be constructed by three-dimensional solid elements.

4.3 Results

4.3.1 Convergence Test and Result Verification

Convergence tests must be performed to guarantee that FEA models yield correct results. The FEA models used in the current study should be convergent for thermoelastic instability analysis and thermal buckling analysis. The material properties and dimensions are tabulated into Table 4.1. The sketch of the model evaluating TEI is shown in Figure 4.2, there are two fixed frictional disks pressing a moving metal disk.

Metal disk	Inner radius	Outer radius	Thickness	Young's modulus	Poisson's ratio	Thermal expansion
Symbol	R_{a1}	D_{b2}	T_1	E_1	ν_1	α_1
Unit	mm	mm	mm	Gpa		10^{-6}/k
	86	125	3	160	0.29	12.7
Friction disk	Inner radius	Outer radius	Thickness	Young's modulus	Poisson's ratio	Thermal expansion
Symbol	R_{a2}	D_{b2}	T_2	E_2	ν_2	α_2
Unit	mm	mm	mm	Gpa		10^{-6}/k
	86	125	6	2.26	0.29	12.1

Table 4.1: Material properties and dimensions of the model

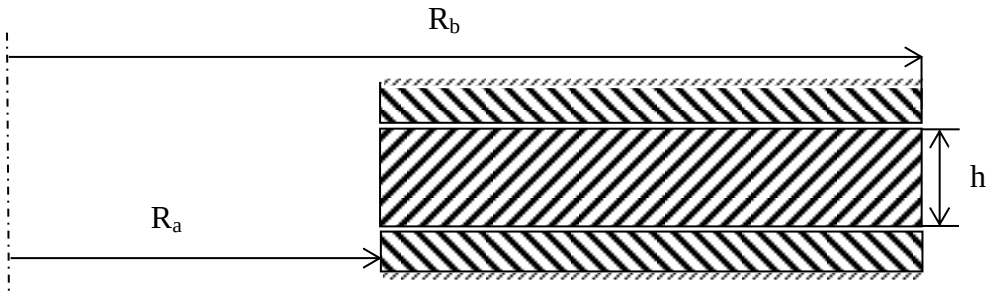

Figure 4.2: Schematic of the model

In TEI problems, there are two or more objects sliding against each other, linearly interpolated elements must be selected in this type of simulation. As a result, in models evaluating TEI phenomenon, C3D8 elements and 2DF elements are chosen. C3D8I elements are chosen for the thermal buckling analysis as incompatible elements are with better bending performance.

For TEI phenomenon, temperature changes obviously in the thickness direction, so there must be several elements in the thickness direction. Temperature gradients near the surfaces of friction disks are extremely sharp. Thus, the meshes of friction disks are biased toward the surfaces that are contacted by the metal disk. All the meshes are represented by the number of elements in the radial direction × the number of elements in the thickness direction × the number of elements in the circumferential direction. Three models with different mesh densities are developed, and the results of the convergence test are listed in Table 4.2. As the temperature distribution is not even, we chose the largest TEI growth rate as the sign of convergence. It shows that the difference between the finest mesh and the thickest mesh is about 2%. The first mesh and third mesh are shown in the Figure 4.3.

	Metal disk	Friction pad	Simulation time (s)	Largest growth rate	Error
1	8×4×60	8×15×60	4832.31	1.960	N/A
2	6×3×48	6×10×48	1237.35	1.962	1.02%
3	4×2×30	4×5×30	47.70	2.004	2.24%

Table 4.2: A comparison of the results using different meshes in TEI analysis

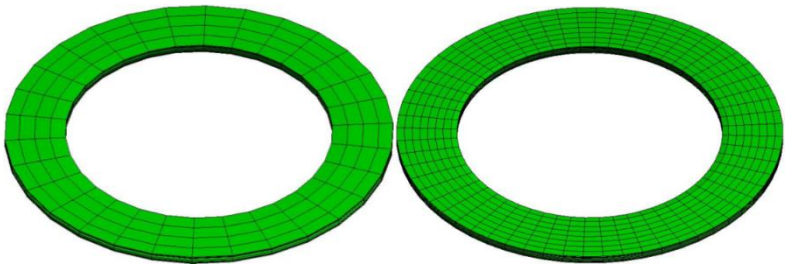

Figure 4.3: Graphic representations of the model

Next, convergence test of 2-D Fourier models investigating TEI is conducted. Three meshes listed in Table 4.3 are applied for the testing purpose. The different meshes are denoted by the products of element numbers along the radius and element numbers in the axial direction. The TEI growth rate of *banding mode* is picked as the sign of convergence. Through Table 4.3, we discover that the variance between the thinnest mesh and thickest mesh is around 2%. As the efficiency of the first model is low, the second mesh should be selected for the current research.

	Friction disk	Metal disk	Simulation time	Growth rate of mode 0	Error
1	33×24	33×9	5824.66s	1.587×10^{-4}	N/A
2	22×16	22×6	353.73s	1.600×10^{-4}	0.82%
3	11×8	11×3	11×3	1.636×10^{-4}	2.25%

Table 4.3: Convergence test of 2D meshes for investigating thermoelastic instability

The convergence test is also conducted on the model investigating thermal buckling of clutch disks. In the testing models, the reference thermal loads linearly increase from the inner radii of disks to the outer radii of disks. Both the inner radii and the outer radii of the testing models are without constraints. A new mesh (i.e. 16×8×120)

had been developed for the testing purpose. The results of the convergence test are tabulated in Table 4.4 from which we conclude that the first mesh is about to be chosen.

Mesh	Metal disk meshes	Buckling temperature	First buckling mode	Error
0	16×8×120	-177.45	coning	NA
1	8×4×60	-177.65	coning	0.11%
2	6×3×48	-178.11	coning	0.37%

Table 4.4: Convergence test of meshes for investigating thermal buckling

To prove that the results obtained from FEA analyses are accurate, we compare the calculated results with analytical solutions. The critical bending moment leading to buckling of an annular disk is expressed as Equation 4-13, on the basis of classic beam theory.

$$M = \int_{R_a}^{R_b} t\sigma_{\theta\theta}(r)(r - R)dr \tag{4-13}$$

If both the inner radius and the outer radius are not constrained, the variation of circumferential stress caused by temperature can be presented as Equation 4-14.

$$\begin{cases} \sigma_{\theta\theta}(r) = \frac{\alpha E}{r^2}\int_{R_a}^{r} rT(r)dr - \alpha ET(r) + \frac{EC_1}{1-\nu} + \frac{EC_1}{(1+\nu)r^2} \\ C_1 = \frac{\alpha}{2(1-\nu)}\frac{1}{R_b^2 - R_a^2}\int_{R_a}^{R_b} rT(r)dr \\ C_2 = \frac{\alpha(1+\nu)R_a^2}{R_b^2 - R_a^2}\int_{R_a}^{R_b} rT(r)dr \\ T(r) = \frac{\Delta T}{R_b - R_a}(r - R_a) \end{cases} \tag{4-14}$$

The comparison between the analytical solution and the numerical solution is shown in Table 4.5, from which we confirm that the finite element analysis yields correct results.

Mode	Analytical results	FEA results	Error
1	-173.83	-177.65	2.198%
2	213.85	212.83	0.4770%
3	429.42	426.44	0.6939%
4	645.42	644.20	0.1890%
5	861.60	870.46	1.028%

Table 4.5: Verification of the model for investigating thermal buckling

4.3.2 Effects of Boundary Conditions

A TEI analysis is performed through a model in which the sliding speed of the metal disk is 10 m/s. 10 m/s is equivalent to 97.79 rad/s or 933.83 rpm. In the rest of the current chapter, this model is used as the reference model.

The temperature distribution (i.e. TEI eigenvector) of the dominant TEI mdoe is the most important one, as it bears a large chance to be evoked. In the current study, the simulated temperature distributions are normalized TEI eigenvectors representing the evoked disturbances. In other words, the product of a constant and a TEI eigenvector is also a TEI eigenvector. For the reference model, the peak value of the evoked eigenvector is 2.150×10^{-2} ℃. The dominant TEI mode of the reference model is presented in Figure 4.4. Through Figure 4.4, we found that the temperature around the inner radius is higher than the temperature around the outer radius.

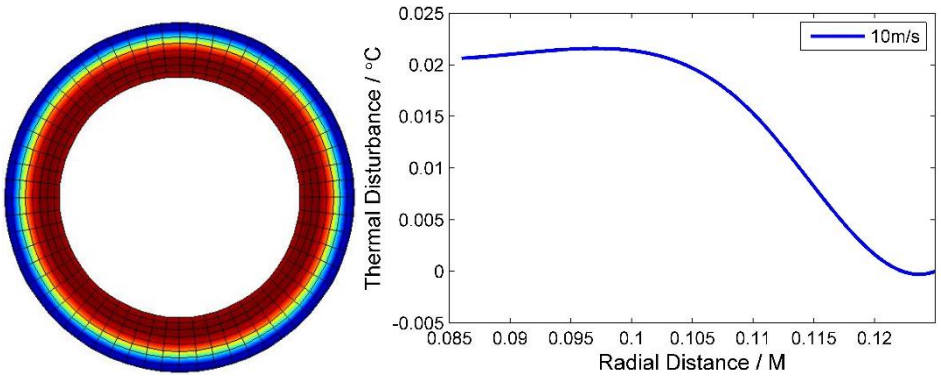

Figure 4.4: Temperature distribution (normalized) with sliding speed of 10 m/s

Multiple models have been developed to study the effects of different boundary conditions. In this research, we define the critical buckling temperature as the product of the peak value of the reference thermal load and the calculated critical buckling eigenvalue. When the inner radius of the model is fully clamped, the buckling mode is the 8^{th} order wavy mode. At this situation, the critical buckling eigenvalue is 1.54×10^{5}. According to the definition of critical buckling temperature, the critical buckling temperature is equal to 3.32×10^{3} ℃. The dominant buckling mode is the 5^{th} order wavy mode, when the disk is movable in the axial direction. The associated buckling eigenvalue and critical buckling temperature are 8.90×10^{4} and 1913.57 ℃ respectively. The dominant buckling mode is the 2^{nd} order wavy mode, when the disk is movable in both the axial direction and the radial direction. The associated buckling eigenvalue and critical buckling temperature are 2.99×10^{4} and 643.84 ℃ respectively. The buckled configurations of the three different boundary conditions are presented in Figure 4.5 in which different colors in are applied to denote the values of displacement in the axial direction.

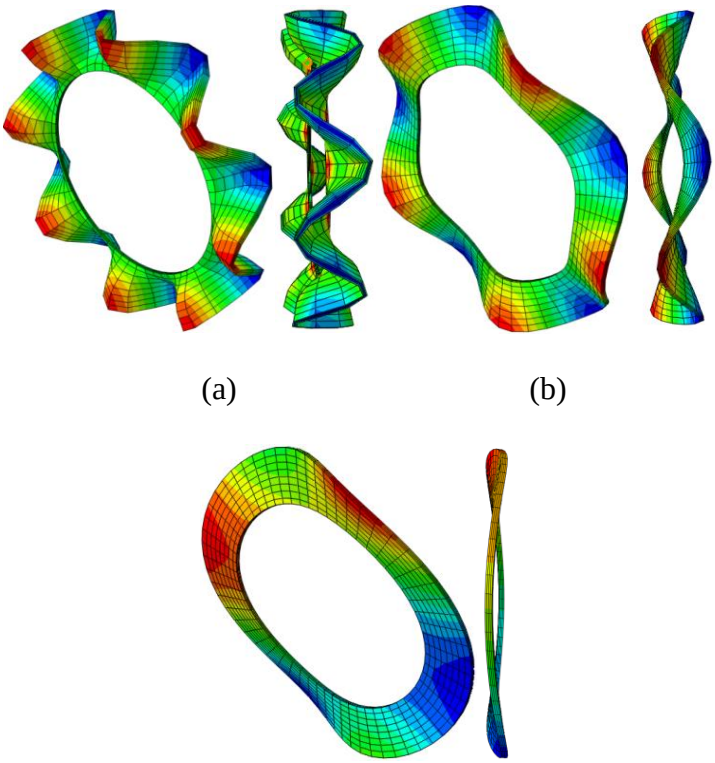

(a) (b)

(c)

Figure 4.5: Buckling modes with the sliding speed of 10 m/s at different boundary conditions

If the inner radius is totally free, the dominant buckling mode is a coning mode. The associated buckling eigenvalue and critical buckling temperature are 9314 and 200.25 ℃ respectively. Under this circumference, the critical buckling temperature is much lower than working temperatures of clutch systems, which shows that the temperature profiles caused by TEI probably can lead to thermal buckling of clutch disks. However, in order to prevent the rigid body motions, in the rest of this chapter the inner radii of all models are fixed in the circumferential direction.

4.3.3 Effects of Coefficient of Friction

The influence of the frictional coefficient on TEI and thermal buckling has also been investigated. Multiple models evaluating TEI phenomenon in which the frictional coefficients are equal to 0.26, 0.39, 0.52 and 0.65 have also been created. These values are constant multiples of the original coefficient of friction 0.13. In the new models, the other material properties and the sliding speed remain. The temperature distributions along the radius of the disk obtained from the TEI models are plotted in Figure 4.6.

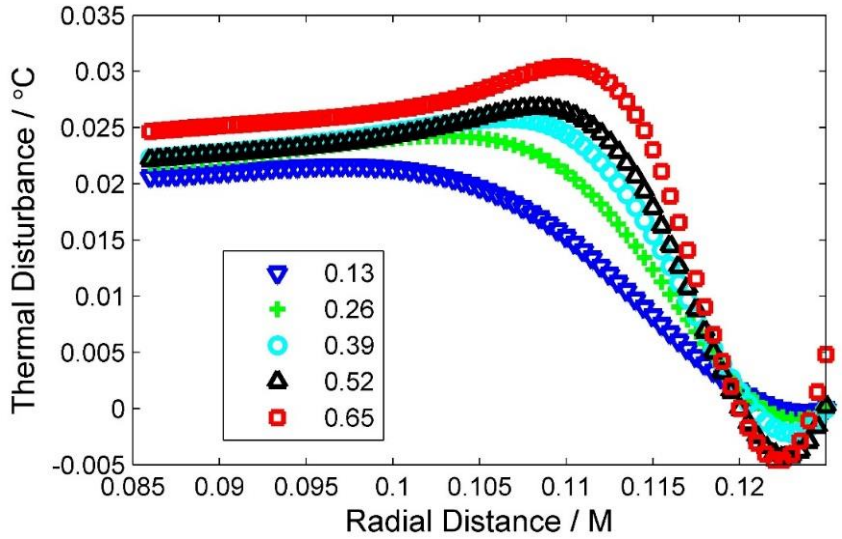

Figure 4.6: Temperature variations with different coefficients of friction

Through Figure 4.6, we discover that the value of frictional coefficient does not change the temperature profiles along the radial direction (i.e. TEI mode) considerably. It also shows that the difference between maximum temperature and minimum temperature becomes larger as the rise of the frictional coefficient. As mentioned in the previous section, the inner radii of all models are constrained in the circumferential direction. Multiple finite element analyses evaluating the thermal buckling have been performed, and the critical buckling eigenvalues of 2.99×10^4, 3.09×10^4, 3.26×10^4, 3.47×10^4 and

3.56×10^4 have been obtained. According to the definition of critical buckling temperature, the associated critical buckling temperatures of these models are 643.84 ℃, 743.85 ℃, 838.93 ℃, 915.45 ℃ and 1054.15 ℃. Through the calculated results, it can be concluded that both the critical buckling eigenvalue and the critical buckling temperature grow with the rise of the value of the frictional coefficient. The buckled configurations gained from aforementioned models are alike with that presented in Figure 4.5(c).

4.3.4 Effects of Relative Sliding Speed

The influence of the sliding speed of the metal disk on TEI and thermal buckling has also been investigated. Multiple models evaluating TEI phenomenon in which the sliding speeds of the metal disks are equal to 20 m/s, 30 m/s, 40 m/s and 50 m/s have also been created.

If the sliding speeds are at 10 m/s, 30 m/s and 50 m/s, the temperature around the inner radius is higher than the temperature around the outer radius of the clutch disk. The temperature profiles along the radius of the clutch disk are presented in Figure 4.7.

Through Figure 4.7, we discover that the difference between maximum temperature and minimum temperature becomes larger as the rise of the sliding speed. As mentioned in the previous section, the inner radii of all models are constrained in the circumferential direction. Multiple finite element analyses evaluating the thermal buckling have been performed, and the critical buckling eigenvalues of 2.99×10^4, 3.26×10^4 and 3.56×10^4 have been obtained. According to the definition of critical buckling temperature, the associated critical buckling temperatures of these models are 643.84 ℃, 838.93 ℃ and 1083.06 ℃. Through the calculated results, it can be concluded

that both the critical buckling eigenvalue and the critical buckling temperature grow with the rise of the value of the sliding speed.

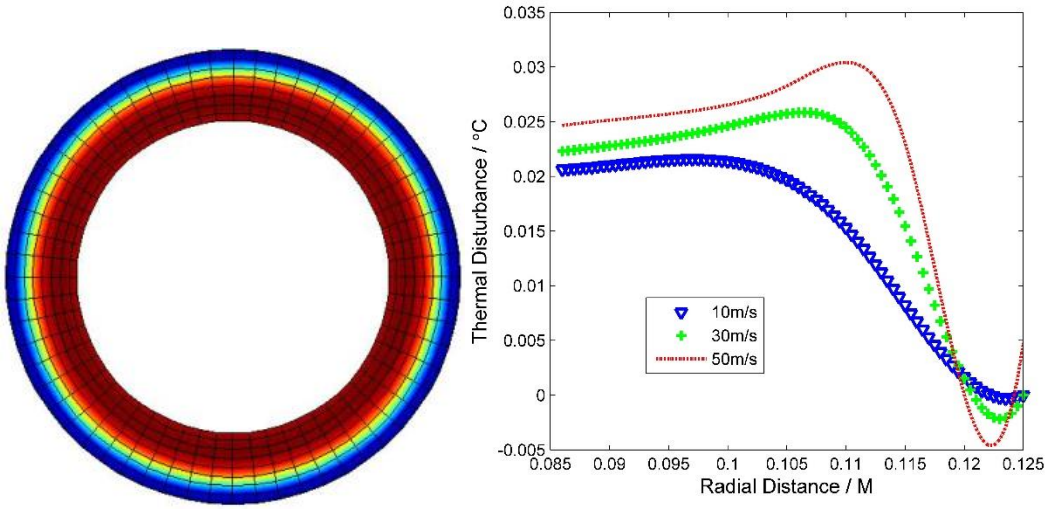

Figure 4.7: Temperature variations with sliding speeds of 10, 30 and 50 m/s

If the sliding speeds are at 20 m/s and 40 m/s, the temperature around the inner radius is lower than the temperature around the outer radius of the clutch disk. The temperature profiles along the radius of the clutch disk are presented in Figure 4.8.

Through Figure 4.8, we discover that the difference between maximum temperature and minimum temperature becomes larger as the rise of the sliding speed. As mentioned in the previous section, the inner radii of all models are constrained in the circumferential direction. Multiple finite element analyses evaluating the thermal buckling have been performed, and the critical buckling eigenvalues of 2.48×10^4 and 2.83×10^4 have been obtained. According to the definition of critical buckling temperature, the associated critical buckling temperatures of these models are 597.04 ℃ and 746.51 ℃. Through the calculated results, it can be concluded that both the critical

buckling eigenvalue and the critical buckling temperature grow with the rise of the value of the sliding speed.

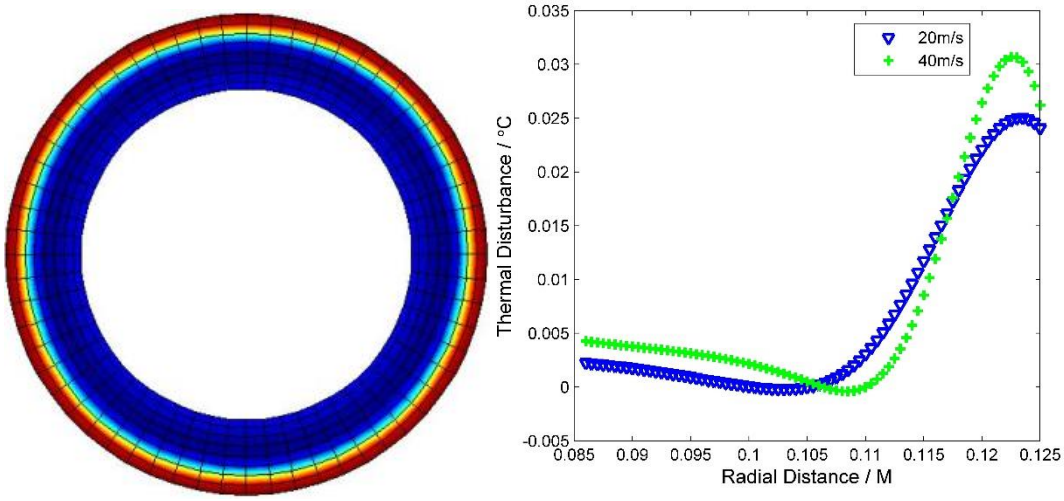

Figure 4.8: Temperature variations with sliding speeds of 20 and 40 m/s

4.3.5 Effects of Focal Hot Spots

The possibility of thermal buckling under the circumstances when there are hotspots on the surface of the metal disk is also investigated. The thermoelastic instability critical speeds as well as the corresponding temperature distributions on a cross-section of the clutch have been studied by using models developed by using two-dimensional Fourier elements. Then the temperature distributions in three-dimensional Cartesian coordinate can be restored numerically. The temperature distributions are shown in Figure 4.9. There are 2, 4 and 6 focal hotspots on the surface of the metal disk. The critical buckling eigenvalues are 2.32×10^4, $2.75\times10^4$and 2.28×10^4. The associated critical buckling temperatures are 1584.08 ℃, 1986.37 ℃ and 1818.70 ℃ respectively. These calculated critical buckling temperatures are only with theoretical importance, as they are well above working temperatures of clutch systems.

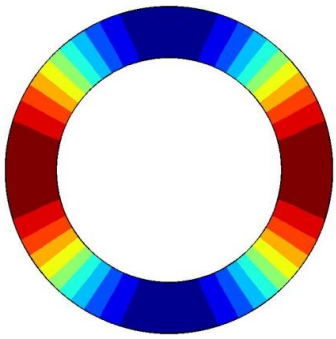

Mode 2

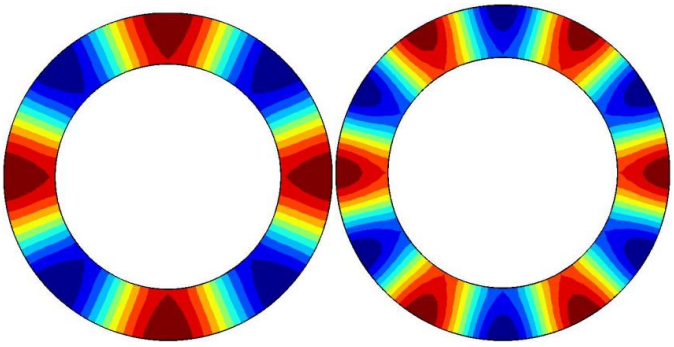

Mode 4 Mode 6

Figure 4.9: Hot spots on the surface of metal disk

4.4 Conclusion

This study aims at investigating the effects of temperature distributions produced by thermoelastic instability upon thermal buckling of automotive clutch disks. The temperature distributions involved in the current research are obtained from the finite element analyses of thermoelastic instability. Through using these temperature distributions, critical buckling temperatures and buckling modes have been studied numerically. When sliding speeds change from 10 m/s to 50 m/s, the critical buckling temperatures increase from around 650 ℃ to 1100 ℃. And when coefficients of friction switch from 0.13 to 0.65, the critical buckling temperatures rise from around 650 ℃ to 1050 ℃. If the TEI modes are banding, there is a circle with low temperature and also a

circle with high temperature. When the inner circle is with high temperature, critical buckling temperature is greater than when the outer radius is high-temperature zone. Under the situations when hot spots exist, the buckling critical temperatures are well above the working temperatures of actual applications. The achievements described in this section have been summarized in ref. [63].

5 FINITE ELEMENT MODELS PREDICTING POSTBUCKLING OF CLUTCH DISKS

5.1 Introduction

The behavior of a structure after it buckles is named as "postbuckling". The dominant buckling mode of a clutch plate can be axisymmetric or non-axisymmetric [26,30]. The conventional buckling finite element analysis or *linear* finite element buckling analysis can only calculate the dominant buckling mode and associated buckling load of a structure under a particular type of load. The postbuckling or *nonlinear* buckling analysis is also able to evaluate the stress distribution and displacement field at a particular loading condition [64].

Due to its importance in industrial applications, the extensive linear thermal buckling analyses of clutch disks have been reported in the literature. However, researches related to thermal postbuckling are still lacking. Ma [34] and Li [35] investigated thermal postbuckling of FGM (functionally graded material) circular plate by aaplying von Karman's plate theory. Sepahi et al. inspected the axisymmetric postbuckling of an annular plate which is fixed in both inner and outer radii by using the first order shear deformation theory (FSDT) [36]. To the author's knowledge, thermal postbuckling of circular disks and annular plates related to clutch applications has not yet investigated systematically. One obvious deficiency in the existing results is that the boundary conditions were not well represented. In real applications only the inner radius

or the outer radius of a clutch disk is constrained, but not both. Multiple researchers pointed out that the boundary condition affects both the excited buckling modes and the associated critical temperatures [32]. It is necessary to evaluate the thermal postbuckling behavior of an annular plate when only its inner radius or outer radius is fixed. The second motivation to perform this analysis is that the previous works such as those in refs. [34,35 and 36] focused on the axisymmetric modes alone. However, the non-axisymmetric modes can be dominant in some situations. Therefore evaluating the axisymmetric modes alone is inadequate [65].

5.2 Method

5.2.1 Principle of Nonlinear Buckling Analysis

The current study consists of two steps. The first step is to perform linear buckling analyses to obtain the dominant buckling modes and the corresponding critical buckling temperatures. The deformation fields of the dominant buckling modes extracted from the first step are used as the initial perturbations in the second phase. Nonlinear buckling analyses are performed conducted in the second step to investigate the postbuckling behaviors of the clutch plate.

The linear buckling analysis can be performed by using the commercial CAE software ABAQUS. The geometric representation, material properties, boundary condition and reference load, can be defined in the GUI program of ABAQUS as discussed in the previous chapters. The "*BUCKLE*" analysis step is capable of computing the critical buckling eigenvalues and corresponding buckling modes. The governing equation of buckling of an individual structure is

$$\left([K] + \lambda_{cr}[K_\sigma]_{ref}\right)\{\delta D\} = \{0\} \quad (5\text{-}1)$$

where $[K_\sigma]_{ref}$ represents the stress stiffness matrix induced by the reference load, λ_{cr} is the critical buckling eigenvalue, and $\{\delta D\}$ is the buckling displacement field [50,51]. In comparison with the radial dimension, the thickness of a clutch disk is negligible; therefore, the 8-node shell elements with reduced integration can be applied. The FEA model and its corresponding mesh are shown in Fig. 5.1.

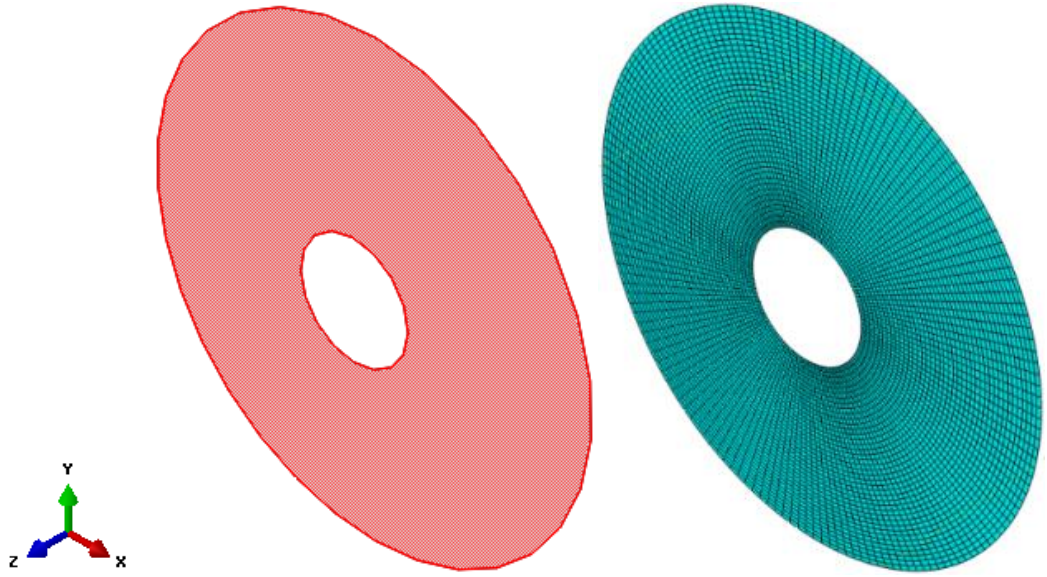

Figure 5.1: FEA model and its corresponding mesh

It is necessary to mention that the results of the linear buckling analyses in ABAQUS are critical eigenvalues, and the critical buckling loads are the products of the critical buckling eigenvalues and the reference loads. For an annular disk, all buckling modes can be classified into two types: *coning* modes and *wavy* modes. The coning mode is an out-of-plane mode that is axisymmetric, and the wavy mode has multiple reversals in the circumferential direction [32,58]. To extract the displacement field of the dominant

buckling mode, ABAQUS keyword "*NODE FILE*" should be added to the input script file manually, as this function is not available in the GUI of ABAQUS.

The linear buckling analysis in ABAQUS is indeed a type of eigenvalue algorithm; it is only capable of determining the stability boundary of a structure. If the load-displacement response is concerned, a nonlinear buckling analysis must be conducted. The governing equation defining the nonlinear buckling problem of a structure is

$$([K] + [K_\sigma] + [K_L])d\{\delta D\} = d\{P\} \quad (5\text{-}2)$$

where the $[K_L]$ is caused by a large displacement and is called as *initial displacement matrix*, $d\{P\}$ and $d\{\delta D\}$ represent the incremental load and the incremental displacement respectively [66].

The "*RIKS*" analysis step in ABAQUS can be adopted to simulate the postbuckling behavior of a clutch plate. This method has been widely used to analyze postbuckling behaviors of various structures [67,68]. The nonlinear buckling model can be modified from the linear buckling FEA model by replacing the "*BUCKLE*" analysis step by a "*RIKS*" analysis step. It should be noticed that the load defined in the nonlinear buckling model should be the *critical buckling load* (i.e. the product of the critical eigenvalue and the reference load) obtained from the linear buckling analysis rather than the *reference load* defined in the linear buckling analysis. To superpose the scaled buckling mode obtained from the linear buckling analysis to the original geometry of clutch plate to generate a perturbed mesh, the keyword "*IMPERFECTION*" should be added manually to the ABAQUS input file. As the maximum nodal displacement of the

displacement field obtained from the linear buckling analysis is normalized to 1 mm in ABAQUS, the displacement field should be multiplied by a scaling factor. The effect of the scaling factor will be discussed in the following subsection. Two lines from the input script file of a nonlinear buckling analysis are quoted here.

*IMPERFECTION,FILE=buckle,STEP=1

1,2e-3

The first line represents that the result of the 1^{st} analysis step of job *buckle* is the resource of initial imperfection. The second line represents that the nodal displacements of the 1^{st} buckling mode have been added to the original geometry to generate the perturbed mesh, and the maximum value of initial perturbation is 2×10^{-3} *mm*.

5.2.2 Method of Verification

The convergence test and result verification of linear buckling models have been elaborated in multiple articles [58,63] and the previous chapters as well. Hence, we present the verification of nonlinear buckling model in this subsection. For this purpose, the calculated results obtained by using the method described in the previous subsection are compared with the results presented in ref. [36]. The geometric representation in the ref. [36] is an annular plate, and its inner radius and outer radius are pinned. The material properties are temperature-independent. The geometric dimensions and material properties in the ref. [36] are listed Table 5.1.

Inner radius r_a	Outer radius r_b	Thickness	Young's modules	Poisson's ratio	Expansion coefficient
25 mm	100 mm	2 mm	348GPa	0.24	5.8723×10^{-6} K^{-1}

Table 5.1: Geometric dimensions and material properties of verification model

The temperature distribution in the ref. [36] is governed by one-dimensional steady-state conduction equation:

$$\frac{d}{dr}\left(r\frac{dy}{dx}\right) = 0 \tag{5-3}$$

As a result, the temperature distribution along the radial direction is

$$\begin{cases} T(r) = T_a - \Delta T \dfrac{ln(\frac{r}{r_b})}{ln(r_b/r_a)} \\ \Delta T = T_a - T_b \end{cases} \tag{5-4}$$

where the temperature at the inner radius (T_a) is fixed at 26.85 ℃, and the temperature at the outer radius (T_b) is increasing [69]. According to ref. [36], the part buckles when the temperature at the outer radius is 138.332 ℃. Therefore, the thermal load in the linear buckling analysis is set to

$$T(r) = 26.85 + 111.472\frac{ln(\frac{r}{100})}{ln\,4} \tag{5-5}$$

The calculated eigenvalue obtained from the model constructed by S8R elements is 0.9325, which implies that the difference is around 6.75%. Consider that the result in ref. [36] is obtained through a two-dimensional analytical model, this difference is acceptable. The dominant buckling mode is an axisymmetric mode which is shown in Fig. 5.2.

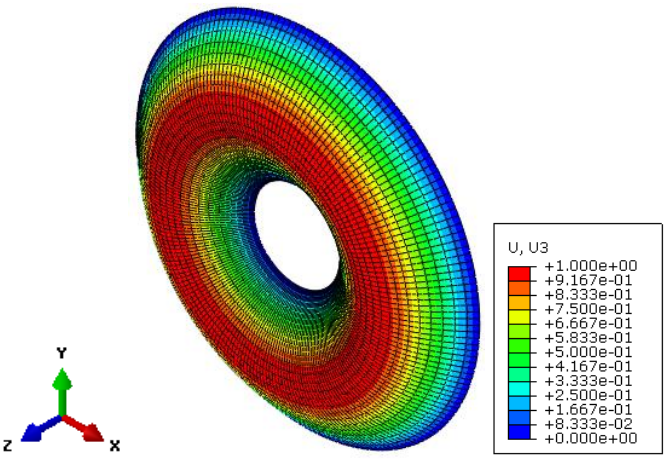

Figure 5.2: The dominant mode of testing model

As mentioned previously, the scaled displacement field should be added to the original geometry as an initial perturbation. A small scaling factor is preferred, as an excessive perturbation changes the geometry of the problem, and hence the results can be inaccurate. However, if the scaling factor is smaller than a critical value, the numerical difficulties will cause a divergence in the results. The load history diagram of the model in which 0.1% perturbation (i.e. the largest value of the perturbation is equal to 0.1% of the thickness of the plate) is added to the original configuration along with the load history diagram of the model in which 1 % perturbation is added to the original configuration, are plotted in Fig. 5.3.

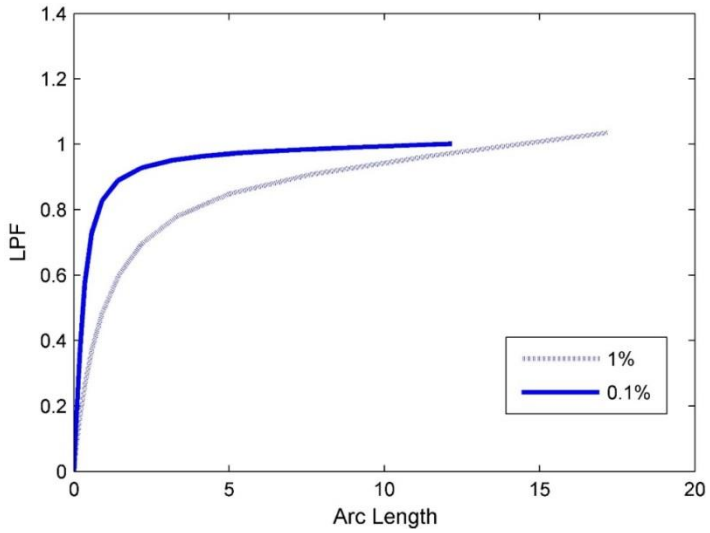

Figure 5.3: Load history diagrams obtained from models with different perturbations

The horizontal axis in the above figure is the arc length, which represents the increment in the computation. The vertical axis of the above figure is the Load Proportionality Factor (LPF). A unit value of the vertical axis denotes that 100% of the defined load has been applied to the structure. Through this figure, we can conclude that the calculated buckling temperature obtained from the model with 0.1% perturbation is about 95% of the value obtained from the linear buckling analysis, and an excessive perturbation (1%) can reduce the simulated critical buckling temperature significantly. Theoretically, as the scaling factor decreases, the load history curve will become to a "Γ" shape. However, we found that when the perturbation is less than 0.1% (2×10^{-3} mm), the results stopped to converge.

The dimensionless displacement in the axial direction at the medium radius ($r_m = (r_a + r_b)/2$) corresponding to the multiple temperature differences computed through the numerical method and the results obtained in ref. [36] are compared in Figure 5.4 and

Table 5.2. It shows that the average error is around 5.67%, which is satisfactory for the current study.

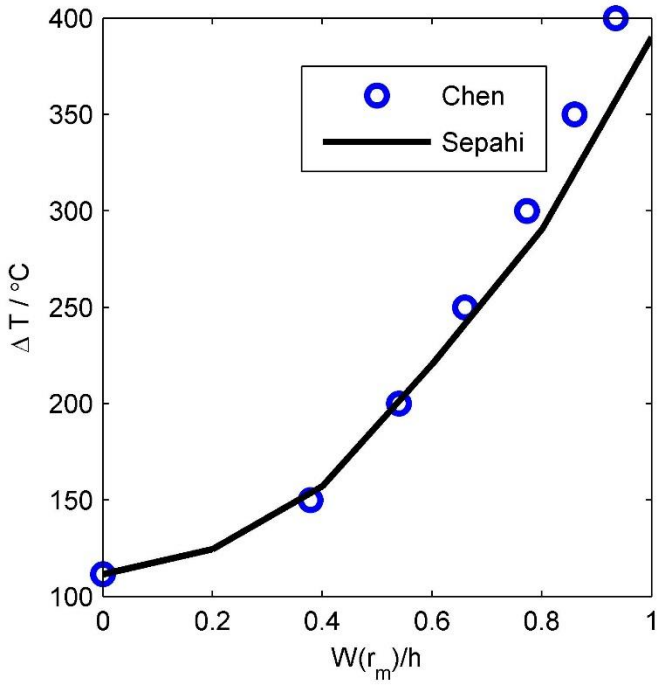

Figure 5.4: Verification results

ΔT	150	200	250	300	350	400
Sepahi	0.370	0.520	0.710	0.820	0.921	1.020
Chen	0.379	0.540	0.660	0.773	0.860	0.935

Table 5.2: Comparison between simulated and analytical results

5.3 Results

5.3.1 Linear Buckling Analysis

Multiple models of two different geometric parameters are developed in the current research. In each model, either the outer radius or the inner radius is constrained. It is assumed that these two types of disks are made of the same material, and the material properties and geometric dimensions are listed in Table 5.3.

Disk 1	Inner radius	Outer radius	Thickness	Young's modulus	Poisson's ratio	Thermal expansion
Symbol	R_{a1}	R_{b1}	h_1	E_1	ν_1	α_1
Unit	mm	mm	mm	Gpa	N/A	10^{-6}/k
	86	125	2.25	160	0.29	12.7
Disk 2	Inner radius	Outer radius	Thickness	Young's modulus	Poisson's ratio	Thermal expansion
Symbol	R_{a2}	R_{b2}	h_2	E_2	ν_2	α_2
Unit	mm	mm	mm	Gpa	N/A	10^{-6}/k
	44.5	57	3.25	160	0.29	12.7

Table 5.3: Material properties and dimensions of the models

In the current analysis, the thermal loads are assumed as linearly increasing from the inner radius to the outer radius of the annular plate, which is based on the fact that frictional heat generation is proportional to the relative sliding speed. The thermal loads can be represented by the following equation.

$$\begin{cases} T(r) = \Delta T \frac{r - r_a}{r_b - r_a} \\ \Delta T = T_b - T_a \end{cases} \quad (5\text{-}6)$$

In the linear buckling analysis, i.e. the first step, ΔT is set as 1 ℃, therefore the critical buckling temperature is equal to the calculated buckling eigenvalue. It should be mentioned that in a linear buckling FEA analysis the critical buckling load is the product of the applied mechanical or thermal reference load and the calculated critical buckling eigenvalue. The calculated critical buckling temperatures are tabulated into Table 5.4. In the current study, the boundary conditions are presented in a simplified way in Table 5.4, SF represents that the inner radius is simply supported and the outer radius is free, and in the FC boundary condition the inner radius is free and the outer radius is clamped.

BC / Result ℃	SF	CF	FS	FC
Disk 1	-31.0	420.8	31.1	749.0
Disk 2	-381.3	6819.3	475.0	14165

Table 5.4: The results of linear buckling analysis

Through Table 5.4, it can be concluded that models of the Disk 1 with the CF and FC boundary conditions and the model of the Disk 2 with the FS condition are of practical importance, as the operating temperatures of clutch systems are usually well below 1000 ℃ and should be positive. Hereafter, these three models are called as Model 1, 2 and 3. The dominant buckling modes of Model 1 and Mode 2 are wavy modes, and the dominant buckling mode of Model 3 is a coning mode. These models are selected in the current research to investigate postbuckling behaviors. The dominant buckling modes of the three models are plotted in Fig. 5.5, in which red represents large displacements in the axial direction and blue zones are with small displacements in the axial direction. It shows that the dominant mode of model 1 is a sixth-order wavy mode (i.e. there are 6 zones with large displacement), the dominant mode of model 2 is a fourth-order wavy mode, and the dominant mode of model 3 is a coning mode.

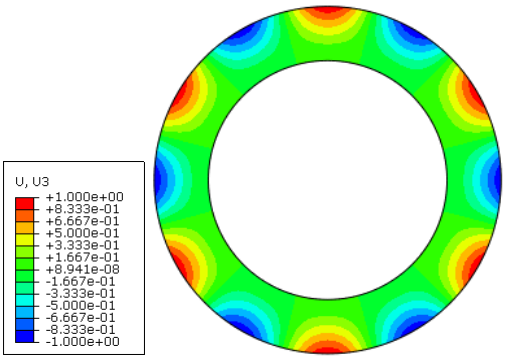

Mode 1

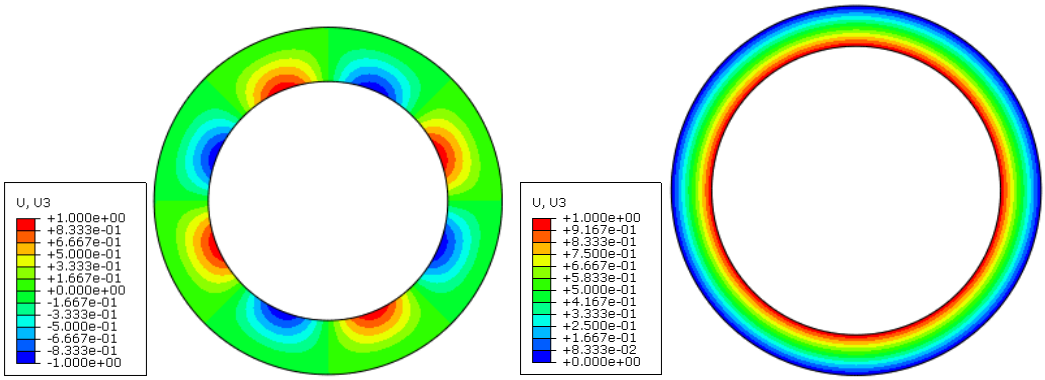

Model 2 Model 3

Figure 5.5: Dominant buckling modes

5.3.2 Postbuckling Analysis

To perform a postbuckling analysis of a structure, the scaled displacement field obtained from a linear buckling analysis has been introduced to the original geometry as an initial perturbation. The value of the scaling factor should be tested carefully, as an excessive perturbation can change the original geometry and hence the simulated results. The scaling factor can be determined through the load history diagrams. The load history diagrams of model 1, model 2 and model 3 with 0.1% and 1% initial perturbations are plotted in Fig. 5.6.

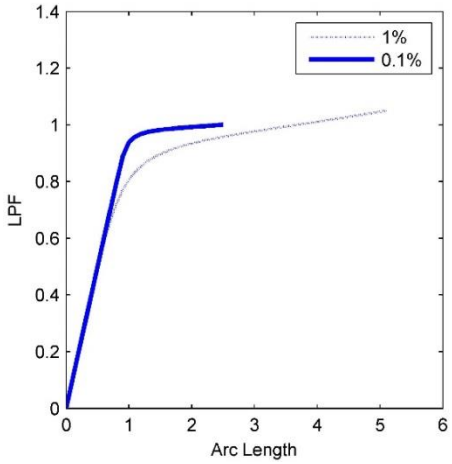

Model 1

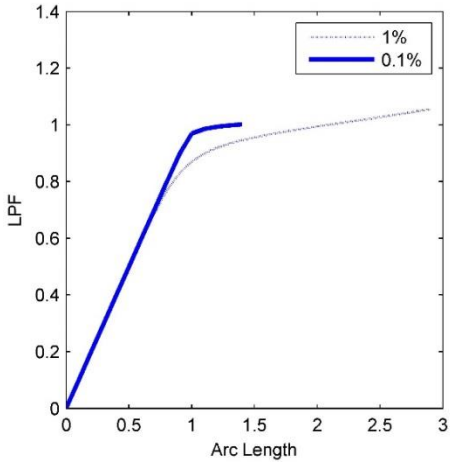

Model 2

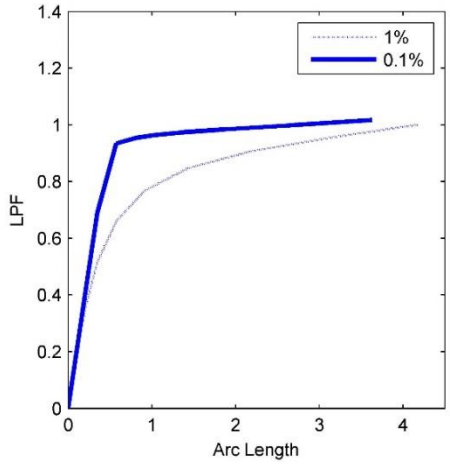

Model 3

Figure 5.6: Load history diagrams with different initial perturbations

If the material properties are temperature-independent, the knees of the load history diagrams should be close to 1s on the vertical axes which correspond to the critical buckling temperatures obtained from linear buckling analyses. Through Fig. 5.6, it can be found that the knees of load history diagrams of models with 0.1% perturbations are close to 1s. The slight differences are caused by the geometric nonlinearity and

numerical errors. However, there are no obvious knees in the load history diagrams of models in which the perturbations are 1% of the disk thicknesses, which reveals that the results are less accurate. In the current study, all perturbations applied to models are equal to 0.1% of the disk thicknesses.

The displacement profile in the axial direction along the outer radius of model 1 and the displacement profile in the axial direction along the inner radius of model 2 at the two different temperatures: (1) the critical temperatures and (2) 100 ℃ above the critical temperatures are plotted in Fig. 5.7. In the figure, we realize that at the critical buckling temperature the largest displacement in the axial direction along the outer radius of model 1 is around 0.3mm, and the largest displacement along the outer radius at 521 ℃ (100℃ above the critical temperature) is around 1.6 mm. It is also found that at the critical buckling temperature the largest displacement in the axial direction of model 2 is around 0.2mm, and the largest displacement along the inner radius at 850 ℃ (100℃ above the critical temperature) is around 2 mm. The largest displacements in the axial direction of model 1 are compared to the result of model 2 at 800 ℃. It is found that at 800 ℃, the largest displacement in the axial direction of model 1 is around 2.4 mm, and the largest displacement in the axial direction of model 2 is around 1.8 mm. Hence, fixing an annular disk at outer radius is a preferred method in practice, due to its higher critical temperature and smaller deformation.

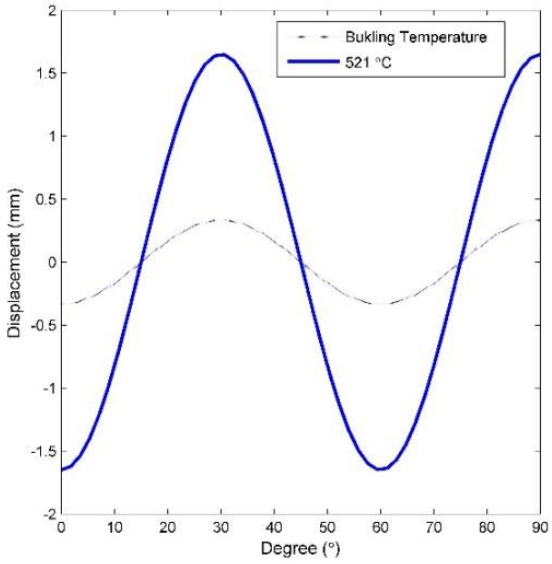

Mode 1

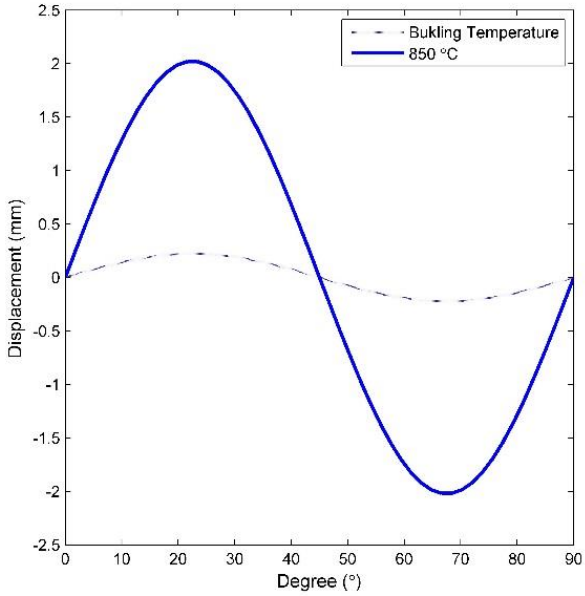

Model 2

Figure 5.7: The displacement in axial direction at the outer radius of model 1 and the displacement in axial direction at the inner radius of model 2

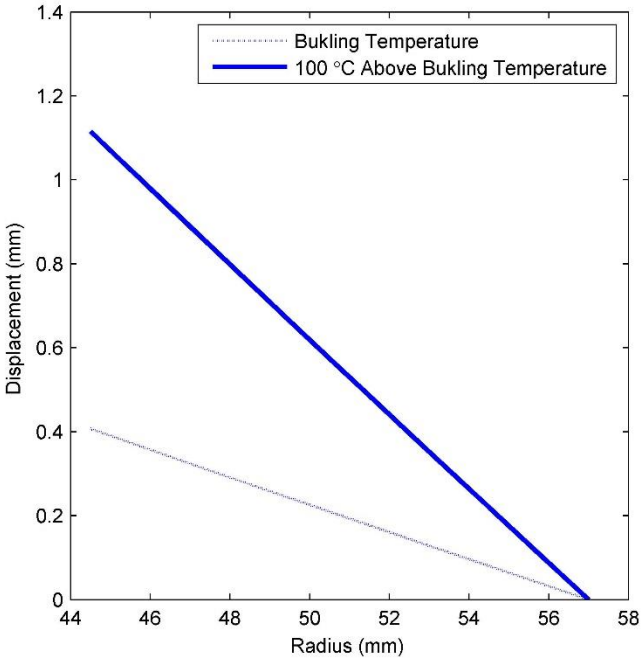

Figure 5.8: The displacement in the axial direction along the radius of model 3

The displacement distributions in the axial direction along the radius of model 3 at the critical temperature and 100 ℃ above critical temperature are plotted in Fig. 5.8. The figure shows that the largest displacement in the axial direction at the critical buckling temperature is around 0.4 mm, and the largest displacement in the axial direction at 575 ℃ (i.e. 100℃ above the critical temperature) is around 1.1 mm. The relatively small deformation is probably due to the large thickness and small radial width. To verify this assumption, the boundary condition of model 2 is changed to FS, and the nonlinear buckling analysis is performed. It is found that at temperature 100℃ above the critical temperature (i.e. 131 ℃), the largest displacement in the axial direction is around 2.8 mm. Therefore, it is confirmed that FS boundary condition is less preferred, as it induces lower critical temperature and larger deformation.

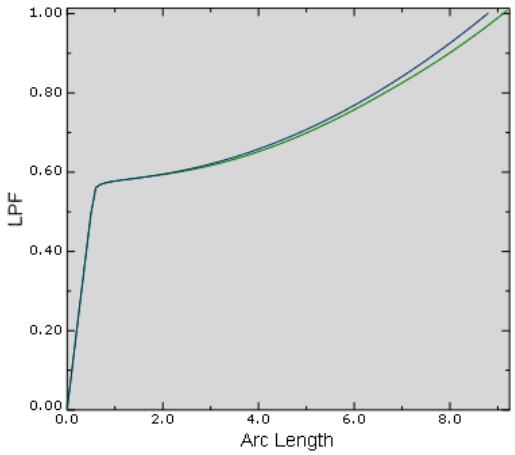

Figure 5.9: The load history diagram of model 1 with plastic properties

The effect of plasticity is also evaluated tentatively. The plasticity is defined in material properties of Mode 1 by a bilinear model in which the yield strength is set as 785GPa and the ultimate strength is set as 980GPa. The thermal load is defined as 721 ℃ which is 300 ℃ above the critical buckling temperature. The load history diagrams of the new model along with that of the original model are plotted in Fig. 5.9. As shown in Fig. 5.9, the plastic properties defined by the simplified bilinear model do not affect the buckling temperature significantly. As the plastic properties of this type of material are still lacking, this research will be conducted in the future.

5.3.3 Effects of Temperature-Dependent Material Properties

In this section, the influences of the temperature-dependent material properties are studied. During engineering applications, the relation between elastic modulus of a certain type of metal and temperature can be estimated by the following equation [70].

$$E(T) = E_0[1 + \alpha_E(t - t_0)] \quad (5\text{-}7)$$

where *E(T)* represents the elastic modulus at a specific temperature, E_0 is elastic modulus at the reference temperature t_0, α_E is the temperature coefficient of elastic modulus.

Normally the temperature coefficient of elastic modulus is negative for most metals. Based on the Table 14-1 of ref. [70] the value of α_E is selected as -0.2589×10^{-3}. Young's moduli in three models are changed to be temperature-dependent, and the other properties remain the same. The load history diagrams are plotted along with that of the original models in Fig. 5.10. It is found that Young's modulus does not affect the critical buckling temperature significantly.

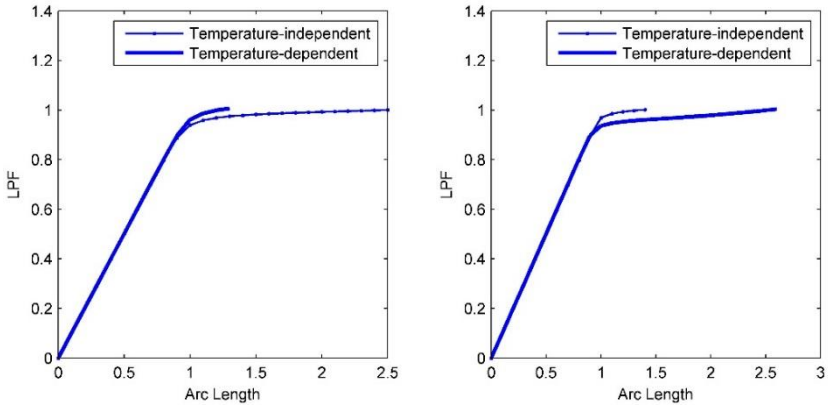

Model 1 Model 2

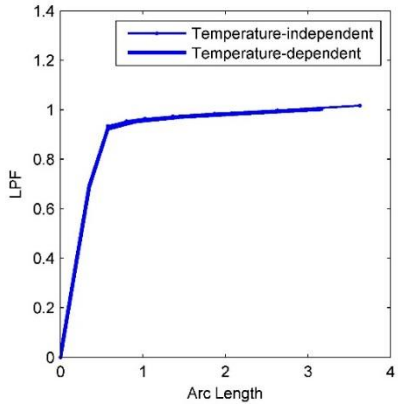

Model 3

Figure 5.10: The load history diagrams of models with temperature-dependent Young's moduli

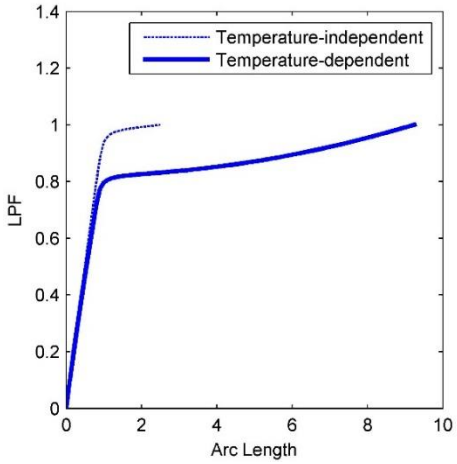

Model 1

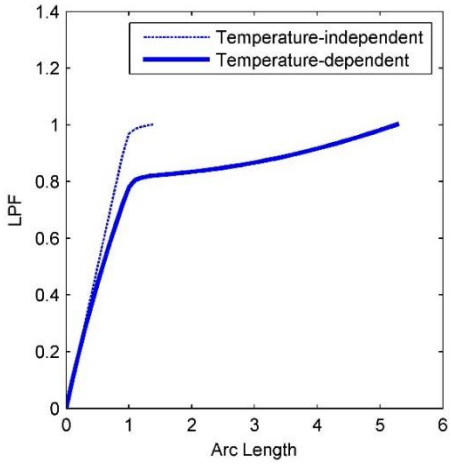

Model 2

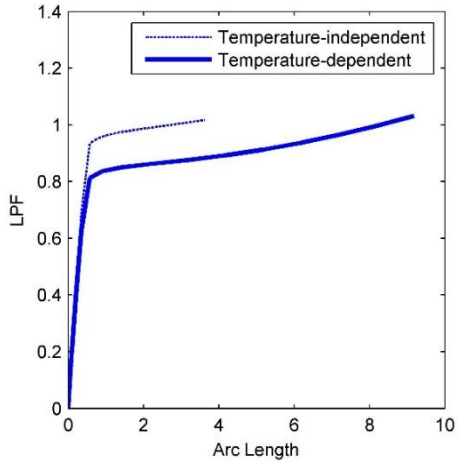

Model 3

Figure 5.11: The load history diagrams of models with temperature-dependent expansion coefficient

The relation between the expansion coefficient of a particular type of metal and temperature can be described by the following equation [71].

$$\alpha(T) = a[1 + b(T + 273.15)] \quad (5\text{-}8)$$

where a and b are two coefficients. The value of a and b are selected as 9.567×10^{-6} and 1.115×10^{-6} based on ref. [71]. Therefore, the relation between the expansion coefficient and temperature can be described by the following equation.

$$\alpha(T) = 9.567 \times 10^{-6}[1 + 1.115 \times 10^{-6}(T + 273.15)] \quad (5\text{-}9)$$

The expansion coefficients in the models are changed to be temperature-dependent, and other properties remain the same. The load history diagrams are plotted along with the load history diagrams of the original models in Figure 5.11. Through Figure 5.11, it was discovered that the critical buckling temperatures represented by the knees of the load history diagram are slightly above 80% of the values obtained from the original model.

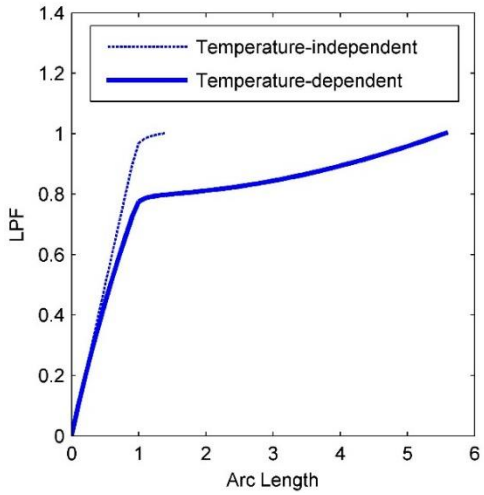

Figure 5.12: The load history diagram of model 2 with temperature-dependent elastic modulus and expansion coefficient

If both Young's module and expansion coefficient are set as temperature-dependent, it is found that the critical buckling temperature is around 80% of the value obtained from the original model as shown in Fig. 5.12. The displacement profile in the

axial direction along the outer radius of model 1 and the displacement profile in the axial direction along the inner radius of model 2 at the critical temperatures obtained from the linear buckling analyses and 100 ℃ above the buckling temperatures are plotted in Fig. 5.13.

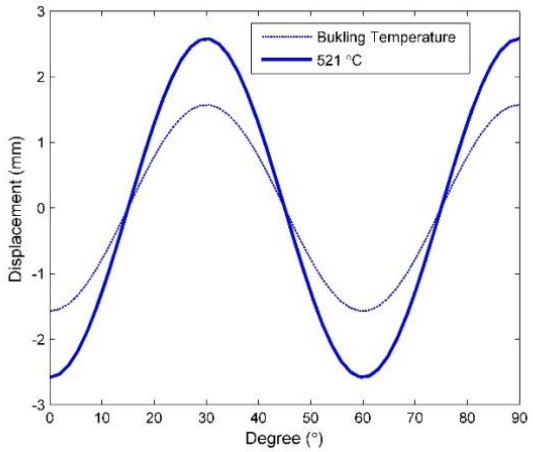

Mode 1

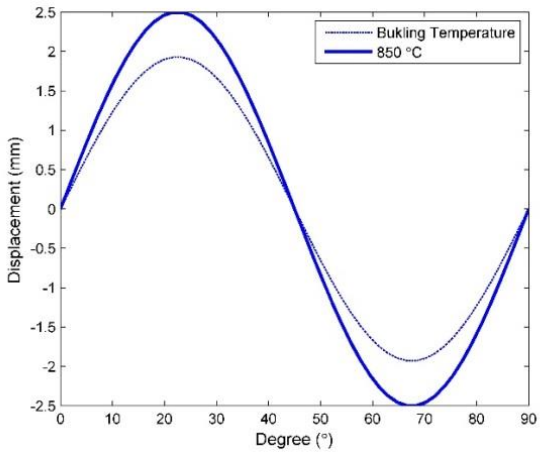

Model 2

Figure 5.13: The displacement profiles in the axial direction at the outer radius of model 1 and the displacement profiles in axial direction at the inner radius of model 2

Through Fig. 5.13, it is confirmed that at the buckling temperature the maximum displacement along the outer radius of model 1 increases from 0.3mm to 1.6mm, and at 100 ℃ above the buckling temperature the maximum displacement along the outer radius of model 1 increases from 1.7mm to 2.6mm. It is also confirmed that at the buckling temperature the maximum displacement along the inner radius of model 2 increases from 0.2mm to 1.9mm and at 100 ℃ above the buckling temperature the maximum displacement along the inner radius of model 2 increases from 2.1mm to 2.5mm.

The displacement profiles in the axial direction along the radius of model 3 with temperature dependent material properties at the buckling temperature and 100 ℃ above the buckling temperature are plotted in Fig. 5.14. It shows that at the buckling temperature the displacement at the inner radius of model 3 increases from 0.4mm to 1.2mm, and at 100 ℃ above the buckling temperature the displacement at the inner radius of model 3 increases from 1.1mm to 1.7mm

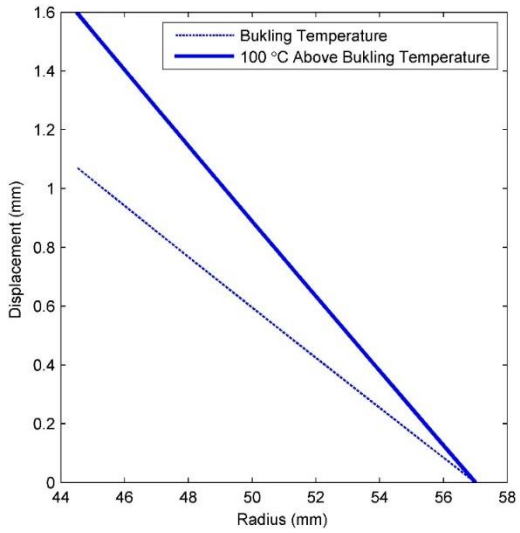

Figure 5.14: The displacement in the axial direction along the radius of model 3

5.4 Conclusion

The finite element models are developed to evaluate the postbuckling of clutch disks or any other ring-shaped mechanical components subjected to elevated temperature. There are two steps in the FEA models. The first step is to develop linear buckling models to obtain critical temperatures and associated deformed shapes. The displacement fields extracted from the deformed shapes are imported to the original geometries to generate the perturbed meshes used in the second step. The second step is to develop the nonlinear buckling models to investigate the postbuckling behaviors. In the current study, the reference loads of linear buckling analyses are linearly distributed temperature fields. The effect of the temperature-dependent material properties is investigated. When elastic modulus is temperature-dependent while the expansion coefficient is temperature-independent, the buckling temperature did not change substantially. However, the critical buckling temperature could decrease significantly when the expansion coefficient is temperature-dependent. Therefore, a linear buckling analysis without considering temperature dependence of material properties is not sufficient. It was also discovered that the maximum displacements during postbuckling could obviously increase when the material properties are temperature dependent. The research findings described in this chapter will be published soon (ref. [72]).

6 CONCLUSIONS

In Chapter 2, the three-dimensional finite element models had been created to study the effects of the different thermal loading profiles upon thermal buckling of clutch disks. It was found that the thermal loads which are uniform along the circumferential direction but vary along the radial direction can cause thermal buckling of clutch disks. It was proved that the different types of temperature profiles along the radial direction affect the deformation shapes of dominant buckling modes and the corresponding critical buckling temperatures evidently. The thermal loads increasing monotonically from the inner radii to the outer radii of disks always lead to axisymmetric dominant buckling modes. But, the axisymmetric buckling modes only exist when the highest temperatures are located at the inner radii of the disks. In other words, the critical buckling eigenvalues are negative. The dominant modes have the lowest simulated critical buckling temperatures. The non-axisymmetric buckling modes also exist when the profile of the thermal load increases monotonically from the inner radius to the outer radius of a clutch disk. However, the critical buckling temperatures are obviously higher. If the highest temperatures of the thermal loads are at the medium radii of the disks, the dominant buckling modes are always non-axisymmetric; and their buckling temperatures are significantly higher than those of the monotonically distributed temperature profiles.

To increase the efficiency and accuracy of the analysis investigating the thermal buckling of a clutch plate, a Fourier finite element method algorithm was developed in

Chapter 3. This approach can calculate the critical thermal buckling temperatures and the associated buckling modes of automotive brakes and clutches with elevated temperatures. In the current research, the thermal load is an axisymmetric predefined temperature distribution which is linearly increasing along the radius. The governing equations were derived based on the Green strain formulation with geometric nonlinearities. Through taking advantage of the Fourier algorithm, the computational cost had been decreased significantly. The reduced Fourier finite element model was validated by comparing the calculated results with that obtained from a three-dimensional finite element analysis by using ABAQUS. Both the wavy modes and coning modes have been obtained from the eigenvectors of the governing equation. It was found that among all buckling modes there is a particular buckling mode with the lowest buckling temperature. The buckling mode with the lowest buckling temperature is determined by the material properties and geometric dimensions. It was discovered that the buckling temperatures of the model with free boundaries are significantly lower than those of a model in which the inner radius is fixed. In the current research the thermal loads are linearly distributed along the radii, meanwhile, this algorithm is also able to be applied to the models with nonlinear temperature profiles. Through this study, it has been found that the TEI dominant modes and thermal buckling dominant modes present similar mode patterns, which implies that these two phenomena can be coupled together.

In Chapter 3, we researched the coupling between the thermoelastic instability (TEI) and the thermal buckling of clutch disks. This part of the current research focuses on evaluating the possibility that the temperature distributions induced by the

thermoelastic instability can lead to the thermal buckling of automotive clutch disks. The reference thermal loads applied in the buckling analyses were obtained from the thermoelastic instability finite element analyses performed by using software *Hotspotter*. It should be mentioned that the temperature distributions obtained through TEI finite element analyses are the eigenvectors of the excited TEI modes. The products of the excited eigenvectors and constant multipliers are also excited eigenvectors or temperature distributions. It was found that the dominant TEI mode is determined by the material properties, the geometric parameters and the sliding speed of a model. In the current research, the dominant modes are banding modes. The critical buckling temperatures and buckling modes have been studied numerically through software ABAQUS. The effects of sliding speed were first studied. The sliding speed had been increased from 10 m/s to 50 m/s. It was found that the critical buckling temperatures increased from around 650 ℃ to 1,100 ℃. The effects of the coefficient of friction were then studied. The coefficient of friction had been increased from 0.13 to 0.65. It was shown that the critical buckling temperatures rose from around 650 ℃ to 1,050 ℃. We found that if the inner circle of the temperature distribution has a higher temperature, the critical buckling temperature is higher than when the outer circle is the high-temperature zone. We also tentatively analyzed the thermal buckling of a model with focal hot spots. It was found that the critical buckling temperatures are extremely high that likely exceed the melting temperature of the material.

In Chapter 5, we developed the finite element models to research the postbuckling behaviors of clutch disks at elevated temperatures. The method of this research consists

of two steps. During the first step, the critical temperatures and associated deformed shapes were obtained through performing *linear* buckling analyses using software ABAQUS. In the current research, the thermal loads are linearly distributed temperature profiles along the radial direction. The scaled displacement fields gained from the deformed shapes of thermal buckling modes were applied to the original geometries to generate the perturbed meshes used in the second step. In the second step, the postbuckling behaviors were evaluated through *RIKS* method by using ABAQUS. The effects of the boundary conditions were studied. It was concluded that installing a clutch disk at outer radius is preferred, as the critical buckling temperature can be raised and the largest deformation value can be reduced. The effects of temperature-dependent material properties were also investigated. It was found that the temperature-dependent Young's modulus does not affect the critical buckling temperatures significantly. However, the critical buckling temperature could be decreased substantially, if the expansion coefficient is temperature-dependent, which implies that linear buckling analyses could be inadequate for thermal buckling problem of clutch disks and automotive disk brakes. The maximum displacements during postbuckling could also increase when the material properties are temperature-dependent.

7 REFERENCES

1. Norton, Robert L. *Machine Design: An Integrated Approach*. Englewood Cliffs, N.J.: Prentice Hall, 1996.

2. Sclater, Neil., and Nicholas P. Chironis. *Mechanisms and Mechanical Devices Sourcebook*. 4th ed. New York: McGraw-Hill, 2007.

3. "How to modify the clutch system of a car." Carnews. Last modified March 7, 2015. Accessed June 14, 2017. http://www.carnews.com/article-39754.html

4. Zagrodzki, P. "Numerical Analysis of Temperature Fields and Thermal Stresses in the Friction Discs of a Multidisc Wet Clutch." *Wear* 101, no. 3 (1985): 255-71.

5. Zagrodzki, P. "Analysis of Thermomechanical Phenomena in Multidisc Clutches and Brakes." *Wear* 140, no. 2 (1990): 291-308.

6. "Disc Brake Conversion Kits." 1937-72 Ford Car Brake Conversion Kits. Accessed July 05, 2017. https://www.performanceonline.com/1937-42-ford-car-disc-brake-conversion-kits/.

7. Bhandari, V. B. *Design of machine elements*. New Delhi: McGraw-Hill Education (India), 2017.

8. Zhao, J., B. Ma, H. Li, M. Chen, and L. Zhu. "Research on Hot Spots of the Multi-disk Clutch and Stability of the System." *Transactions of Beijing Institute of Technology* 34, no.9 (2014): 923-28.

9. Parker, R. C., and P. R. Marshall. "The Measurement of the Temperature of Sliding Surfaces, with Particular Reference to Railway Break Blocks." *Proceedings of the Institution of Mechanical Engineers* 158, no. 1948 (1948): 209-29.

10. Barber, J.R. "The Influence of Thermal Expansion on the Friction and Wear Process." *Wear* 10, no. 2 (1967): 155-59.

11. Barber, J.R. "Thermoelastic Instabilities in the Sliding of Conforming Solids." *Wear* 15, no. 4 (1970): 296.

12. Burton, Nerlikar, and Kilaparti. "Thermoelastic Instability in a Seal-like Configuration." *Wear* 24, no. 2 (1973): 177-88.

13. Fec, and Sehitoglu. "Thermal-mechanical Damage in Railroad Wheels Due to Hot Spotting." *Wear* 102, no. 1 (1985): 31-42.

14. Anderson, and Knapp. "Hot Spotting in Automotive Friction Systems." *Wear* 135, no. 2 (1990): 319-37.

15. Lee, Kwangjin. "Frictionally-excited Thermoelastic Instability in Automotive Disk Brakes." University of Michigan, PhD diss., 1993.

16. Vernersson, T. "Thermally Induced Roughness of Tread-braked Railway Wheels: Part 1: Brake Rig Experiments." *Wear* 236, no. 1-2 (1999): 96-105.

17. Vernersson, T. "Thermally Induced Roughness of Tread Braked Railway Wheels: Part 2: Modelling and Field Measurements." *Wear* 236, no. 1 (1999): 106-16.

18. Du, Shuqin. "Thermoelastic Effects in Automotive Brakes." University of Michigan, PhD diss., 1997.

19. Du, Shuqin, P. Zagrodzki, J. R. Barber, and G. M. Hulbert. "Finite Element Analysis of Frictionally Excited Thermoelastic Instability." *Journal of Thermal Stresses* 20, no. 2 (1997): 185-201.

20. Yi, Yun-Bo, Shuqin Du, J. R. Barber, and J. W. Fash. "Effect of Geometry on Thermoelastic Instability in Disk Brakes and Clutches." *ASME Journal of Tribology* 121, no.4 (1999):661-666.

21. Yi, Yun-Bo. "Thermoelastic Instabilities in Automotive Disk Brakes and Clutches." University of Michigan, PhD diss., 2001.

22. Yi, Yun-Bo, J. R. Barber, and P. Zagrodzki. "Eigenvalue Solution of Thermoelastic Instability Problems Using Fourier Reduction." *Proceedings: Mathematical, Physical and Engineering Sciences* 456, no. 2003 (2000): 2799-821.

23. Hotspotter User's Manual, Version 5.0, University Of Michigan., 2006

24. Jang, and Ahn. "Frictionally-excited Thermoelastic Instability in Functionally Graded Material." *Wear* 262, no. 9 (2007): 1102-112.

25. Zhao, J., Y.-B. Yi, and H. Li. "Effects of Frictional Material Properties on Thermoelastic Instability Deformation Modes." *Proceedings of the Institution of Mechanical Engineers, Part J: Journal of Engineering Tribology* 229, no. 10 (2015): 1239-246.

26. Ma, Chunye. "Thermal Buckling of Automotive Brake Discs." University of Michigan, PhD diss., 2004.

27. Budiansky, Bernard. "Theory of Buckling and Post-Buckling Behavior of Elastic Structures." *Advances in Applied Mechanics* 14, no. C (1974): 1-65.

28. Hutchinson, J. W., and W. T. Koiter. "Postbuckling theory." *Applied Mechanics Reviews* 23, no. 12 (1970): 1353-366.

29. Koiter, and Stanford Univ Ca Dept Of Aeronautics Astronautics. "The Stability of Elastic Equilibrium." 1970.

30. Cenbo, Xiong, Ma Biao, Li Heyan, Zhang Fenglian, and Wu Da. "Experimental Study and Thermal Analysis on the Buckling of Friction Components in Multi-Disc Clutch." *Journal of Thermal Stresses* 38, no. 11 (2015): 1323-343.

31. Timoshenko, Stephen P., and James M. Gere. *Theory of Elastic Stability*. Dover Civil and Mechanical Engineering. Newburyport: Dover Publications, 2012.

32. Audebert, Nadine, J. R. Barber, and P. Zagrodzki. "Buckling of Automatic Transmission Clutch Plates due to Thermoelastic/Plastic Residual Stresses." *Journal of Thermal Stresses* 21, no. 3-4 (1998): 309-26.

33. Zhao, Jiaxin, Zhuo Chen, Huizhou Yang, and Yun-Bo Yi. "Finite Element Analysis of Thermal Buckling in Automotive Clutch Plates." *Journal of Thermal Stresses* 39, no. 1 (2016): 77-89.

34. Ma, and Wang. "Nonlinear Bending and Post-buckling of a Functionally Graded Circular Plate under Mechanical and Thermal Loadings." *International Journal of Solids and Structures* 40, no. 13 (2003): 3311-330.

35. Li, Zhang, and Zhao. "Nonlinear Thermomechanical Post-buckling of Circular FGM Plate with Geometric Imperfection." *Thin-Walled Structures* 45, no. 5 (2007): 528-36.

36. Sepahi, Forouzan, and Malekzadeh. "Thermal Buckling and Postbuckling Analysis of Functionally Graded Annular Plates with Temperature-dependent Material Properties." *Materials and Design* 32, no. 7 (2011): 4030-041.

37. J.R.Barber. J.R.Barber. Accessed June 14, 2017. http://www-personal.umich.edu/~jbarber/.

38. "SIMULIA." 3DS. Accessed June 3, 2017. https://www.3ds.com/products-services/simulia/.

39. "Subsidiaries news." Groupe Dassault. Accessed June 3, 2017. http://www.dassault.fr/en/.

40. El-Adas, Kadmous M. "Linear and Nonlinear Buckling Analysis via Abaqus. " Master Thesis, 1990, Virginia Polytechnic Institute and State University.

41. Deshpande, Shruti. "Buckling and Post Buckling of Structural Components." Master Thesis, University of Texas at Arlington, 2010.

42. Choi, Ji-Hoon, and In Lee. " Transient Thermoelastic Analysis of Disk Brakes in Frictional Contact." *Journal of Thermal Stresses* 26, no. 3 (2003): 223-44.

43. Choi, and Lee. "Finite Element Analysis of Transient Thermoelastic Behaviors in Disk Brakes." *Wear* 257, no. 1 (2004): 47-58.

44. Cho, Chongdu, and Sooick Ahn. "Transient Thermoelastic Analysis of Disk Brake Using The Fast Fourier Transform And Finite Element Method." *Journal of Thermal Stresses* 25, no. 3 (2002): 215-43.

45. Yi, Yun-Bo, and Mohammad Matin. "Eigenvalue Solution of Thermoelastic Damping in Beam Resonators Using a Finite Element Analysis." *Journal of Vibration and Acoustics (Transactions of the ASME)* 129, no. 4 (2007): 478-83.

46. Yi, Y.B. "Geometric Effects on Thermoelastic Damping in MEMS Resonators." *Journal of Sound and Vibration* 309, no. 3 (2008): 588-99.

47. Zhao, Ma, Li, and Yi. "The Effect of Lubrication Film Thickness on Thermoelastic Instability under Fluid Lubricating Condition." *Wear* 303, no. 1-2 (2013): 146-53.

48. Kao, T.K., J.W. Richmond and A. Douarre. "Brake Disc Hot Spotting and Thermal Judder: an Experimental and Finite Element Study." *International Journal of Vehicle Design* 23, no. 3/4 (2000): 276-296.

49. Zagrodzki, P. "Numerical Analysis of Temperature Fields and Thermal Stresses in the Friction Discs of a Multidisc Wet Clutch." *Wear* 101, no. 3 (1985): 255-71.

50. Cook, Robert D. *Concepts and Applications of Finite Element Analysis*. New York: Wiley, 2002.

51. Cook, Robert D. *Finite Element Modeling for Stress Analysis*. New York: Wiley, 1995.

52. Abaqus Software User's Manual 6.9, Providence, RI, 2009.

53. Shi, Yiping. *Case Studies of Finite Element Analyses by Using ABAQUS*. Beijing: China Machine Press, 2006

54. Zhao, Tenglun. *Applications of ABAQUS 6.6 in Mechanical Engineering*. Beijing: China Water&Power Press, 2007

55. Malvern, Lawrence E. *Introduction to the Mechanics of a Continuous Medium*. Prentice-Hall Series in Engineering of the Physical Sciences. Englewood Cliffs, N.J.: Prentice-Hall, 1969.

56. Dvorkin, Eduardo N., and Marcela B. Goldschmit. *Nonlinear Continua*. Computational Fluid and Solid Mechanics. Berlin; New York: Springer-Verlag, 2006.

57. Zienkiewicz, Olek C., Robert L. Taylor, and J.Z. Zhu. *The Finite Element Method Its Basis and Fundamentals*. 6th ed. Burlington: Elsevier Science, 2005.

58. Chen, Zhuo, Yun-Bo Yi, and Jiaxin Zhao. "Fourier Finite Element Model for Prediction of Thermal Buckling in Disc Clutches and Brakes." *Journal of Thermal Stresses* 39, no. 10 (2016): 1241-251.

59. Thornton, EA. "Thermal Buckling of Plates and Shells." *Applied Mechanics Reviews 46*, no. 10 (1993): 486–506.

60. Taunchert, TR. "Thermally Induced Flexure, Buckling and Vibration of Plate." *Applied Mechanics Reviews* 44, no. 8 (1991): 347–60.

61. Najafizadeh, M. M., and B. Hedayati. "Refined Theory for Thermoelastic Stability of Functionally Graded Circular Plates." *Journal of Thermal Stresses* 27, no. 9 (2004): 857-80.

62. Najafizadeh, and Heydari. "Thermal Buckling of Functionally Graded Circular Plates Based on Higher Order Shear Deformation Plate Theory." *European Journal of Mechanics / A Solids* 23, no. 6 (2004): 1085-100.

63. Chen, Zhuo and Yun-Bo Yi. "A Numerical Analysis of the Coupling between Frictionally Excited Thermoelastic Instability and Thermal Buckling." in preparation.

64. "Nonlinear Buckling Analysis Using Workbench 15." CAE Associates. Last modified April 27, 2017. Accessed May 14, 2017. https://caeai.com/sites/default/files/Nonlinear_Buckling_CAEA_0.pdf

65. Ghiasian, Kiani, Sadighi, and Eslami. "Thermal Buckling of Shear Deformable Temperature Dependent Circular/annular FGM Plates." *International Journal of Mechanical Sciences* 81 (2014): 137-48.

66. Wu, Lianyuan. *Shell Theory*. Shanghai: Shanghai Jiao Tong University Press, 1989.

67. Muameleci, Mert. "Linear and Nonlinear Buckling Analyses of Plates using the Finite Element Method." 2014, Master Thesis, Linköping University.

68. Li, Wei. "Buckling and Postbuckling Analysis of Plate with Multiple Cracks." 2014, Master Thesis, **N**anjing **U**niversity of **A**eronautics and **A**stronautics.

69. Kothandaraman, C. P., and Ebrary, Inc. *Fundamentals of Heat and Mass Transfer*. Rev. 3rd ed. New Delhi: New Age International (P), Publishers, 2006.

70. Xu, Feng. and Qingxiang. Li. *The design of Precision Machinery*. Beijing: Tsinghua University Press, 2005.

71. Liu, Tong and Min-Shan Liu. "Theoretical Analysis of the Relationship Between Elastic Constants of Metals and Temperature." *Materials for Mechanical Engineering* 38, no. 3 (2014): 85-95.

72. Chen, Zhuo and Yun-Bo Yi. "Finite Element Models Predicting Postbuckling of Clutch Disks." in preparation.

73. Al-Shabibi, Abdullah M., and James R. Barber. "Transient Solution of the Unperturbed Thermoelastic Contact Problem." *Journal of Thermal Stresses* 32, no. 3 (2009): 226-43.

74. Al-Shabibi, Abdullah M. "Transient Behavior of Initial Perturbation in Multi-disk Clutch System." *Tribology Transactions* 57, (2014): 1164-71.

75. Li, Mingyang. "Influence of Radial Thermal Stress on Buckling Deformation of Separator Discs in Multi-disc Clutches."*Journal of Jilin University*, (2016)

9 APPENDIX A

Published papers:

1. Zhao, Jiaxin, Zhuo Chen, Huizhou Yang, and Yun-Bo Yi. "Finite Element Analysis of Thermal Buckling in Automotive Clutch Plates." *Journal of Thermal Stresses* 39, no. 1 (2016): 77-89.

2. Chen, Zhuo, Yun-Bo Yi, and Jiaxin Zhao. "Fourier Finite Element Model for Prediction of Thermal Buckling in Disc Clutches and Brakes." *Journal of Thermal Stresses* 39, no. 10 (2016): 1241-251.

Papers in preparation:

1. A Numerical Analysis of the Coupling Between Frictionally Excited Thermoelastic Instability and Thermal Buckling

2. Finite Element Models Predicting Postbuckling of Clutch Disks

Conference paper:

1. Yun-Bo Yi and Zhuo Chen, "Modeling of Thermal-Mechanical Instabilities," Advancements in Thermal Management Conference, Denver, Colorado, August 9-10, 2017.

10 APPENDIX B

Future Work

1. Thermal Buckling Analysis of Clutch Disks and Brake Disks Based on Temperature Distributions Obtained by Transient Thermal-Mechanical Analyses

In both the previous and current researches, none of the reference thermal loads applied in buckling finite element analyses are based on the results of transient thermal-mechanical analyses. As pointed out in the second chapter of this dissertation, the reference thermal loads defined in the linear buckling analyses affect both the excited buckling mode and the associated critical buckling temperatures. It is natural for us to explore the possibility of utilizing the temperature distributions obtained via transient thermal-mechanical FEA analyses to investigate thermal buckling of clutch disks and brake disks. Three-dimensional models are computationally inefficient for transient thermal-mechanical FEA analyses of multidisc clutches and disk brakes, as severe nonlinearity in the rotational movements and friction will be involved, and extremely fine meshes will be required to eliminate the numerical difficulty caused by the convective heat transfer. However, it is reasonable to assume that the temperature distributions in multidisc clutches are axisymmetric in general cases. As a result, axisymmetric models in which metal disks and friction disks are represented as two-dimensional layers can be applied to generate temperature distributions. This method has been used extensively to analyze the coupled thermal-mechanical behaviors of clutch and brake systems [73.74]. The simulated temperature distributions are then extracted to perform FEA models evaluating thermal buckling of clutch plates and brake disks.

2. The Fourier FEA Model Evaluating Postbuckling of Annular Plates

During this research, it was found that simulating the postbuckling behaviors of annular plates is computationally inefficient, as a lot of elements were required in the analyses. For instance, there are 5000 elements used in the models discussed in Chapter 5; and the computational time of a single model is around half an hour. Taking advantage of the Fourier finite element algorithm would be beneficial, as only the cross-section of an annular plate is needed to be meshed. As a result, the number of elements used in a single model can significantly be reduced and hence the efficiency and accuracy of the simulation would be improved. We will first determine the critical buckling temperatures and corresponding buckling deformation fields via the methodology described in Chapter 3. The scaled deformation fields will then be added to the original mesh to generate the perturbed meshes used in the postbuckling analyses. The arc length method will be applied to simulate the postbuckling problem defined by equation 5-2. As the Fourier finite element method is applied, the improvement in the efficiency and accuracy of the FEA are expected. Another advantage of the Fourier algorithm is that the dimension in the thickness direction can be taken into account, which would be otherwise unlike for the models mentioned in Chapter 5. Therefore, we can study the effects of temperature variations in the thickness direction. The temperature variations can be noticeable in some situations, especially in the presence of thermoelastic instability or the convective heat transfer.

3. Axisymmetric Postbuckling of Annular Plate with Simply Supported Outer Radius

Based on the result of linear buckling analysis described in the fifth chapter, it is concluded that when the inner radius of an annular plate is free, and the outer radius is simply supported, the dominant buckling model is a coning mode. This conclusion can be verified via ref. [75]. Based on the author's knowledge, the analytical solution of this model is currently unavailable. The governing equation and boundary condition can be expressed by the following equations.

$$\delta u: Ar\frac{d^2u}{dr^2}+\left(A+r\frac{dA}{dr}\right)\frac{du}{dr}+\left(v\frac{dA}{dr}-\frac{A}{r}+A\frac{dv}{dr}\right)u+\frac{1}{2}\left(A+r\frac{dA}{dr}-vA\right)\left(\frac{dw}{dr}\right)^2+$$

$$Ar\frac{dw}{dr}\frac{d^2w}{dr^2}-(1+v)r\left(\alpha A\frac{dT}{dr}+\alpha\frac{dA}{dr}\Delta T+\frac{d\alpha}{dr}A\Delta T\right)-\frac{dv}{dr}\alpha Ar\Delta T=0$$

$$\delta\varphi: Dr\frac{d^2\varphi}{dr^2}+\left(D+r\frac{dD}{dr}\right)\frac{d\varphi}{dr}+\left(v\frac{dD}{dr}-\frac{D}{r}-Cr+D\frac{dv}{dr}\right)\varphi-Cr\frac{dw}{dr}=0$$

$$\delta w: [C-(1+v)\alpha A\Delta T]r\frac{d^2w}{dr^2}+\left[C+r\frac{dC}{dr}-(1+v)\alpha A\Delta T\right]\frac{dw}{dr}+Cr\frac{d\varphi}{dr}$$
$$+\left(C+r\frac{dC}{dr}\right)\varphi+\frac{A}{r}\frac{dw}{dr}u+vA\frac{du}{dr}\frac{dw}{dr}+\frac{1}{2}vA\left(\frac{dw}{dr}\right)^3+Ar\frac{du}{dr}\frac{d^2w}{dr^2}$$
$$+\frac{Ar}{2}\left(\frac{dw}{dr}\right)^2\frac{d^2w}{dr^2}+vAu\frac{d^2w}{dr^2}=0$$

$$\begin{cases}\delta u=0\\ \delta\varphi=0\\ \delta w=0\end{cases}$$

In above equations, $A=\frac{Eh}{1-v^2}$, $D=\frac{Eh}{1-v^2}\frac{h^2}{12}$, $C=\frac{Eh}{1-v^2}\frac{k_s(1-v)}{2}$.

By solving the above equations using the "*differential quadrature"* method, the coning postbuckling phenomenon of the annular disk can be evaluated.

11 APPENDIX C

This is a three-dimensional model input script file for hotspotter.

```
*node
1,0.086,0
2,0.090,0
3,0.095,0
4,0.100,0
5,0.105,0
6,0.110,0
7,0.115,0
8,0.120,0
9,0.125,0

1001,0.086,0.0012
1002,0.090,0.0012
1003,0.095,0.0012
1004,0.100,0.0012
1005,0.105,0.0012
1006,0.110,0.0012
1007,0.115,0.0012
1008,0.120,0.0012
1009,0.125,0.0012

1101,0.086,0.0012
1102,0.090,0.0012
1103,0.095,0.0012
1104,0.100,0.0012
1105,0.105,0.0012
1106,0.110,0.0012
1107,0.115,0.0012
1108,0.120,0.0012
1109,0.125,0.0012

1501,0.086,0.0042
1502,0.090,0.0042
1503,0.095,0.0042
1504,0.100,0.0042
1505,0.105,0.0042
1506,0.110,0.0042
1507,0.115,0.0042
1508,0.120,0.0042
1509,0.125,0.0042
```

```
1601,0.086,0.0042
1602,0.090,0.0042
1603,0.095,0.0042
1604,0.100,0.0042
1605,0.105,0.0042
1606,0.110,0.0042
1607,0.115,0.0042
1608,0.120,0.0042
1609,0.125,0.0042

2601,0.086,0.0054
2602,0.090,0.0054
2603,0.095,0.0054
2604,0.100,0.0054
2605,0.105,0.0054
2606,0.110,0.0054
2607,0.115,0.0054
2608,0.120,0.0054
2609,0.125,0.0054


*nset,nset=bottom,gen
1,9,1
*nset,nset=contact1,gen
1001,1009,1
*nset,nset=contact2,gen
1101,1109,1
*nset,nset=contact3,gen
1501,1509,1
*nset,nset=contact4,gen
1601,1609,1
*nset,nset=top,gen
2601,2609,1

*nfil,nset=p1,bias=2
bottom,contact1,10,100
*nfil,nset=d
contact2,contact3,4,100
*nfil,nset=p2,bias=0.5
contact4,top,10,100

*element,type=cpe4
1,1,2,102,101
1001,1101,1102,1202,1201
1401,1601,1602,1702,1701
```

```
*elgen,elset=pad1,type=cpe4
1,8,1,1,10,100,100
*elgen,elset=disk,type=cpe4
1001,8,1,1,4,100,100
*elgen,elset=pad2,type=cpe4
1401,8,1,1,10,100,100


*revolve,elset=disk
6*60
*revolve,elset=pad1
6*60
*revolve,elset=pad2
6*60


*SOLID SECTION, ELSET=disk, MATERIAL=steel
*MATERIAL, NAME=steel
*ELASTIC
160e9, 0.29
*DENSITY
7800
*SPECIFIC HEAT
487
*CONDUCTIVITY
45.9
*expansion
1.27e-5

*SOLID SECTION, ELSET=pad1, MATERIAL=fric
*SOLID SECTION, ELSET=pad2, MATERIAL=fric
*MATERIAL, NAME=fric
*elastic
2.26e9,0.29
*DENSITY
5500
*SPECIFIC HEAT
460
*CONDUCTIVITY
9.3
*expansion
1.21e-5
```

```
*contact mpc,interaction=inter,orientation=neg
contact2,contact1
contact4,contact3
*surface interaction, name=inter
*friction
0.13
*speed
disk,10
*boundary
top,1,3
bottom,1,3
*STEP
*static
*restart,write
*END STEP
```

12 APPENDIX D

This is a two-dimensional model input script file for hotspotter.

```
*node
1,0.086,0
2,0.090,0
3,0.095,0
4,0.100,0
5,0.105,0
6,0.110,0
7,0.115,0
8,0.120,0
9,0.125,0

1001,0.086,0.0012
1002,0.090,0.0012
1003,0.095,0.0012
1004,0.100,0.0012
1005,0.105,0.0012
1006,0.110,0.0012
1007,0.115,0.0012
1008,0.120,0.0012
1009,0.125,0.0012

1101,0.086,0.0012
1102,0.090,0.0012
1103,0.095,0.0012
1104,0.100,0.0012
1105,0.105,0.0012
1106,0.110,0.0012
1107,0.115,0.0012
1108,0.120,0.0012
1109,0.125,0.0012

1501,0.086,0.0042
1502,0.090,0.0042
1503,0.095,0.0042
1504,0.100,0.0042
1505,0.105,0.0042
1506,0.110,0.0042
1507,0.115,0.0042
1508,0.120,0.0042
1509,0.125,0.0042
```

```
1601,0.086,0.0042
1602,0.090,0.0042
1603,0.095,0.0042
1604,0.100,0.0042
1605,0.105,0.0042
1606,0.110,0.0042
1607,0.115,0.0042
1608,0.120,0.0042
1609,0.125,0.0042

2601,0.086,0.0054
2602,0.090,0.0054
2603,0.095,0.0054
2604,0.100,0.0054
2605,0.105,0.0054
2606,0.110,0.0054
2607,0.115,0.0054
2608,0.120,0.0054
2609,0.125,0.0054

*nset,nset=bottom,gen
1,9,1
*nset,nset=contact1,gen
1001,1009,1
*nset,nset=contact2,gen
1101,1109,1
*nset,nset=contact3,gen
1501,1509,1
*nset,nset=contact4,gen
1601,1609,1
*nset,nset=top,gen
2601,2609,1

*nfil,nset=p1,bias=2
bottom,contact1,10,100
*nfil,nset=d
contact2,contact3,4,100
*nfil,nset=p2,bias=0.5
contact4,top,10,100
```

```
*element,type=2df
1,1,2,102,101
1001,1101,1102,1202,1201
1401,1601,1602,1702,1701

*elgen,type=2df,elset=pad1
1,8,1,1,10,100,100
*elgen,type=2df,elset=disk
1001,8,1,1,4,100,100
*elgen,type=2df,elset=pad2
1401,8,1,1,10,100,100
*elset,elset=pad
pad1,pad2

*SOLID SECTION, ELSET=disk, MATERIAL=steel
*MATERIAL, NAME=steel
*ELASTIC
160e9, 0.29
*DENSITY
7800
*SPECIFIC HEAT
487
*CONDUCTIVITY
45.9
*expansion
1.27e-5

*SOLID SECTION, ELSET=pad, MATERIAL=fric
*MATERIAL, NAME=fric
*elastic
2.26e9,0.29
*DENSITY
5500
*SPECIFIC HEAT
460
*CONDUCTIVITY
9.3
*expansion
1.21e-5

*contact mpc,interaction=int,orientation=neg
contact1,contact2
contact4,contact3
*surface interaction, name=int
*friction
0.13
```

```
*STEP
*hot spot number
0:2:24
*boundary
top,1,3
bottom,1,3
*speed
disk,100
*tei,iter=0.06
*END STEP
```

13 APPENDIX E

This is an example of linear buckling analysis used in ABAQUS. Please note that the contents below keywords “Node”, “Element” and “Temperature” are incomplete. Please also note that keyword “Node file” in this input script file is added manually.

```
*Heading
** Job name: buckle Model name: Model-1
** Generated by: Abaqus/CAE 6.13-1
*Preprint, echo=NO, model=NO, history=NO, contact=NO
**
** PARTS
**
** 200X30
*Part, name=Part-1
*Node
      1,          -86.,           0.,           0.
      2,         -125.,           0.,           0.
       .
       .
       .
   4199,    89.8556366,   2.82382727,           0.
   4200,     87.906601,   2.76257634,           0.
*Element, type=S4R
   1,    1,    5,  439,  240
   2,    5,    6,  440,  439
    .
    .
    .
3999, 4199, 4200,  141,  140
4000, 4200,  339,    4,  141
*Nset, nset=_PickedSet2, internal, generate
    1,  4200,     1
*Elset, elset=_PickedSet2, internal, generate
    1,  4000,     1
** Section: Section-1
*Shell Section, elset=_PickedSet2, material=Copper, controls=EC-1
2.25, 5
*End Part
**
**
** ASSEMBLY
**
*Assembly, name=Assembly
**
*Instance, name=Part-1-1, part=Part-1
```

```
*End Instance
**
*Nset, nset=_PickedSet12, internal, instance=Part-1-1, generate
    1,  4200,     1
*Elset, elset=_PickedSet12, internal, instance=Part-1-1, generate
    1,  4000,     1
*Nset, nset=_PickedSet13, internal, instance=Part-1-1
   1,   4, 142, 143, 144, 145, 146, 147, 148, 149, 150, 151, 152,
153, 154, 155
 156, 157, 158, 159, 160, 161, 162, 163, 164, 165, 166, 167, 168,
169, 170, 171
 172, 173, 174, 175, 176, 177, 178, 179, 180, 181, 182, 183, 184,
185, 186, 187
 188, 189, 190, 191, 192, 193, 194, 195, 196, 197, 198, 199, 200,
201, 202, 203
 204, 205, 206, 207, 208, 209, 210, 211, 212, 213, 214, 215, 216,
217, 218, 219
 220, 221, 222, 223, 224, 225, 226, 227, 228, 229, 230, 231, 232,
233, 234, 235
 236, 237, 238, 239, 240, 241, 242, 243, 244, 245, 246, 247, 248,
249, 250, 251
 252, 253, 254, 255, 256, 257, 258, 259, 260, 261, 262, 263, 264,
265, 266, 267
 268, 269, 270, 271, 272, 273, 274, 275, 276, 277, 278, 279, 280,
281, 282, 283
 284, 285, 286, 287, 288, 289, 290, 291, 292, 293, 294, 295, 296,
297, 298, 299
 300, 301, 302, 303, 304, 305, 306, 307, 308, 309, 310, 311, 312,
313, 314, 315
 316, 317, 318, 319, 320, 321, 322, 323, 324, 325, 326, 327, 328,
329, 330, 331
 332, 333, 334, 335, 336, 337, 338, 339
*Elset, elset=_PickedSet13, internal, instance=Part-1-1
    1,   21,   41,   61,   81,  101,  121,  141,  161,  181,
201,  221,  241,  261,  281,  301
  321,  341,  361,  381,  401,  421,  441,  461,  481,  501,
521,  541,  561,  581,  601,  621
  641,  661,  681,  701,  721,  741,  761,  781,  801,  821,
841,  861,  881,  901,  921,  941
  961,  981, 1001, 1021, 1041, 1061, 1081, 1101, 1121, 1141,
1161, 1181, 1201, 1221, 1241, 1261
 1281, 1301, 1321, 1341, 1361, 1381, 1401, 1421, 1441, 1461,
1481, 1501, 1521, 1541, 1561, 1581
 1601, 1621, 1641, 1661, 1681, 1701, 1721, 1741, 1761, 1781,
1801, 1821, 1841, 1861, 1881, 1901
 1921, 1941, 1961, 1981, 2020, 2040, 2060, 2080, 2100, 2120,
2140, 2160, 2180, 2200, 2220, 2240
 2260, 2280, 2300, 2320, 2340, 2360, 2380, 2400, 2420, 2440,
2460, 2480, 2500, 2520, 2540, 2560
```

```
 2580, 2600, 2620, 2640, 2660, 2680, 2700, 2720, 2740, 2760,
2780, 2800, 2820, 2840, 2860, 2880
 2900, 2920, 2940, 2960, 2980, 3000, 3020, 3040, 3060, 3080,
3100, 3120, 3140, 3160, 3180, 3200
 3220, 3240, 3260, 3280, 3300, 3320, 3340, 3360, 3380, 3400,
3420, 3440, 3460, 3480, 3500, 3520
 3540, 3560, 3580, 3600, 3620, 3640, 3660, 3680, 3700, 3720,
3740, 3760, 3780, 3800, 3820, 3840
 3860, 3880, 3900, 3920, 3940, 3960, 3980, 4000
*Nset, nset="_T-Datum csys-syl", internal
_PickedSet13,
*Transform, nset="_T-Datum csys-syl", type=C
          0.,           0.,           0.,           0.,
0.,           1.
*End Assembly
**
** ELEMENT CONTROLS
**
*Section Controls, name=EC-1, hourglass=ENHANCED
1., 1., 1.
**
** MATERIALS
**
*Material, name=Copper
*Elastic
 1.6e+11, 0.29
*Expansion
 1.27e-05,
**
** BOUNDARY CONDITIONS
**
** Name: BC-1 Type: Displacement/Rotation
*Boundary
_PickedSet13, 1, 1
_PickedSet13, 2, 2
_PickedSet13, 3, 3
_PickedSet13, 4, 4
_PickedSet13, 5, 5
_PickedSet13, 6, 6
** ----------------------------------------------------------------
--
**
** STEP: Step-1
**
*Step, name=Step-1, nlgeom=NO, perturbation
*Buckle
20, , 28, 3000
**
```

```
** BOUNDARY CONDITIONS
**
** Name: BC-1 Type: Displacement/Rotation
*Boundary, op=NEW, load case=1
_PickedSet13, 1, 1
_PickedSet13, 2, 2
_PickedSet13, 3, 3
_PickedSet13, 4, 4
_PickedSet13, 5, 5
_PickedSet13, 6, 6
*Boundary, op=NEW, load case=2
_PickedSet13, 1, 1
_PickedSet13, 2, 2
_PickedSet13, 3, 3
_PickedSet13, 4, 4
_PickedSet13, 5, 5
_PickedSet13, 6, 6
**
** PREDEFINED FIELDS
**
** Name: Predefined Field-1   Type: Temperature Using Field:
AnalyticalField-t
*Temperature
Part-1-1.1, 0.
Part-1-1.2, 1.
.
.
.
Part-1-1.4199, 0.0999999
Part-1-1.4200, 0.05
**
** OUTPUT REQUESTS
**
*Restart, write, frequency=0
**
** FIELD OUTPUT: F-Output-1
**
*Output, field, variable=PRESELECT
*NODE FILE
U
*End Step
```

14 APPENDIX F

This is an example of nonlinear buckling analysis used in ABAQUS. Please note that the contents below keywords “Node”, “Element” and “Temperature” are incomplete. Please also note that keyword “Imperfection” in this input script file is added manually.

```
*Heading
** Job name: Job-post Model name: Model-post
** Generated by: Abaqus/CAE 6.13-1
*Preprint, echo=NO, model=NO, history=NO, contact=NO
**
** PARTS
**
*Part, name=Part-1
*Node
      1,          -86.,           0.,           0.
      2,         -125.,           0.,           0.
       .
       .
       .
   4199,   89.8556366,   2.82382727,           0.
   4200,    87.906601,   2.76257634,           0.
*Element, type=S4R
   1,    1,    5,  439,  240
   2,    5,    6,  440,  439
    .
    .
    .
3999, 4199, 4200,  141,  140
4000, 4200,  339,    4,  141
*Nset, nset=_PickedSet2, internal, generate
    1,  4200,     1
*Elset, elset=_PickedSet2, internal, generate
    1,  4000,     1
** Section: Section-1
*Shell Section, elset=_PickedSet2, material=Copper, controls=EC-1
2.25, 5
*End Part
**
**
** ASSEMBLY
**
*Assembly, name=Assembly
**
*Instance, name=Part-1-1, part=Part-1
*End Instance
```

```
**
*Nset, nset=_PickedSet14, internal, instance=Part-1-1, generate
    1,  4200,     1
*Elset, elset=_PickedSet14, internal, instance=Part-1-1, generate
    1,  4000,     1
*Nset, nset=_PickedSet15, internal, instance=Part-1-1
   1,   4, 142, 143, 144, 145, 146, 147, 148, 149, 150, 151, 152,
153, 154, 155
 156, 157, 158, 159, 160, 161, 162, 163, 164, 165, 166, 167, 168,
169, 170, 171
 172, 173, 174, 175, 176, 177, 178, 179, 180, 181, 182, 183, 184,
185, 186, 187
 188, 189, 190, 191, 192, 193, 194, 195, 196, 197, 198, 199, 200,
201, 202, 203
 204, 205, 206, 207, 208, 209, 210, 211, 212, 213, 214, 215, 216,
217, 218, 219
 220, 221, 222, 223, 224, 225, 226, 227, 228, 229, 230, 231, 232,
233, 234, 235
 236, 237, 238, 239, 240, 241, 242, 243, 244, 245, 246, 247, 248,
249, 250, 251
 252, 253, 254, 255, 256, 257, 258, 259, 260, 261, 262, 263, 264,
265, 266, 267
 268, 269, 270, 271, 272, 273, 274, 275, 276, 277, 278, 279, 280,
281, 282, 283
 284, 285, 286, 287, 288, 289, 290, 291, 292, 293, 294, 295, 296,
297, 298, 299
 300, 301, 302, 303, 304, 305, 306, 307, 308, 309, 310, 311, 312,
313, 314, 315
 316, 317, 318, 319, 320, 321, 322, 323, 324, 325, 326, 327, 328,
329, 330, 331
 332, 333, 334, 335, 336, 337, 338, 339
*Elset, elset=_PickedSet15, internal, instance=Part-1-1
    1,   21,   41,   61,   81,  101,  121,  141,  161,  181,
201,  221,  241,  261,  281,  301
  321,  341,  361,  381,  401,  421,  441,  461,  481,  501,
521,  541,  561,  581,  601,  621
  641,  661,  681,  701,  721,  741,  761,  781,  801,  821,
841,  861,  881,  901,  921,  941
  961,  981, 1001, 1021, 1041, 1061, 1081, 1101, 1121, 1141,
1161, 1181, 1201, 1221, 1241, 1261
 1281, 1301, 1321, 1341, 1361, 1381, 1401, 1421, 1441, 1461,
1481, 1501, 1521, 1541, 1561, 1581
 1601, 1621, 1641, 1661, 1681, 1701, 1721, 1741, 1761, 1781,
1801, 1821, 1841, 1861, 1881, 1901
 1921, 1941, 1961, 1981, 2020, 2040, 2060, 2080, 2100, 2120,
2140, 2160, 2180, 2200, 2220, 2240
 2260, 2280, 2300, 2320, 2340, 2360, 2380, 2400, 2420, 2440,
2460, 2480, 2500, 2520, 2540, 2560
```

```
 2580, 2600, 2620, 2640, 2660, 2680, 2700, 2720, 2740, 2760,
2780, 2800, 2820, 2840, 2860, 2880
 2900, 2920, 2940, 2960, 2980, 3000, 3020, 3040, 3060, 3080,
3100, 3120, 3140, 3160, 3180, 3200
 3220, 3240, 3260, 3280, 3300, 3320, 3340, 3360, 3380, 3400,
3420, 3440, 3460, 3480, 3500, 3520
 3540, 3560, 3580, 3600, 3620, 3640, 3660, 3680, 3700, 3720,
3740, 3760, 3780, 3800, 3820, 3840
 3860, 3880, 3900, 3920, 3940, 3960, 3980, 4000
*Nset, nset="_T-Datum csys-syl", internal
_PickedSet15,
*Transform, nset="_T-Datum csys-syl", type=C
          0.,           0.,           0.,           0.,
0.,           1.
*End Assembly
**
** ELEMENT CONTROLS
**
*Section Controls, name=EC-1, hourglass=ENHANCED
1., 1., 1.
**
** MATERIALS
**
*Material, name=Copper
*Elastic
    1.6e+11, 0.29,   0.
 1.1858e+11, 0.29,1000.
*Expansion
 1.2481e-05,   0.
 2.1546e-05,1000.
**
** BOUNDARY CONDITIONS
**
** Name: BC-1 Type: Displacement/Rotation
*Boundary
_PickedSet15, 1, 1
_PickedSet15, 2, 2
_PickedSet15, 3, 3
_PickedSet15, 4, 4
_PickedSet15, 5, 5
_PickedSet15, 6, 6
** ----------------------------------------------------------------
--
**
** STEP: Step-1
**
*IMPERFECTION,FILE=buckle,STEP=1
1,2.25e-3
*Step, name=Step-1, nlgeom=YES, inc=10000
```

```
*Static, direct, riks
0.1, 1., , , 1.,
**
** PREDEFINED FIELDS
**
** Name: Predefined Field-1   Type: Temperature Using Field:
AnalyticalField-t
*Temperature
Part-1-1.1, 0.
Part-1-1.2, 421.
.
.
.
Part-1-1.4199, 42.1
Part-1-1.4200, 21.05
**
** OUTPUT REQUESTS
**
*Restart, write, frequency=0
**
** FIELD OUTPUT: F-Output-1
**
*Output, field, variable=PRESELECT
**
** HISTORY OUTPUT: H-Output-1
**
*Output, history, variable=PRESELECT
*End Step
```